Mahmoud Rajabbi

Climate and Environmental Monitoring using GNSS Remote Sensing

Doctoral thesis

NTNU
Norwegian University of
Science and Technology

Mahmoud Rajabbi

Climate and Environmental Monitoring using GNSS Remote Sensing

Thesis for the Degree of Philosophiae Doctor

Trondheim, June 2024

Norwegian University of Science and Technology
Faculty of Engineering
Department of Civil and Environmental Engineering

NTNU
Norwegian University of
Science and Technology

To my parents and wife
the heavenly sources of
hope and unconditional love...

This page is intentionally left blank

Preface

This thesis is submitted in partial fulfillment of the *Philosophiae Doctor* (PhD) degree requirements at the Norwegian University of Science and Technology (NTNU). The research has been conducted for four years, from March 2019 to March 2023, from which three years were designated for the Ph.D. research and one year to non-curricular activities. The doctoral studies were performed predominantly in the Geomatics group of the Department of Civil and Environmental Engineering (IBM). A duration of about two months was spent at the Department of Geodesy at the German Research Center for Geosciences (GFZ) in Potsdam, Germany. Most of the ground-based experimental data used in this thesis has been provided by GFZ.

This page is intentionally left blank

Abstract

The potential of Global Navigation Satellite System (GNSS) signals for remote sensing applications has been widely recognized. The widespread availability of GNSS signals, whether in direct form or as reflections, enables the extraction of various Earth system component parameters. This thesis comprises of multiple investigations concerning the evaluation and improvement of data products derived from GNSS remote sensing, as well as the exploration of other potential applications.

Exemplary datasets from two classes of GNSS data products are used. The thesis presents studies based on reflected signals of Medium Earth Orbiting (MEO) GNSS satellites in bistatic radar configuration. The reflected signals can be received by ground-based receivers or spaceborne receivers onboard Low Earth Orbiting (LEOs) satellites. In this sense, the thesis focuses on a new generation of observations from the spaceborne GNSS-R technique for flood detection purposes. Finally, ground-based GNSS-Reflectometry (GNSS-R) measurements with demonstrated applications for environmental monitoring.

The initial research in this thesis centers on a dataset derived from advanced spaceborne GNSS-R observations, specifically addressing flood detection and mapping during intense rainfall events. Flood detection and produced maps play essential roles in policymaking, planning, and implementing flood management options. The investigation is carried out in a region prone to flooding, necessitating continuous monitoring with timely observations. A threshold of about 11 dB or more could be distinguished between the inundated and noninundated areas in the regions of interest. The flood-affected areas were mapped on Google Maps. The area of the flooded regions was estimated to be about 19,644 km2 or 10.8% of the study area. The findings underscore the capability of spaceborne GNSS-R to deliver observations characterized by the necessary sensitivity and frequent revisits, enabling the identification and mapping of inundated regions.

A GNSS-R dataset from a coastal experiment has been used in three studies of this thesis to investigate possible quality improvements of sea surface characterization measurements. The dataset includes polarimetric observations recorded using a dedicated reflectometry receiver with multiple input antennas. The antennas have Right- and Left-Handed Circular Polarizations (RHCP and LHCP) and are installed at zenith and sea-looking orientations. The studies show that polarimetric observations can significantly improve the quality of the GNSS-R measurements. The dataset is used to assess GNSS-R sea-level monitoring under different

scenarios. The effects of sea surface roughness, wind effect, polarization and orientation of the antenna, and the frequency of the GNSS signal are studied. The results show that the roughness and wind can degrade the accuracy of the GNSS-R sea-level measurements. The best GNSS-R altimetric performance is observed when combined multi-frequency measurements are used from a sea-looking antenna with an LHCP design. The RMSEs between GNSS-R sea surface heights for LHCP sea-looking antenna with respect to collocated tide gauge (TG) measurements are 2.4, 3.0, 4.5, and 5.6 cm for 6-, 3-, 1-, and 0.25-h window sizes, respectively. The seaward orientation can improve the accuracy of RHCP sea level results up to 20%, 13%, and 25%, respectively, for L1, L2, and L12. This improvement can reach about 48%, 50%, and 47% for L1, L2, and L12 if the tilted antenna is LHCP.

The data set with this type but longer is also applied for tidal analysis. The detection results highlight a good match between GNSS-R and TG. we estimate the amplitude and phase of standard tidal harmonics from the two datasets. The results show an overall good agreement between the datasets with a few exceptions. There are some differences between the estimated amplitude (K_1) and phase ($K_1, OO_1, K_2, and MK_3$) values. The GPS orbital period can be one of the main contributors to the observed differences as reported by previous studies. This effect is more noticeable in the phase of the tidal harmonics. Higher harmonics, i.e., the periods shorter than 3 hours show stronger signatures in GNSS-R data.

Acknowledgments

This page is intentionally left blank

Table of Contents

This page is intentionally left blank

List of Tables

This page is intentionally left blank

List of Figures

This page is intentionally left blank

List of Abbreviations

ADC	Analog to Digital Converter
AGC	Automatic Gain Controller
BRCS	Bistatic Radar Cross Section
CME	Change Magnitude Estimator
CORS	Continuously Operating Reference Station
CS	Commercial Service
CYGNSS	Cyclone GNSS mission
DDM	Delay-Doppler Map
ECMWF	European Center for Medium-range Weather Forecast
EIRP	Equivalent Isotropically Radiated Power
GCOS	Global Climate Observing System
GEO	Geostationary orbit
GLONASS	GLObal NAvigation Satellite System
GNSS	Global Navigation Satellite Systems
GNSS-R	GNSS-Reflectometry
GNSS-RO	GNSS Radio Occultation
GORS	GNSS Occultation, Reflectometry, and Scatterometry receiver
GPS	Global Positioning System
GPT	Global Pressure and Temperature model
GRUAN	GCOS Reference Upper-Air Network
I/Q	In-phase/Quadrature
IF	Intermediate Frequency
IGS	International GNSS Service
IGSO	Inclined Geosynchronous Orbit
IRNSS	Indian Regional Navigation Satellite System

LEO	Low Earth Orbit
LHCP	Left-Handed Circular Polarization
LNA	Low-Noise Amplifier
LS-HE	Least-Squares Harmonics Estimation
MEO	Medium-altitude Earth Orbit
MSS	Mean Square Slopes
NBRCS	Normalized Bistatic Radar Cross Section
NWP	Numerical Weather Prediction model
OS	Open Service
PCO	Phase Center Offset
PCV	Phase Center Variation
PPS	Precise Positioning Service
PRN	PseudoRandom Noise
PRS	Public Regulated Service
PWV	Precipitable Water Vapor
QZSS	Quasi-Zenith Satellite System
RHCP	Right-Handed Circular Polarization
RMSE	Root Mean Squared Error
SAR	Synthetic Aperture Radar
SNR	Signal-to-Noise Ratio
SoOP	Signals of Opportunity
SP	Specular Point
SPS	Standard Positioning Service
SR	Surface Reflectivity
SSA	Singular Spectrum Analysis
SST	Sea Surface Temperature
SVD	Singular Value Decomposition
SWH	Significant Wave Height
VMF	Vienna Mapping Function
ZTD	Zenith Total Delay

Chapter 1

Introduction

1.1 Motivation

Climate and environmental monitoring involve the collection, analysis, and interpretation of data on various aspects of the environment. This can include factors such as air quality, water quality, weather patterns, and ecosystem health, among others.

There are several reasons why climate and environmental monitoring is important. First, it provides policymakers and decision-makers with the information they need to develop effective policies and strategies to address environmental challenges. For example, data on air and water quality can help inform regulations and standards to protect human health and the environment. Information on weather patterns and climate change can help inform adaptation strategies to reduce the impacts of extreme weather events.

Second, environmental monitoring can help identify trends and changes in the environment over time. This is important for understanding how human activities and natural processes are affecting the environment and for tracking progress towards environmental goals. For example, monitoring the health of ecosystems can help identify areas where conservation efforts are needed to protect biodiversity.

Finally, environmental monitoring can help raise awareness among the public about environmental issues and encourage individuals and communities to take action to protect the environment. By providing accessible and understandable information on the state of the environment, monitoring can help build support for environmental protection efforts and motivate people to make changes in their daily lives to reduce their environmental impact.

Overall, climate and environmental monitoring is an essential tool for understanding the state of the environment, developing effective policies and strategies, and empowering individuals and communities to take action to protect the planet.

Remote sensing is the use of satellites, aircraft, or other platforms to collect data on the Earth's surface and atmosphere from a distance. This technology has revolutionized the field of climate and environmental monitoring, providing a wealth of data on a wide range of environmental parameters. This method has enabled scientists to gain a better understanding of the state of the environment and the impacts of human activities and has provided valuable information for policy-makers and decision-makers working to protect the planet. Several remote sensing methods are commonly used for climate and environmental monitoring: 1-Optical Remote Sensing: This method involves the use of sensors that capture electromagnetic radiation in the visible, near-infrared, and shortwave-infrared parts of the spectrum. Optical remote sensing can be used to collect data on land cover, vegetation health, and water quality, among other parameters. 2-Radar Remote Sensing: Radar sensors emit electromagnetic pulses and measure the time it takes for the pulses to bounce back from the Earth's surface. This method can be used to collect data on land topography, soil moisture, and ice cover. 3-LiDAR Remote Sensing: LiDAR sensors use laser beams to measure the distance between the sensor and the Earth's surface. This method can be used to collect data on topography, vegetation height, and forest structure. 4-Passive Microwave Remote Sensing: This method involves the use of sensors that detect the natural microwave radiation emitted by the Earth's surface. Passive microwave remote sensing can be used to collect data on soil moisture, sea surface temperature, and atmospheric water vapor. 5-Thermal Infrared Remote Sensing: Thermal infrared sensors measure the temperature of the Earth's surface by detecting the infrared radiation emitted by objects. This method can be used to collect data on land surface temperature and the thermal properties of vegetation.

Each remote sensing method has its strengths and weaknesses, and the choice of method depends on the specific environmental parameter being measured and the spatial and temporal resolution required. By combining data from multiple remote sensing methods, scientists can gain a more comprehensive understanding of the state of the environment and how it is changing over time.

The Global Navigation Satellite System (GNSS) offers a range of primary services, including positioning, navigation, and timing. However, in recent years, the system has been utilized for a variety of other applications, including GNSS RS. This technique involves using measurements from GNSS signals to gather valuable information about different components of the Earth's system. By observing the GNSS signals passing through the atmosphere, researchers have been able to

study the atmospheric layers and their variabilities. Additionally, GNSS signals that reflect off the Earth's surface can provide insight into various parameters of the Earth's surface and water cycles. For example, scientists have used these reflections to study snow depth, ice height and sea level, soil moisture, vegetation, floods, ocean eddies, wind speed, salinity, and more.

Natural disasters often cause significant disturbances to communities and the environment, resulting in human, environmental, social, and economic losses that communities are unable to bear. Among these disasters, floods are particularly devastating, causing extensive damage to both the artificial and natural environment and leading to the destruction of human settlements. In recent years, the economic losses due to flood damage have increased considerably around the world. Floods occur when water bodies, including riversides, lakes, dams, or dikes, overflow onto low-lying lands during heavy rainfall. The rising temperatures on Earth's surface are leading to increased evaporation and higher overall precipitation levels. Although increased precipitation is typically associated with inland flooding, it can also raise the risk of coastal flooding.

Land surveying and airborne observations are conventional methods used for flood detection. However, these techniques can be expensive and time-consuming when applied on a large scale. Alternatively, Space-based Remote Sensing (RS) offers a practical alternative that provides up-to-date information from various sensors aboard different satellites. Despite this, there are limitations to using RS data for flood detection. For example, optical RS has restrictions during severe weather conditions and at night, which can limit its ability to provide the necessary information before and after a flood event [7]. However, Radar RS in the microwave spectrum can overcome these limitations by penetrating through clouds and vegetation and can work effectively at night. Among the several radar RS sensors in operation, Synthetic Aperture Radar (SAR) imagery provides high spatial resolution data but typically uses a monostatic configuration, resulting in long revisit times (more than one week) and limited temporal resolution for flood detection purposes. Due to the highly dynamic nature of floods, SAR images are not typically used operationally during floods.

The measurement of sea surface level is a crucial parameter in various scientific fields, including geology, geodesy, oceanography, and archaeology, as it helps in understanding climate and environmental changes. The impact of global warming and natural disasters such as floods, tsunamis, and volcanoes on sea surface level can have both major and minor effects on modern civilization. The significance of sea surface level information is further underscored by the large population, economic activities, and commercial developments in coastal areas. Furthermore, the sea surface level is critical for determining the vertical datum (geoid) and measur-
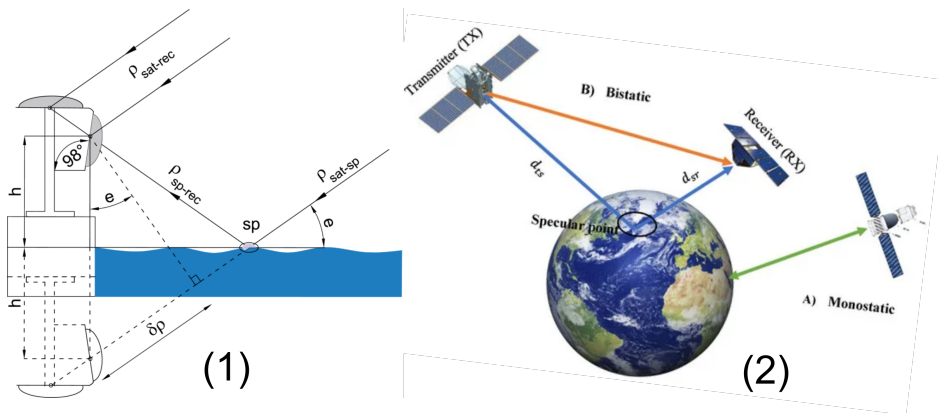
Figure 1.1: A schematic view of different methods of GNSS remote sensing data products (1. ground-based and 2. space-borne) for the monitoring of climate and environment.

ing the Earth's shape. Therefore, accurate and reliable methods for monitoring sea surface levels are crucial.

Sea level monitoring is essential for understanding the Earth's system and predicting the impact of climate change. Traditional tide gauges and spaceborne radar altimeters are two commonly used methods for sea level monitoring. However, these methods have limitations. Tide gauges provide pointwise measurements and are affected by subsidence, tectonics, and human activities, leading to potential inaccuracies in the data. On the other hand, radar altimeters suffer from degradation in accuracy close to the coast due to land effects and geophysical corrections. Furthermore, the spatiotemporal resolution of this method is limited, which restricts its effectiveness in coastal areas. Therefore, there is a need for more accurate and reliable sea level monitoring methods that can overcome these limitations and provide accurate data for scientific and practical applications.

With all GNSS satellites (GPS, Galileo, GLONASS, and Beidou) becoming operational, multi-signals are now available that are capable of remotely sensing the Earth's atmosphere and surface providing highly precise, continuous, all-weather and near real-time environmental monitoring data.

This thesis aims to use GNSS-R in both space-born and ground-based capabilities to minimize remote sensing limitations for sea level monitoring and flood detection as a climate and environment indicator. The contribution of GNSS-R data is at different levels from raw to final scientific data products that have been processed.

1.2   Problem Statement

The use of GNSS-R technology, which involves measuring the reflections of GNSS signals from surfaces such as land and water, presents numerous opportunities for environmental monitoring and natural hazard warning systems. In inland areas, this technology can be used for soil moisture and flood detection based on small satellite observations. Meanwhile, coastal regions are of particular interest due to the proximity of permanent GNSS stations to water bodies. These stations can receive GNSS signals that bounce off the sea surface and reflect back to the receiver. By analyzing the characteristics of these reflections, such as the time delay and amplitude, important information about the state of the sea surface, including sea level, wave height, and surface roughness, can be inferred.

Regarding the use of space-born for flood detection: the traditional methods, such as land surveying and airborne observations, can be expensive and time-consuming when applied on a large scale. While space-based remote sensing offers a practical alternative, optical remote sensing has limitations during severe weather and at night, and Synthetic Aperture Radar (SAR) has limited temporal resolution and is not typically used operationally during floods due to its highly dynamic nature. Thus, there is a need for cost-effective and reliable flood detection methods that can operate in all weather conditions, and with high temporal and spatial resolution. One potential solution is the use of Space Born GNSS-R technology, which involves measuring the reflections of GNSS signals However, the utilization of small satellites with GNSS receivers needs to fully exploit the potential of this technology and address the limitations of traditional flood detection methods.

One of the challenges in using standard geodetic receivers for reflectometry observations is that they are not optimized for this purpose. These receivers are typically designed for precise positioning and navigation, rather than reflectometry measurements. Therefore, dedicated reflectometry receivers are needed to fully exploit the potential of GNSS-R observations. These specialized receivers are designed to capture and process the reflected signals with higher sensitivity and accuracy, allowing for more precise measurements of the sea surface characteristics.

The utilization of dedicated reflectometry receivers can also help in assessing the performance of GNSS-R sensors in different scenarios. By comparing the observations from different reflectometry receivers and analyzing the discrepancies, researchers can gain insights into the accuracy, reliability, and limitations of GNSS-R measurements in various environmental conditions, such as calm seas, rough seas, or during severe weather events. This information is crucial for developing and improving GNSS-R-based applications, such as weather prediction, oceanography, and climate monitoring.

Furthermore, the findings from reflectometry observations using dedicated receivers can also inform the design and implementation of spaceborne missions. Low-cost, low-power, and low-mass GNSS-R sensors can be deployed on small satellites, forming constellations that provide global coverage and high temporal sampling of environ-mental parameters. These small-satellite constellations can utilize GNSS-R signals or other L-band signals of opportunity (SoOP) to monitor and predict abrupt weather haz-ards, such as hurricanes, storms, and floods, in near real-time. This can greatly enhance our ability to monitor and understand weather patterns and natural hazards, and im-prove early warning systems for disaster mitigation.

The use of L-band microwave signals in GNSS-R is particularly advantageous compared to optical sensors or other frequency bands such as Ku-band or C-band. L-band signals are less affected by cloud coverage and can penetrate through rain and severe weather conditions more effectively, making them suitable for all-weather and day-and-night observations. Moreover, the relatively low cost and low mass of small satellites carrying GNSS-R sensors make them a cost-effective solution for collecting frequent and con-tinuous data over large areas, enabling high temporal and spatial resolution monitoring of environmental parameters.

1.3 Research Objectives and Research Questions

The availability of GNSS satellites and permanent stations worldwide, along with advancements in GNSS signal transmitters and receiving equipment, and the potential for low-cost high-performance GNSS-based Earth-observing small satellites, have led to increased research opportunities and data exploitation challenges. This thesis aims to address some of these demands and issues, with a specific focus on GNSS-R as a relatively new remote sensing technique. The thesis will primarily focus on assessing and improving the quality of GNSS-R observations based on recent space-borne and ground-based observations. The main objectives of this thesis can be summarized as follows:

Objective 1: The novel application of the new-generation space-borne GNSS remote sensing measurements.

GNSS satellites are designed to offer continuous navigation services on and near the Earth's surface, including low Earth orbit (LEO) satellites. These satellites provide global coverage and present an opportunity to establish a passive Earth-observing system that operates in all weather conditions and at any time of day. Unlike traditional remote sensing satellites that are bulky and expensive, GNSS-R (GNSS-Reflectometry) sensors can be utilized with small satellites due to their less demanding instrumentation requirements. In a passive configuration, a GNSS-R sensor collects and processes both direct and reflected GNSS signals from the

Earth's surface. This approach enables the derivation of various geophysical parameters, which find application in scientific fields such as climate and environmental monitoring. Implementing spaceborne GNSS-R on a constellation of cost-effective CubeSats allows for high spatiotemporal resolution data, global coverage, and frequent revisits. This new generation of observations facilitates the study of interactions between the atmosphere and the ocean or land. However, further research is needed to demonstrate the feasibility of these innovative applications and garner attention from the scientific community. To address these goals, the following research questions are examined in this thesis:

- *RQ 1.1: How can the new generation of GNSS measurements from spaceborne reflectometry be used for climate and environmental monitoring?*

- *RQ 1.2: Can the observations from the CYGNSS mission be used for flood detection and mapping during extreme rainfall events in Sistan and Baluchestan?*

- *RQ 1.3: How we can use CYGNSS data for flood detection?*

- *RQ 1.4: What are the advantages and limitations of using CYGNSS data for flood monitoring and management in the study area?*

Objective 2: To contribute to improving the emerging category of remote sensing data products derived from GNSS technology, efforts are being made to enhance its capabilities.

The global network of permanent GNSS stations offers significant potential for generating remote sensing data products through the analysis of reflected signals. For instance, GNSS stations located in coastal areas, which have a clear view of the sea, can receive GNSS signals reflected from the ocean surface. These stations enable the retrieval of various information pertaining to the sea surface, including its roughness and variations in sea level. The stations typically employ a standardized setup consisting of a geodetic receiver and a zenith-looking antenna with Right-Handed Circular Polarization (RHCP). However, the performance of reflectometry observations can vary depending on the polarization and orientation of the antenna. Investigating these different scenarios provides valuable insights for improving measurements and exploring new applications, particularly in spaceborne configurations. To this end, the focus of the thesis is on characterizing the sea surface and addressing specific research questions in this area.

- *RQ 2.1: How can we enhance the performance of the ground-based GNSS-R measurements for sea surface height and tidal analysis?*

- *RQ 2.2: What could be the prospect for future ground-based GNSS-R stations?*

- *RQ 2.3: Can Mathematical methods like LSHE and SAS, improve the data products generated from GNSS-R?*

1.4   Research Approach

This section presents a summary of the datasets, processing methodologies, and data analysis techniques employed in this thesis.

To address the research questions RQ 1.1, RQ 1.2, RQ 1.3, and RQ 1.4, a dataset consisting of spaceborne GNSS-R observations collected by a constellation of micro-satellites launched by NASA is employed. These observations offer a valuable resource for studying and exploring the potential applications of the latest GNSS-based technology. The primary focus of this research is to leverage these new-generation GNSS-based observations for potential applications over land areas. By analyzing and interpreting the dataset, the thesis aims to uncover novel insights, patterns, and information that can contribute to various fields. The utilization of these new-generation GNSS-based observations holds promise for advancing our understanding and practical applications in land-based remote sensing. In order to justify and verify the findings, the GNSS-R dataset utilized in this thesis is collocated with a match-up dataset consisting of optical satellite images. By combining these datasets, the research aims to establish a robust and comprehensive understanding of the observed phenomena. The collocation process involves aligning and synchronizing the GNSS-R observations with corresponding optical satellite images, allowing for a comparative analysis. This approach enables researchers to validate the accuracy and reliability of the GNSS-R measurements by cross-referencing them with independent optical data. By leveraging the complementary information provided by both datasets, the research can gain further insights and strengthen confidence in the results. The integration of the GNSS-R and optical satellite datasets enhances the scientific rigor and expands the scope of the analysis, facilitating a more comprehensive evaluation of the land-based applications of the new-generation GNSS remote sensing technology.

Regarding RQ 2.1, RQ 2.2 and RQ 2.3 a six-year dataset obtained from a coastal GNSS-R experiment conducted at Onsala Space Observatory in Sweden is utilized. The dataset comprises raw observations collected by a dedicated GNSS-R receiver, which simultaneously captures reflected signals from three antennas with varying polarizations and orientations. Given the thesis's focus on characterizing the sea surface, the performance of GNSS-R observations in retrieving sea surface sea level and tidal harmonics is evaluated. This assessment considers differ-

ent variables such as antenna polarization, antenna orientation, and the influence of wind. The results of this performance assessment not only address research questions but also provide insights into future experiments and encourage further research endeavors. Additionally, drawing from the findings of both ground-based and spaceborne GNSS-R measurements, the thesis presents a potential design for future spaceborne GNSS-R sensors that are compatible with CubeSat specifications. This design proposal contributes to the advancement of spaceborne GNSS-R technology and its potential applications in CubeSat missions.

1.5   Structure of the Dissertation

This dissertation comprises five chapters. The introduction in the current chapter provided an overview of the topic and described the motivation, research questions, and research objectives. A short description of the research approach is also included in Chapter 1. In the second chapter, a brief explanation of the theoretical background is provided. Chapter 3 presents an overview of the results and a summary of the papers included in this dissertation. Chapter 4 provides the concluding remarks together with an outlook for future research topics. A list of the references is provided after Chapter 4. The last chapter comprises the publications associated with this thesis.

This page is intentionally left blank

Chapter 2

Theoretical Foundations

2.1 Global Navigation Satellite Systems (GNSS)

Global Navigation Satellite Systems (GNSS) are a collection of satellite-based systems that provide positioning, navigation, and timing services to users on or near the Earth's surface. The fundamental principle behind satellite-based positioning is similar to the traditional resection process that has been historically used. In the resection process, the position of an unknown object is determined by measuring its distances to several objects with known positions. Similarly, GNSS relies on observing distant objects with known positions, which in this case are the satellites themselves. By measuring the distances or range to multiple satellites, a receiver on the Earth's surface can calculate its own position. For a detailed explanation of GNSS, including how they work, their key components, and an overview of their applications, readers are advised to refer to e.g., [30, 23, 58]. Figure 2.1 shows the GNSS positioning basic, based on the traditional resection concept. From the practical point of view, however, a fourth satellite is needed to account for the receiver clock offset.

The distance measurement in the satellite-based positioning is carried out through electromagnetic waves or GNSS signals. The frequencies of the signals are in the part of the L-band spectrum, which resides between about 1.2 and 1.6 GHz, corresponding approximately to 25 and 19 cm wavelengths, respectively. The assigned frequency range provides an adequate setting for the signals to propagate through the atmosphere and reach the user at almost any weather condition. The coexistence of GNSS signals from several independent constellations, e.g. the US Global Positioning System (GPS), the Russian GLObal NAvigation Satellite System (GLONASS), European Galileo, Chinese Beidou, Japanese Quasi-
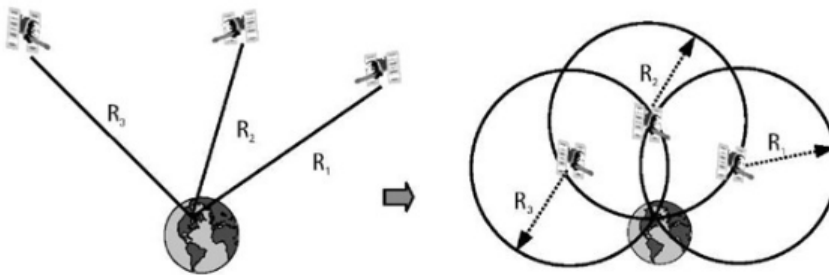
Figure 2.1: Fundamental concept of GNSS positioning.

Zenith Satellite System (QZSS), and Indian Regional Navigation Satellite System (IRNSS) increases the number of the observations. The high number of observations makes a positive contribution to the position accuracy, availability, integrity, and continuity of the GNSS services [23].

Most GNSS satellites use a near-circular Medium Earth Orbit (MEO) to provide global coverage. However, some of the satellites are in Inclined Geosynchronous Orbits (IGSO), or Geostationary Orbits (GEO) for regional applications [30]. The GPS satellites use L1 (1575.42MHz) and L2 (1227.6 MHz) frequencies as carrier signals. Different codes are modulated on the carrier signals for Standard and Precise Positioning Services (SPS and PPS). Authorized users can use PPS based on an encrypted Precise (P) code modulated on both L1 and L2. Civilian users have access to SPS by utilizing Coarse/Acquisition (C/A) code available only on L1. A new civil signal (L2C) on L2 and a new military signal (M) on L1 and L2 are implemented within the GPS modernization program. Additionally, the new L5 signal with the frequency of 1176.45 MHz has been implemented on some of the GPS satellites since May 2010 [30].

The GLONASS satellites transmit signals within two bands: Ll, 1602 - 1615.5 MHz, and L2, 1246 - 1256.5 MHz. A new generation of the satellites in this constellation has a new link, i.e., L3, with a frequency of 1202.025 MHz. Galileo satellites utilize three frequency bands, i.e., E1 (centered on 1575.46 MHz), E6 (centered on 1278.75 MHz), and E5 (centered on 1191.795 MHz), to provide three levels of service called the Open Service (OS), the Public Regulated Service (PRS), and the Commercial Service (CS) [30]. BeiDou satellites provide open and authorized services using three frequency bands, including B1 (1561.098 MHz), B2 (1207.14 MHz), and B3 (1268.52 MHz). A new generation of this constellation called BeiDou-3 is designed to transmit modernized signals at the L1/E1 and L5/E5 bands as well as the BeiDou B3 frequency [30]. Table 2.1 provides an

overview of the operational GNSS constellations. The studies conducted within this thesis are mainly based on the GPS L1 and L2 frequencies.

2.2 Signal specifications

The propagation of transmitted GNSS signals through space is described by Maxwell's theory. Using Maxwell equations (see e.g. [28]), the fundamental wave equations are as follows [38]:

$$\nabla^2 \mathbf{E} = \varepsilon \mu \frac{\partial^2 \mathbf{E}}{\partial t^2} \tag{2.1}$$

$$\nabla^2 \mathbf{B} = \varepsilon \mu \frac{\partial^2 \mathbf{B}}{\partial t^2} \tag{2.2}$$

where $\mathbf{E}$ and $\mathbf{B}$ are the electric and magnetic fields, respectively, the operator ∇^2 is vectorial Laplacean, t is time, and the constants ε and μ respectively denote the

Table 2.1: An overview of the operational constellations of Global Navigation Satellite Systems (GNSS) [30]. The orbit types of the satellites are Medium Earth Orbit (MEO), Geostationary orbit (GEO), and Inclined Geosynchronous Orbit (IGSO).

System	GPS	GLONASS	Galileo	BeiDou	QZSS	IRNSS/NavIC
Orbit	MEO	MEO	MEO	MEO, IGSO, GEO	GEO, IGSO	GEO, IGSO
Nominal satellites	24	24	30	27, 3, 5	1, 3	3, 4
Orbit inclination	56°	64.8°	56°	55°	43°	29°
Initial service	1993	1993	2016	2012	2018	2018
Origin	USA	Russia	Europe	China	Japan	India
Frequency (MHz)	L1 1575.42 L2 1227.60 L5 1176.45	L1 1602.00 L2 1246.00 L3 1202.025	E1 1575.42 E5a 1176.45 E5b 1207.14 E6 1278.75	B1 1561.098 B2 1207.14 B3 1268.52	L1 1575.42 L2 1227.60 L5 1176.45 LEX 1278.75	L5 1176.45 S 2492.028

electrical permittivity and magnetic permeability of the medium through which the signals propagate. A solution to 2.1 can be described by the following equation [38]:

$$\mathbf{E}(\mathbf{r}, t) = \mathbf{E_0} \cos\left(\mathbf{k}.\mathbf{r} - k c t + \phi_0\right), \quad \mathbf{k} = k \, \mathbf{n_0} \tag{2.3}$$

where $\mathbf{r} = (x, y, z)$ is the position vector, $\mathbf{E_0}$ identifies the strength of the electrical field, $\mathbf{k}$ denotes wave vector, $k = \frac{2\pi}{\lambda}$ is wave number, λ refers to the wavelength, $\mathbf{n_0}$ is a unit vector showing the direction of propagation, c is the speed of light, and ϕ_0 denotes zero-phase offset. If $\mathbf{E_0}$ and $\mathbf{k}$ are perpendicular, which is usually the case regarding the satellite navigation signals, then the wave is a transverse wave. Magnetic wave $\mathbf{B}$ follows similar considerations. The magnetic and electrical fields are both orthogonal to each other, as well as the propagation direction denoted by $\mathbf{n_0}$.

If the electric field or magnetic field oscillates within a plane along $\mathbf{k}$, the electromagnetic wave has linear polarization (Figure 2.2, left). The propagation of electromagnetic waves through the ionosphere or Earth magnetic field can alter linearly polarized waves to elliptically or circularly polarized waves [23]. This issue has been addressed for the navigation signals by using a circular polarization design.

To create a circularly polarized electromagnetic wave, two perpendicular electric waves with similar wave vectors ($\mathbf{k}$) and strengths ($||\mathbf{E_0}||$) can be superposed while the zero-phase offsets (ϕ_0) differ by 90° [38]. The strength of this electrical field at a given location $\mathbf{r}$ over time exhibits a circular variation (Figure 2.2, right). A clockwise rotation of the wave, when looking into the propagation direction, indicates a Right-Handed Circular Polarization (RHCP), and a counter-clockwise rotation is associated with a Left-Handed Circular Polarization (LHCP). All GNSS satellites transmit the navigation signals with RHCP. This setting avoids possible power losses due to orientation mismatch of the incoming electromagnetic field, and the receiving antenna [38].

All GNSS signals are transmitted with a modulated characteristic binary sequence called Pseudo-Random Noise (PRN) code at a typical rate of 1 to 10 MHz with a repetition period of a few milliseconds to seconds [30]. The modulation scheme used in GPS satellites is illustrated in Figure 2.3. The PRN code can be used as an identifier to separate the signals with the same frequency from different satellites. The modulated signals include the time of transmission and other required information encapsulated in the data messages to derive the satellites-receiver ranges and the position of the satellites.

Calculating the ranges is based on the estimation of the time delay between the received signal and the transmission time. To estimate the time delay, the receiver
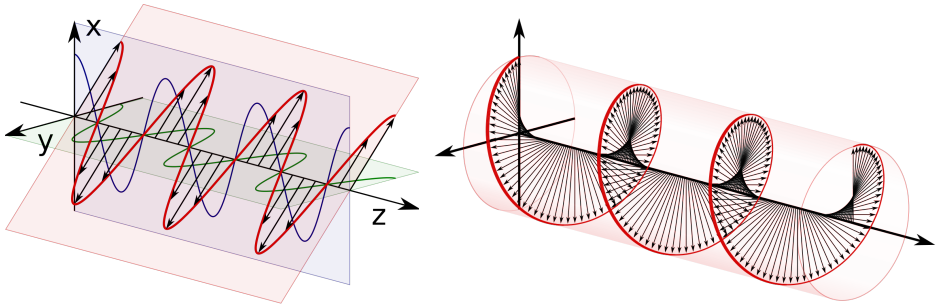
Figure 2.2: Linearly (left) and circularly (right) polarized waves.
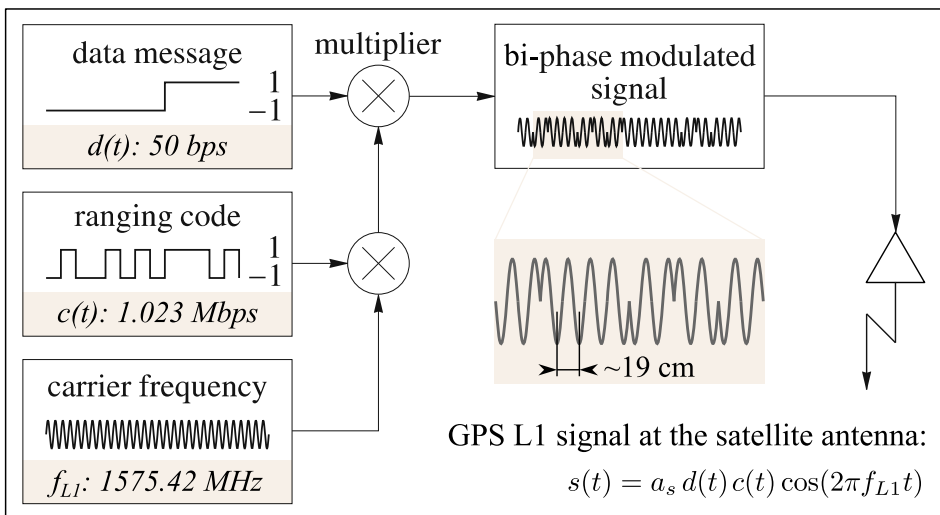
Figure 2.3: A schematic representation of phase modulation of data message and ranging code layers on GPS carrier signals, originally presented by [23]. The parameter a_s is the modulation amplitude.

correlates the received signal with a local replica of the satellite's PRN code. Besides the time delay, another factor also influences the correlation, i.e., the Doppler effect. The effect is caused due to the relative satellite-receiver movement, which introduces a frequency shift in the GNSS signals known as Doppler frequency. Therefore, the correlation of the PRN replica with the received signal is a function of the code delay and Doppler shift. The receiver searches for the code delay and Doppler shift that produce the maximal correlation value. The detection can be done by producing a delay-Doppler Map (DDM) in the receiver. The DDM reveals the variation of correlation value at different code-delays and Doppler shifts (Figure 2.4).
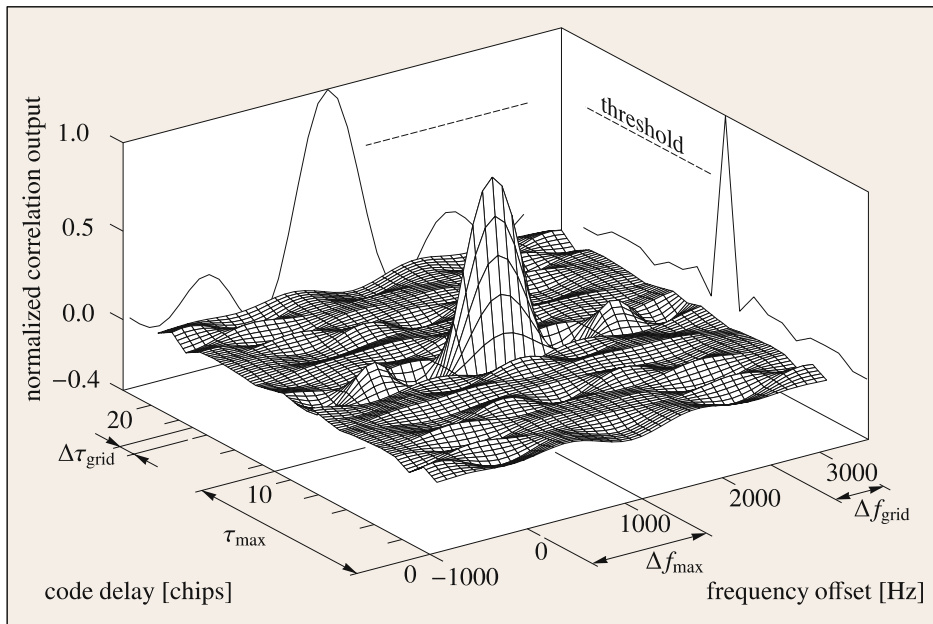
Figure 2.4: An exemplary Delay-Doppler Map (DDM), that is generated in typical GPS receivers (image source: [23]).

GNSS receivers can make the following measurements using the received signals [30, 23]:

- *Code range or Pseudorange:* A measure of the delay between the signal reception and transmission time based on the receiver clock which can be scaled by the speed of light to yield the so-called Pseudorange. This measurement estimates the distance traveled by the signal from the satellite to the receiver.

- *Carrier phase:* Besides the PRN replica, a local oscillator in the receiver generates a signal with a frequency similar to the incoming carrier signal. Any deviation between the generated and incoming signals results in a beat frequency and a beat phase. A measure of the beat phase can be used to retrieve the phase of the satellite signal. Measurement of the carrier phase can precisely report on the change in the pseudorange.

- *Doppler frequency:* A measure of the Doppler frequency provides information about the range-rate or line-of-sight velocity.

2.3 Receiver architecture

A conceptual block diagram of a typical GPS receiver architecture is shown in Figure 2.5. The components depicted in the figure are further elaborated in Figure 2.6 to Figure 2.8. The components perform the essential parts of the signal processing procedure on the user side. The variables used in the figures are as follows: a_r is the amplitude of the incoming signal at the receiver antenna, A is the amplitude of the received signal in the receiver, d and c are respectively the modulated data messages and PRN code as functions of time (t) and the path delay (τ), f_{L1} is the GPS L1 frequency, f_D is the Doppler frequency, and f_{IF} is the intermediate frequency. The hat symbol ($\hat{\bullet}$) is used to show an estimation of the respective parameter, e.g., $\hat{f}_D$ indicates an estimation of f_D. The variable φ_0 is the initial phase of the signal when it arrives at the receiver antenna, φ_{IF} is the initial phase of the intermediate frequency, $\Delta\varphi = \varphi_0 - \varphi_{IF}$ and $\delta\varphi = \Delta\varphi - \hat{\Delta\varphi}$ are used for the phase differences, and T_{CI} is the coherent integration time that can be from a few milliseconds usually up to 20 milliseconds.
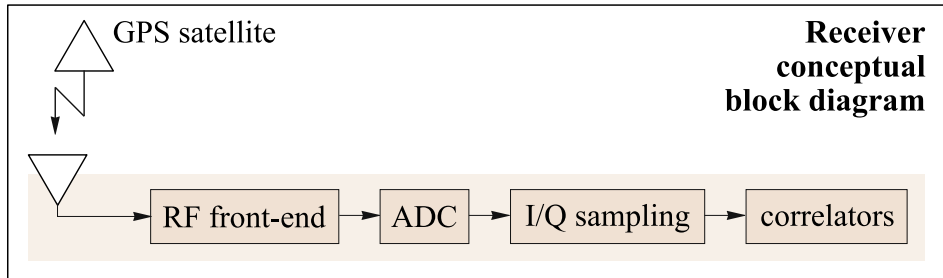
Figure 2.5: The fundamental components of a typical GPS receiver including the Radio Frequency (RF) front-end, Analog to Digital Converter (ADC), In-phase/Quadrature (I/Q) sampling unit, and correlators.

The antenna intercepts incoming signals from any GPS satellites in view and feeds the receiver with a mixture of all intercepted signals (Figure 2.6). Before starting the signal processing procedure, a Low-Noise Amplifier (LNA) increases the strength of the captured signals at the antenna. The receiver front-end shown in Figure 2.6 includes several band-pass filters, a local oscillator, and a mixer to provide a signal at a much lower frequency compared to the carrier frequency. The down-converted signal with a lower frequency is called Intermediate Frequency (IF) and has a frequency that is appropriate for the digitization of the signal in the Analog to Digital Converter (ADC).

The digitized signal from the ADC contains the navigation data message, $d(t - \tau)$, and PRN codes, $c(t - \tau)$, of different GPS satellites. To retrieve PRN code delay

GPS L1 signal at the receiver antenna: **Receiver**
$S(t) = a_r\, d(t-\tau)\, c(t-\tau)\cos(2\pi(f_{L1} + f_D)t + \varphi_0)$ **front-end**

low-noise amplifier

$S(t) = A\, d(t-\tau)\, c(t-\tau)\big[$
$\cos(2\pi(f_D + f_{IF})t + \varphi_0 - \varphi_{IF}) +$
$\cos(2\pi(2f_{L1} + f_D - f_{IF})t + \varphi_0 + \varphi_{IF})\big]$

band pass filter $\times$ band pass filter centered on f_{IF}

$\cos(2\pi(f_{L1} - f_{IF})t + \varphi_{IF})$ $A\, d(t-\tau)\, c(t-\tau)\cos(2\pi(f_D + f_{IF})t + \Delta\varphi)$

to the analog to digital converter
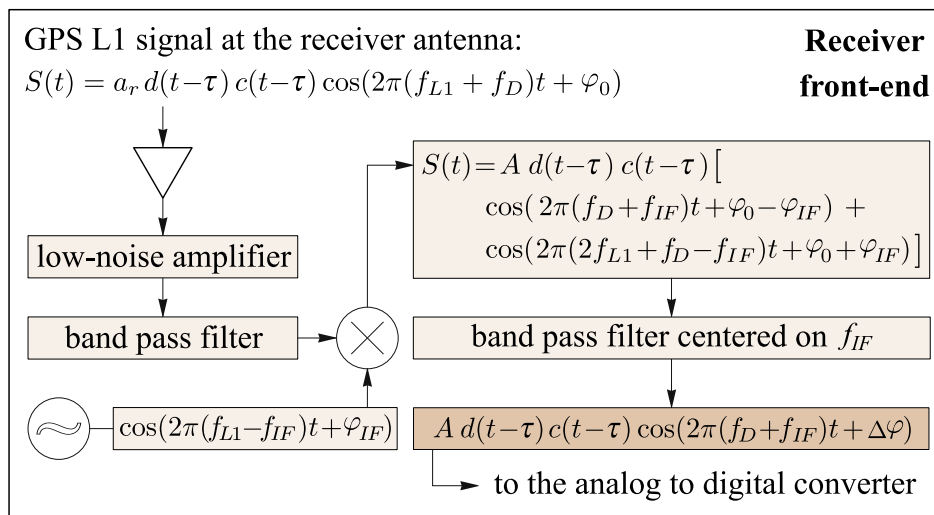
Figure 2.6: A block diagram of the signal processing steps in the receiver frond-end, produced based on the description presented in [58].

and the navigation data, the trigonometric term of the signal, i.e., the cosine term, needs to be wiped off. For this purpose, the exact frequency and phase of the digitized signal are required. The frequency is slightly different from the IF frequency due to the Doppler effects, which are unknown and are different for different GPS satellites. Therefore, the receiver cannot completely eliminate the trigonometric term, which results in a remaining residual frequency. The residual frequency can introduce some slow-varying oscillation in the signal that can affect the correlation value between the PRN replicas and the digitized signal. The receiver uses an In-phase/Quadrature (I/Q) method (Figure 2.7) to address this issue. The method provides two outputs in separate I/Q channels to allow preserving correlation power through the following trigonometric equation:

$$[M\cos(\bullet)]^2 + [M\sin(\bullet)]^2 = M^2 \tag{2.4}$$

The I/Q samples are duplicated to many channels to feed parallel correlators. Each channel can be dedicated to correlating the signal against one specific PRN code. An estimate of the code delay and Doppler shift is applied in each correlator before calculating the correlation between the replica and I/Q samples. For every pair of the code-delay and Doppler shift estimates, one correlation output is produced. The correlation outputs for a range of different code-delays and Doppler shifts can form the DDM as shown in Figure 2.4. After forming the DDM, the peak value of the correlation in the DDM is detected by the receiver, and the corresponding

> Digitized signal from ADC: **I/Q sampling**
>
> $A\,d(t-\tau)\,c(t-\tau)\cos(2\pi(f_D+f_{IF})t+\Delta\varphi)$
>
> in-phase (I)   quadrature (Q)
>
> $2\cos(2\pi(f_{IF}+\hat{f}_D)t+\hat{\Delta}\varphi)$ $-2\sin(2\pi(f_{IF}+\hat{f}_D)t+\hat{\Delta}\varphi)$
>
> low pass filter   I $A\,d(t-\tau)\,c(t-\tau)\cos(2\pi(f_D-\hat{f}_D)t+\delta\varphi)$ low pass filter
>
> $A\,d(t-\tau)\,c(t-\tau)\sin(2\pi(f_D-\hat{f}_D)t+\delta\varphi)$ Q
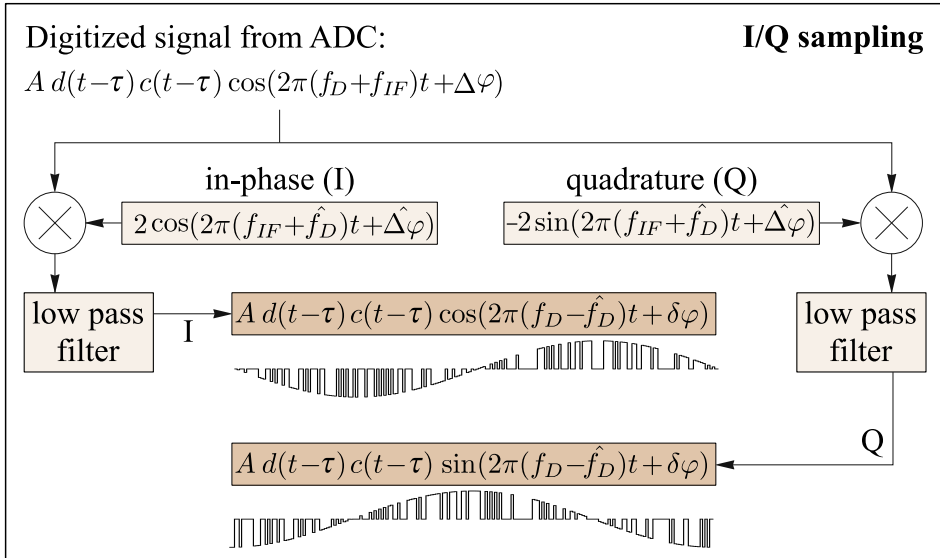
Figure 2.7: A block diagram of the signal processing steps during In-phase and Quadrature (I/Q) sampling. The ADC refers to the analog to digital converter, produced based on the description presented in [58].

delay and Doppler are retrieved. The retrieved delay and Doppler values are used to provide the fundamental GPS observables by the receiver, i.e., pseudorange, Doppler frequency, and carrier phase. The peak value of the correlation sum in the DDM can provide an estimate for the received signal strength. More details about the signal processing scheme in the receiver can be found in, e.g., [30, 23, 58].

2.4   Interference of the direct and reflected signals

The received signal in the receiver can be a compound signal generated by the interference of the direct signal and some reflections from nearby surfaces. In this case, the contribution of reflected signals can affect the peak correlation power in the DDM. The interference of the reflections with direct signals is considered as an error source in positioning and navigation applications. Nevertheless, this phenomenon is utilized in the GNSS-Reflectometry (GNSS-R) technique to characterize the surface the signals are reflected from. For instance, reflections from sea surface can be collected and processed to retrieve sea surface height or sea state.

In this thesis, we use a dedicated reflectometry receiver with multiple antenna inputs. The details about this receiver and the experimental site can be found in [21, 26, 47]. The first antenna input of this receiver is called the master link. The

Outputs from I/Q sampling: **Correlators**

in-phase channel: $A\, d(t-\tau)\, c(t-\tau) \cos(2\pi(f_D - \hat{f}_D)t + \delta\varphi)$

quadrature channel:

$A\, d(t-\tau)\, c(t-\tau) \sin(2\pi(f_D - \hat{f}_D)t + \delta\varphi)$

locally generated
PRN replica:

$c(t-\hat{\tau})$

$$\Sigma_Q = \frac{A\,d}{T_{CI}} \int_0^{T_{CI}} c(t-\hat{\tau})\, c(t-\hat{\tau}) \sin(2\pi\Delta f_D t + \delta\varphi)\, dt$$

correlator output
for each $\hat{\tau}$ and $\hat{f}_D$:

$\Sigma_I^2 + \Sigma_Q^2$

$$\Sigma_I = \frac{A\,d}{T_{CI}} \int_0^{T_{CI}} c(t-\hat{\tau})\, c(t-\hat{\tau}) \cos(2\pi\Delta f_D t + \delta\varphi)\, dt$$
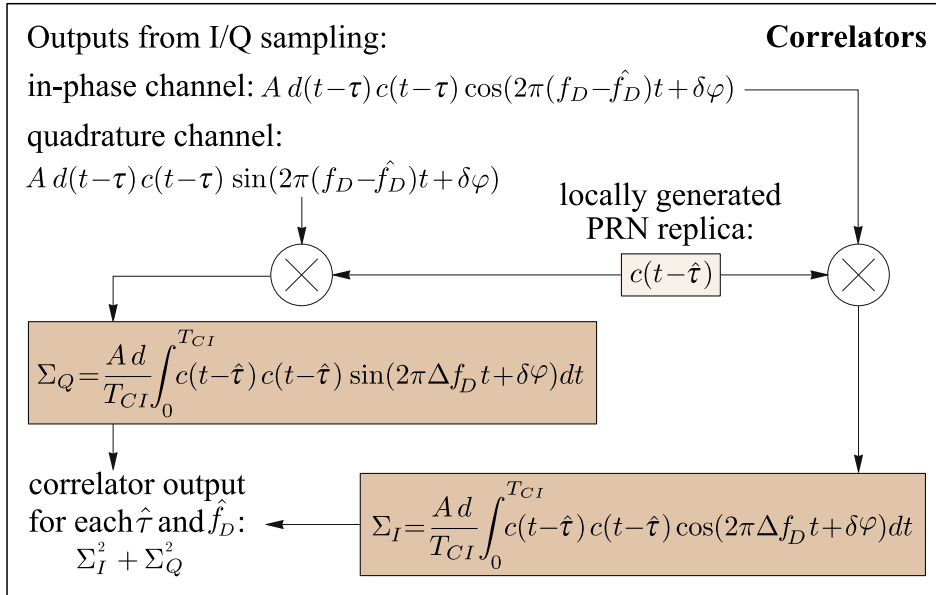
Figure 2.8: A block diagram of a correlator channel in the receiver, produced based on the description presented in [58].

master antenna is used for tracking direct signals similar to typical GPS receivers with the procedure described in section 2.3. The other antennas are called slave links and can be used to capture reflections from the target surfaces. In the following, we investigate the effect of reflected signals on the power of received signals in the master and slave antennas. We use the complex numbers system to simultaneously work with the outputs of I/Q channels in a unified formulation. The real part of the complex numbers is used for the in-phase channel and the imaginary part for the quadrature channel. In this sense, the symbol j indicates the imaginary unit ($j^2 = -1$).

As illustrated in Figure 2.9(a) and Figure 1 in [31], the intercepted direct and reflected signals in the master antenna can be expressed by:

$$\mathbf{A_c} = \mathbf{A_d} + \mathbf{A_r} \tag{2.5}$$

$$A_c e^{j\varphi_c} = A_d\, e^{j\varphi_d} + A_r\, e^{j(\varphi_d + \psi)} \tag{2.6}$$

where A_d, A_r, and A_c are respectively the amplitude of direct, reflected, and compound signals. Correspondingly, the phase values for these signals are φ_d, φ_r, and φ_c. The phase difference between the direct and reflected signals is represented by ψ. The phase of the direct signal comprises several components, i.e., the traveling path from the GNSS satellite to the receiver (including atmospheric refraction)

denoted by φ_ρ, phase wind-up shown by φ_w, and Phase Center Variations (PCV) indicated by φ_{pcv}:

$$\varphi_d = \varphi_\rho + \varphi_w + \varphi_{pcv} \tag{2.7}$$
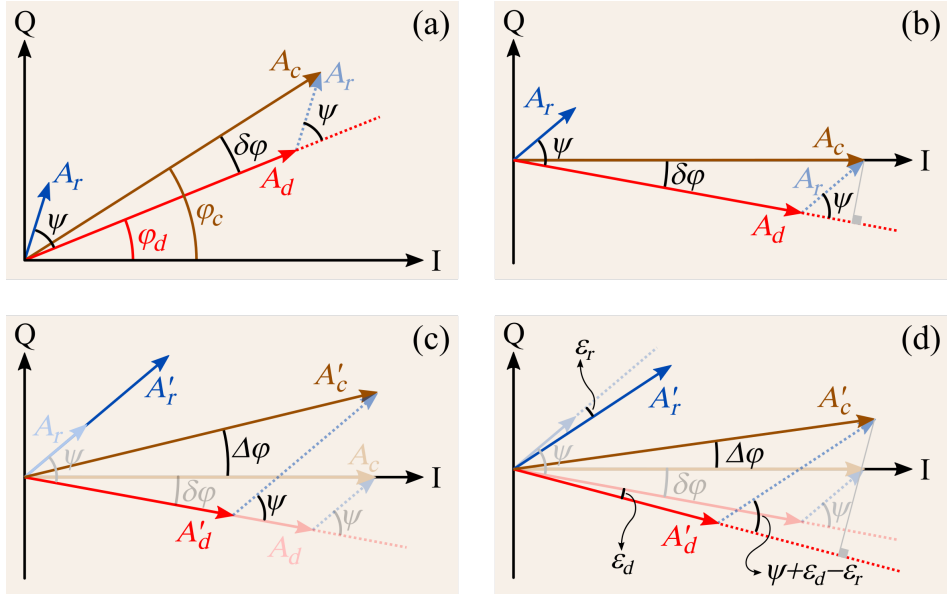
Figure 2.9: Phasor representation of the In-phase (I) and Quadrature (Q) components of the received direct and reflected GNSS signals at the receiver: (a) before tracking the phase of the compound signal (generated by the interference of the direct and reflected signals) in the master channel, (b) after tracking the phase of the compound signal in the master channel. The same value of the tracked phase in the master channel is applied to the slave channel and represented in (c) a simplified model and (d) a model including the phase contributions from other factors, e.g., possible baseline between the master and slave antennas. Panels (a) to (c) are reused from [47].

The receiver tracks the phase of the compound signal in the master channel. After tracking, the compound signal will have only an in-phase component as it is shown in Figure 2.9(b). In this case, the quadrature component which is expressed by the imaginary part in Equation 2.6 will be vanished, resulting in:

$$[A_c e^{j\varphi_c} = A_d e^{j\varphi_d} + A_r e^{j(\varphi_d+\psi)}].e^{-j\varphi_c} \tag{2.8}$$

$$A_c = A_d e^{j(\varphi_d-\varphi_c)} + A_r e^{j(\varphi_d+\psi-\varphi_c)} \tag{2.9}$$

$$= A_d e^{-j\delta\varphi} + A_r e^{j(\psi-\delta\varphi)} \tag{2.10}$$

$$= e^{-j\delta\varphi}.(A_d + A_r e^{j\psi}) \tag{2.11}$$

where the in-phase (I) and quadrature (Q) components of the master channel output are:

$$I_m = A_d \cos(\delta\varphi) + A_r \cos(\psi - \delta\varphi) = A_c \qquad (2.12)$$
$$Q_m = -A_d \sin(\delta\varphi) + A_r \sin(\psi - \delta\varphi) = 0 \qquad (2.13)$$

with subscript m referring to the master channel. From Figure 2.9(b), the value of the phase difference between the direct and compound signals ($\delta\varphi$) can be derived using:

$$\tan(\delta\varphi) = \frac{\sin(\delta\varphi)}{\cos(\delta\varphi)} = \frac{\frac{A_r \sin(\psi)}{A_c}}{\frac{A_d + A_r \cos(\psi)}{A_c}} = \frac{A_r \sin(\psi)}{A_d + A_r \cos(\psi)} \qquad (2.14)$$

The following equation can be used to calculate $e^{-j\delta\varphi}$:

$$e^{-j\delta\varphi} = \cos(\delta\varphi) - j\sin(\delta\varphi) \qquad (2.15)$$

$$= \frac{A_d + A_r \cos(\psi) - jA_r \sin(\psi)}{A_c} = \frac{A_d + A_r e^{-j\psi}}{A_c} \qquad (2.16)$$

The Signal-to-Noise Ratio (SNR) observations, similar to geodetic receivers' SNR, can be worked out by applying the law of cosines in Figure 2.9(b):

$$A_c^2 = I_m^2 = A_d^2 + A_r^2 + 2A_d A_r \cos\psi \qquad (2.17)$$

As can be seen from the latter formula, the SNR value does not depend on $\delta\varphi$. In contrast, the in-phase component of the master channel, before squaring, depends on $\delta\varphi$ and should be accounted for in the analysis.

The phase rotation applied to the master channel to track the phase of the compound signal is concurrently applied to the slave channels. A tilted orientation would be favorable for the slave antennas since they are usually utilized to capture reflections from land or sea surfaces. Such an orientation can amplify the received reflections by assigning higher antenna gains to the reflected signals. Depending on the polarization of the tilted antenna, the intercepted direct and reflected signals would have different magnitudes. The effect of polarization of the reflected signals in association with the polarization design of the slave antenna is discussed in section 2.4.1. Figure 2.9(c) depicts the phasor diagrams for the slave channel. The amplitudes of the direct and reflected signals are changed due to the antenna gain factor. For simplicity, this panel does not show the other affecting factors, including the baseline effects between master and slave antennas, the effect of different phase wind-ups, and the phase center offset and variation. These effects are

summarized by ε_d and ε_r for the direct and reflected signals, respectively (see Figure 2.9(d)). Therefore, the compound signal in the slave channels can be expressed in the following form:

$$A'_c e^{j\Delta\varphi} = A'_d e^{-j(\delta\varphi+\varepsilon_d)} + A'_r e^{j(\psi-\delta\varphi-\varepsilon_r)} \tag{2.18}$$

$$A'_c e^{j\Delta\varphi} = e^{-j\delta\varphi} \cdot (A'_d e^{-j\varepsilon_d} + A'_r e^{j(\psi-\varepsilon_r)}) \tag{2.19}$$

$$A'^2_c = I^2_s + Q^2_s \tag{2.20}$$

$$= A'^2_d + A'^2_r + 2A'_d A'_r \cos(\psi + \varepsilon_d - \varepsilon_r) \tag{2.21}$$

where the prime symbol $'$ is used to distinguish the amplitudes in the slave channel from those in the master channel. The formulation introduced in this section only accounts for RHCP reflected signals. A possible contribution from LHCP reflected signals is discussed and formulated in the following section.

2.4.1 Ellipticity and polarization of the reflected signals

Here, the direct signals are considered to be pure RHCP signals. However, the polarization of direct GPS signals can be slightly elliptical. According to the GPS documentation (IS-GPS-200M), the ellipticity of GPS L1 signal is below 1.2 dB for Block IIA satellites and 1.8 dB for Block IIR/IIR-M/IIF/III/IIIF satellites. Regarding the L2 signal, the ellipticity shall be no worse than 3.2 dB for Block II/IIA satellites and 2.2 dB for Block IIR/IIR-M/IIF and GPS III/IIIF satellites. These ellipticity limits are considered to be valid over the angular range of ± 13.8 degrees from the GPS satellite's nadir.

The nearly circular polarization of direct GPS signals can significantly change upon reflection. Consequently, reflected GPS signals can generally be regarded as elliptically polarized signals with RHCP and LHCP components. Common geodetic antennas have an RHCP design. These antennas are configured in a way that the possible LHCP component of the incoming signal is suppressed. For reflectometry receivers with multiple antenna inputs, an RHCP design with upward orientation (or slightly tilted from the zenith) is usually considered for the master antenna, similar to that of geodetic antennas. This setting assigns higher antenna gains to the incoming direct signals and facilitates the signal tracking processes. However, while an RHCP antenna almost mitigates the possible LHCP component of the direct signals, the signature of the LHCP component of reflected signals can be clearly visible at certain incoming angles for some of the geodetic antennas. Figure 2.10 shows the gain patterns of an RHCP antenna used in this thesis in two different orientations. The left panel is related to the zenith-looking orientation

used as the master antenna, and the right panel shows the side-looking orientation, i.e., a tilt of 90 degrees with respect to the zenith, used as a slave antenna. The co-polarization gain of the antenna, which indicates reception performance for RHCP signals, is shown by blue color, and the cross-polarization reception, i.e., LHCP signal, is shown by red color. Dashed lines show the gain values associated with reflected signals.
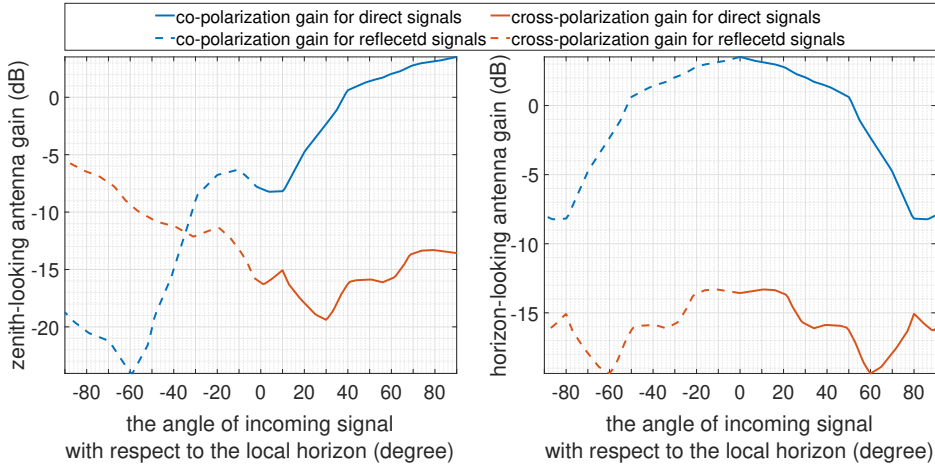
Figure 2.10: An exemplary antenna gain pattern for Right- and Left-Handed Circular Polarization signals (RHCP and LHCP) referred respectively here as co- and cross-polarization receptions with respect to the RHCP design of the direct signals. Left panel is related to a zenith-looking orientation for the antenna and right panel shows a horizon-looking orientation. The gain values are retrieved from [42].

As can be seen from Figure 2.10, the cross-talk gain of the antenna, i.e., the LHCP reception gain, can be significant for angles below -20° with respect to the zenith-looking antenna's ground plane. To account for the cross-talk component in the received signal at the receiver, Equation 2.6, which follows the simplified representation of the reflected signal in Figure 2.9(c), can be elaborated as:

$$A_c e^{j\varphi_c} = A_d \, e^{j\varphi_d} + A_{r_+} \, e^{j(\varphi_d + \psi_+)} + A_{r_-} \, e^{j(\varphi_d + \psi_-)} \tag{2.22}$$

where A_{r_+} and A_{r_-} are the amplitudes of the co-polarization (RHCP) and cross-polarization (LHCP) components of the reflected signal, respectively. Different factors contribute to the phase of the reflected signals. The direct-reflected signals phase difference for the co- (ψ_+) and cross-polarization (ψ_-) components of the

reflected signal can have the following elements:

$$\psi_+ = \psi_{\delta\rho} + \psi_{w_+} + \psi_{R_+} + \psi_{\delta pcv_+} \tag{2.23}$$

$$\psi_- = \psi_{\delta\rho} + \psi_{w_-} + \psi_{R_-} + \psi_{\delta pcv_-} \tag{2.24}$$

with $\psi_{\delta\rho}$ being the phase due to the extra path traveled by the reflected signal as shown in Figure 2.11(a). ψ_{w_+} and ψ_{w_-} are the phase wind-up effects (see e.g., [7]) for co- and cross-polarization reflected signals, respectively. ψ_{R_+} and ψ_{R_-} are the phase changes due to the Fresnel reflection coefficients for co- and cross-polarization reflected signals, respectively. The formulas do not include any phase changes due to the sea surface roughness. Similar to the PCV parameter for the direct signal, the reflected signals at the antenna would manifest different phase delays based on the angle of reception. The corresponding effect, which is shown in Figure 2.11(b), is denoted by $\psi_{\delta pcv_+}$ and $\psi_{\delta pcv_-}$ for the RHCP and LHCP components of the reflected signal, respectively. An exemplary PCV pattern for GPS L1 signal in an RHCP antenna is depicted in Figure 2.12.
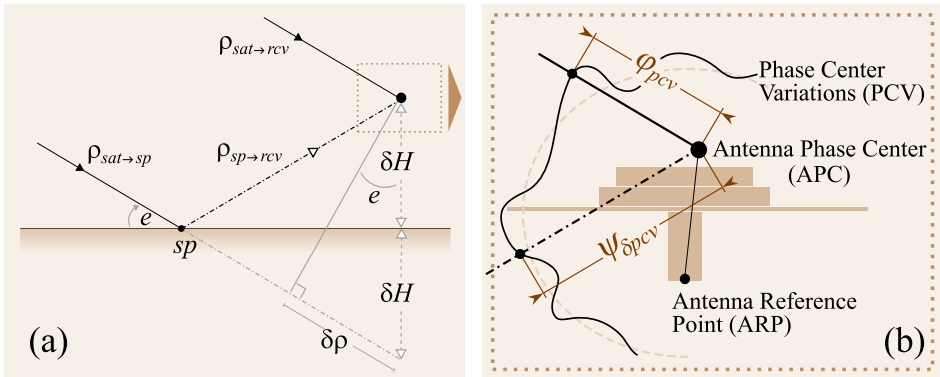
Figure 2.11: (a) The extra path traveled by the reflected signal in a ground-based GNSS-Reflectometry setting, (b) the Phase Center Variations (PCV) of the antenna for the direct and reflected signals. The parameter ρ is used for the signal path with subscript *sat*, *sp*, and *rcv* respectively denoting the satellite, reflection point, and receiver. δH is the height difference between the reflecting surface and the receiver antenna, and e refers to the elevation angle of the satellite. The variables φ_{pcv} and $\psi_{\delta pcv}$ are the phase residuals due to the PCV for the direct and reflected signals, respectively.

An analysis of the parameters in Equation 2.22 is given as follows, starting with the amplitudes A_d, A_r. The amplitudes of the received direct and reflected signals in the receiver from the master antenna vary due to several factors, one of which is the antenna gain factor. Moreover, the receiver applies an Automatic Gain Controller (AGC) factor to adjust the received signal power. The AGC factor would be similar for each antenna input. These two factors, i.e., the antenna gain and AGC, will be

	North	East	Up
PCO [mm]	0.48	0.89	5.76
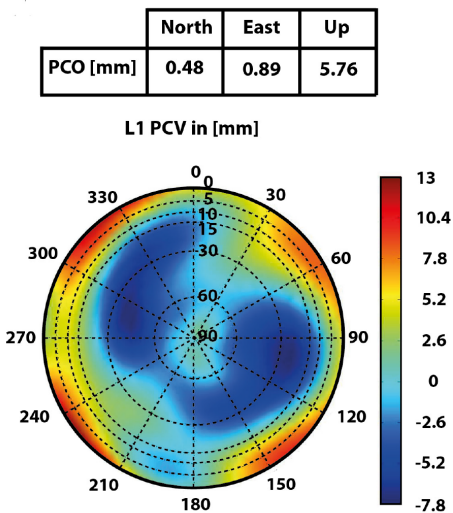
Figure 2.12: An example of the antenna Phase Center Offset and Variation (PCO and PCV) for GPS L1 signal in millimeter (image source: [35]).

indicated by F and k, respectively. The factor k is applied to the compound signal; therefore, it is the same for the direct and reflected signals. We keep using the subscript d and r to refer to the direct and reflected signals and the symbols $+$ and $-$ to denote the co- and cross-polarization components, respectively. Based on this:

$$A_d = k \, F_d \, U_d \tag{2.25}$$

$$A_{r_+} = k \, F_{r_+} \, U_{r_+} \tag{2.26}$$

$$A_{r_-} = k \, F_{r_-} \, U_{r_-} \tag{2.27}$$

where U_d and U_r are respectively the amplitudes of the direct and reflected signals immediately before reaching the antenna. Assuming that the gain and AGC values are available, the only unknown parameters will be U_d and U_r.

For ground-based GNSS-R with low reflector heights, one can assume that the amplitude of the direct signal before reaching the reflection point and before being intercepted by the antenna is almost the same. In this case, the amplitude of signal before and after reflection can be related through the following equation:

$$U_{r_+} = S(e, \sigma, \lambda) \, R_+(e, \varepsilon) \, U_d \tag{2.28}$$

$$U_{r_-} = S(e, \sigma, \lambda) \, R_-(e, \varepsilon) \, U_d \tag{2.29}$$

where S is a function that translates the random surface roughness to a dampening coefficient between 0 and 1. Here, the effect of roughness is assumed to be independent from the polarization. The standard deviation of the reflecting surface is

considered as a measure of surface roughness and is indicated by σ. The elevation angle of the satellite with respect to the reflecting surface is denoted by e. The function S also depends on the wavelength of the carrier signal (λ) and reads [40]:

$$S(e, \sigma, \lambda) = exp(-\frac{1}{2} \frac{(2\pi)^2}{\lambda^2} \sigma^2 \sin^2 e) \tag{2.30}$$

In Equation 2.28 and Equation 2.29, reflectivity of the surface and polarization change due to reflection are described by Fresnel reflection coefficients denoted by R. This factor is a function of the permittivity (ε) and elevation angle (e) and has the following forms [11]:

$$R_\parallel = \frac{\varepsilon_r \sin e - \sqrt{\varepsilon_{air} \varepsilon_r - (\varepsilon_{air} \cos e)^2}}{\varepsilon_r \sin e + \sqrt{\varepsilon_{air} \varepsilon_r - (\varepsilon_{air} \cos e)^2}} \tag{2.31}$$

$$R_\perp = \frac{\varepsilon_{air} \sin e - \sqrt{\varepsilon_{air} \varepsilon_r - (\varepsilon_{air} \cos e)^2}}{\varepsilon_{air} \sin e + \sqrt{\varepsilon_{air} \varepsilon_r - (\varepsilon_{air} \cos e)^2}} \tag{2.32}$$

with ε_r being the permittivity of the reflecting medium, $R_\parallel$ denoting the reflection with the polarization parallel to incidence plane, and $R_\perp$ indicating the reflection polarization perpendicular to the plane. The incidence plane, shown in Figure 2.13, is defined as a plane that contains the surface normal and the propagation vector of the incoming wave (wavevector). The coefficients $R_\parallel$ and $R_\perp$ (see Figure 2.14)
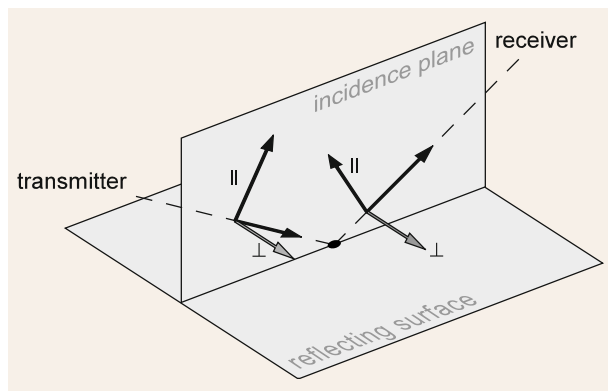
Figure 2.13: A sketch showing the incidence plane as well as the parallel and perpendicular components of the incoming and reflected waves. The figure is reused from [7].

can be combined to yield co- (R_+) and cross-polarization (R_-) forms of the Fresnel coefficients with respect to the incoming RHCP signals [11]:

$$R_+ = \tfrac{1}{2}(R_\parallel + R_\perp) \tag{2.33}$$

$$R_- = \tfrac{1}{2}(R_\parallel - R_\perp) \tag{2.34}$$
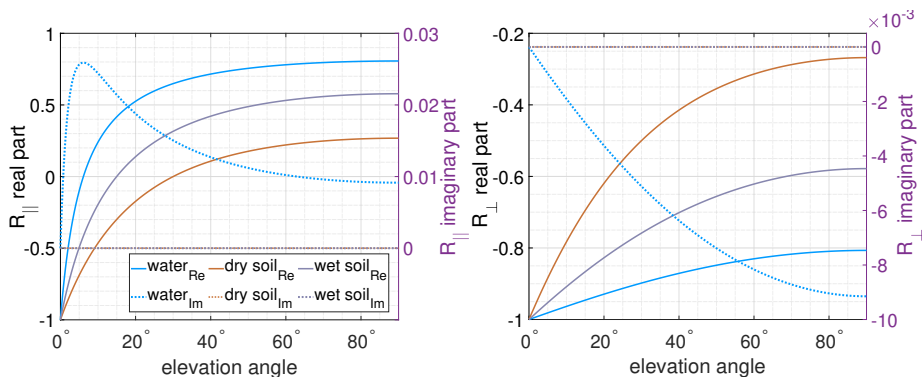
Figure 2.14: Real (*Re*) and imaginary (*Im*) parts of the parallel (left) and perpendicular (right) components of the Fresnel reflection coefficients for water, wet and dry soil. The imaginary parts of the permittivity for wet and dry soil are not considered here.
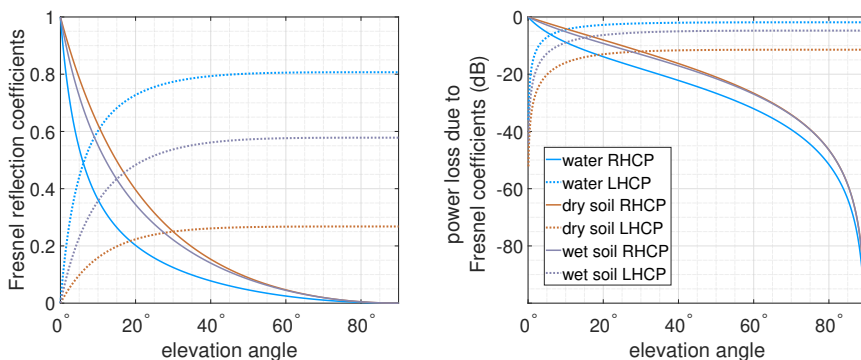
Figure 2.15: The RHCP and LHCP components of the Fresnel reflection coefficients with values ranging from 0 to 1 (left) and corresponding power losses in decibel (dB) (right) for water, wet and dry soil.

Figure 2.15 shows the variation of the co- and cross-polarization coefficients (left panel) and amount of power losses due to reflection (right panel) over different elevation angles for three reflecting surfaces. Among the three surfaces, the power loss in the RCHP component of the reflected signal from water (solid blue line in Figure 2.15) is the highest, and from dry soil is the lowest (solid brown line in the figure). This pattern is the opposite of the LHCP component (the dotted lines). Figure 2.16 and Figure 2.17 show the power loss variations due to the RHCP and LHCP Fresnel coefficients as a function of seawater salinity and temperature.

Now that all the elements of Equation 2.22 are described, we can use the formula for forward modeling of SNR observations. For this purpose, each term in Equa-
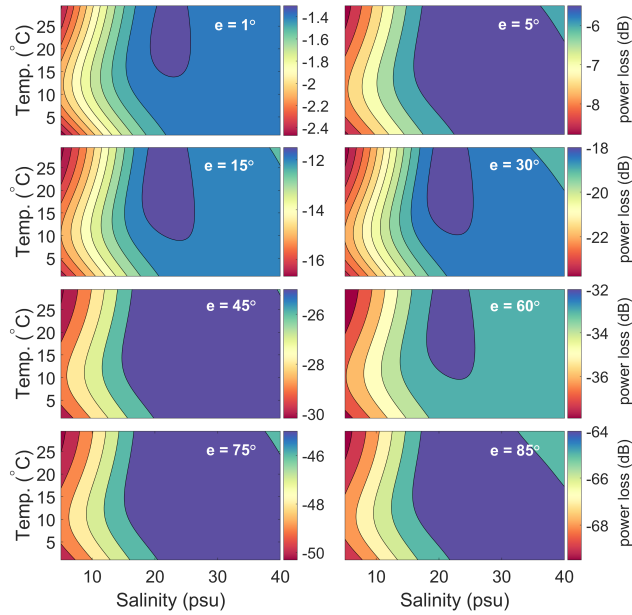
Figure 2.16: Power loss due to the co-polarization (RHCP) Fresnel reflection coefficient as a function of seawater salinity and temperature for different elevation angles.

tion 2.22 is constructed separately and is shown in Figure 2.18. The actual SNR observations are taken from a ground-based GNSS-R setup at Onsala, Sweden, using a dedicated GNSS-R receiver [26]. An estimated sea surface roughness of $\sigma = 6\ cm$ for the whole observation interval is used in the simulation. For the calculation of $\psi_{\delta\rho}$ sea level measurements from the nearest tide gauge are used. The amplitude of the direct signal before reaching the antenna (U_d) is considered to be almost constant over the interval.
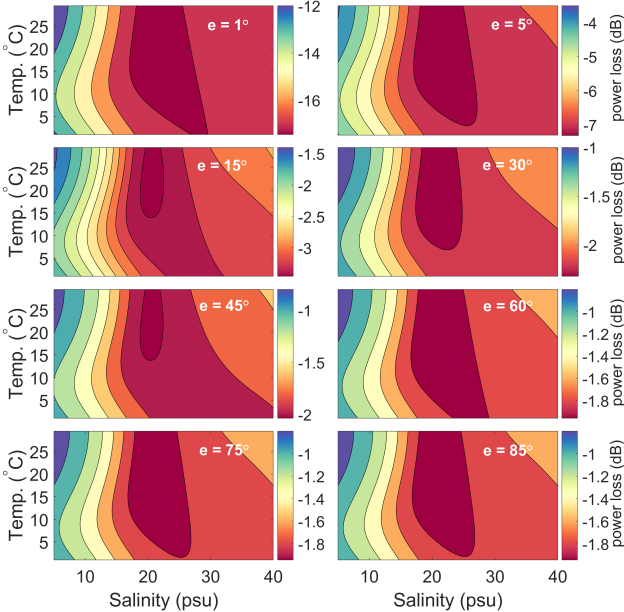
Figure 2.17: Power loss due to the cross-polarization (LHCP) Fresnel reflection coefficient as a function of seawater salinity and temperature for different elevation angles.
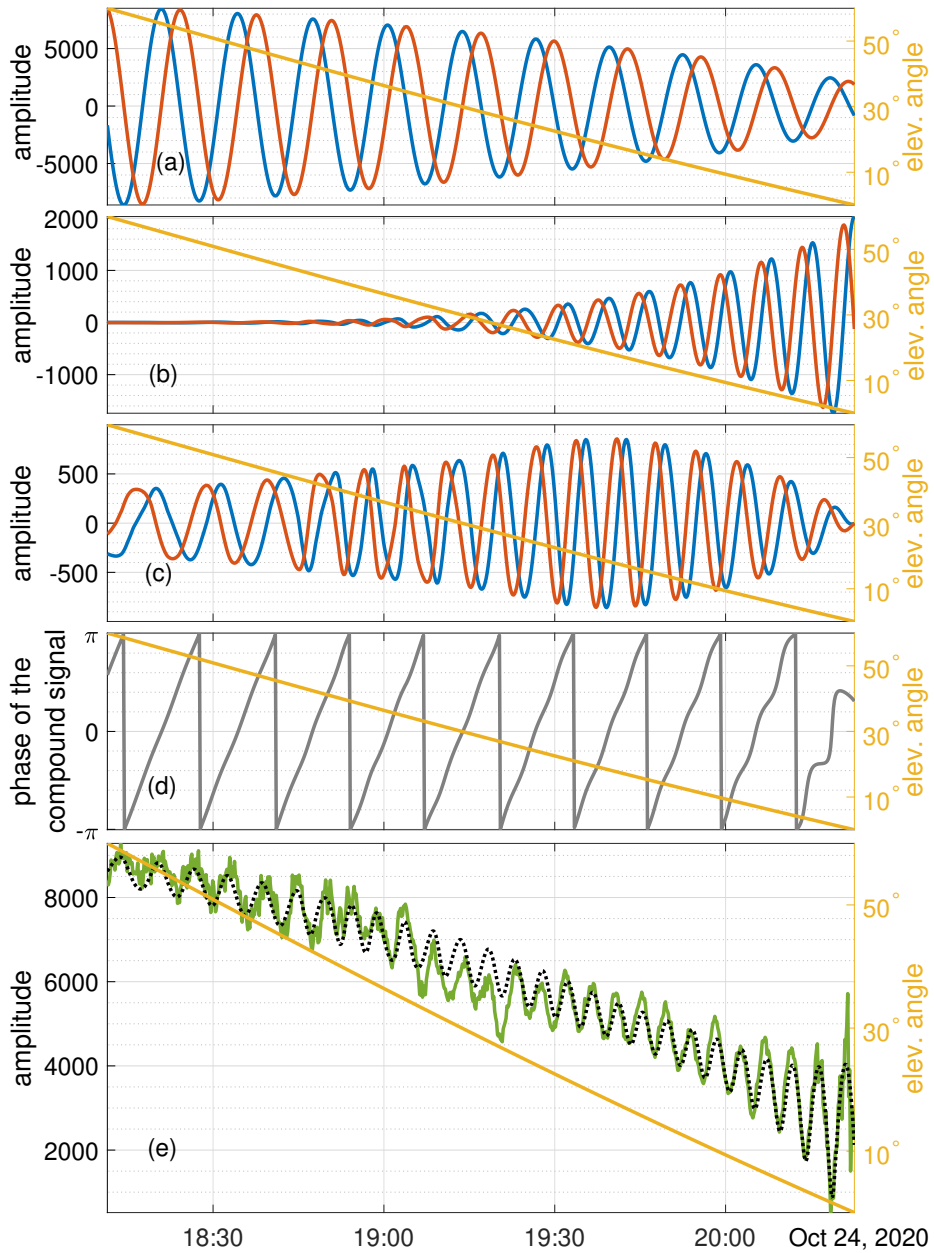
Figure 2.18: Reconstruction of different components of SNR observations from a zenith-looking antenna based on Equation 2.22: (a) contribution of the direct signal, (b) the RHCP component of the reflected signal, (c) the LHCP component of the reflected signal, (d) the phase of the compound signal, and (e) combination of the components (dotted line) overlaid on the actual observations (green line). The blue and red lines in panel (a) to (c) refer to the in-phase and quadrature components of the signals.

2.5   Direct and reflected GNSS signals for remote sensing

GNSS signals as sources of opportunity are being utilized for several remote sensing applications. The general concept behind the GNSS remote sensing is based on investigating the effects of geophysical phenomena that alter the signal characteristics. The remote sensing observations used in this thesis are basically made by investigating the following phenomena:

- the excess path due to the refraction of direct GNSS signals in the troposphere,

- the variation in the strength of reflected GNSS signal due to sea surface roughness, and

- the change of polarization, phase and frequency of GNSS signals in connection to the reflection geometry.

This section describes some of the relevant conceptual foundations for the specified remote sensing applications.

2.5.1   Sea surface characterization using ground-based GNSS-R

A significant portion of the global population inhabits coastal regions where many economic and transportation activities are hosted. These regions have been prone to several natural disasters. In the era of climate change consequences, the necessity of monitoring these regions becomes more vital. Along with previous research on GNSS-R usage for monitoring coastal waters, this thesis contributes to two essential aspects of sea surface characterization, i.e., sea-level monitoring and sea surface roughness estimation. Different factors affecting the performance of GNSS-R coastal altimetry and surface roughness estimation have been investigated. The formulation and the theoretical background used in these assessments are described as follows.

The phase variation due to extra path traveled by the reflected signal, $\psi_{\delta\rho}$, in Equation 2.23 and Equation 2.24 is:

$$\psi_{\delta\rho} = (\frac{2\pi}{\lambda})\delta\rho \tag{2.35}$$

$$= (\frac{2\pi}{\lambda})(\rho_r - \rho_d) \tag{2.36}$$

where λ is the carrier wavelength, ρ_r and ρ_d are the path lengths for the reflected and direct signals, respectively. Figure 2.11(a) shows a simple reflection geometry. In a ground-based setup with low reflector heights, i.e., the height difference between the antenna phase center and the reflecting surface, the GNSS signals

reaching the antenna and the reflecting surface can be approximately considered to be parallel. In this case, the extra path traveled by the reflected signal ($\delta\rho$) can be approximated by the geometric paths as:

$$\delta\rho_g = 2\,\delta H_g \sin e \tag{2.37}$$

where $\delta\rho_g$ is the difference between the geometric paths of the direct and reflected signals, e is the elevation angle of satellite, and δH_g is the reflector height based on assuming the geometric paths shown by dotted lines in Figure 2.19. However, the actual path difference, $\delta\rho_a$, differs from $\delta\rho_g$ due to tropospheric refraction. The refraction induces a bending effect on the signals, which changes the elevation angles at the antenna and reflection points. Moreover, the refraction prolongs the path, leading to an excess phase.
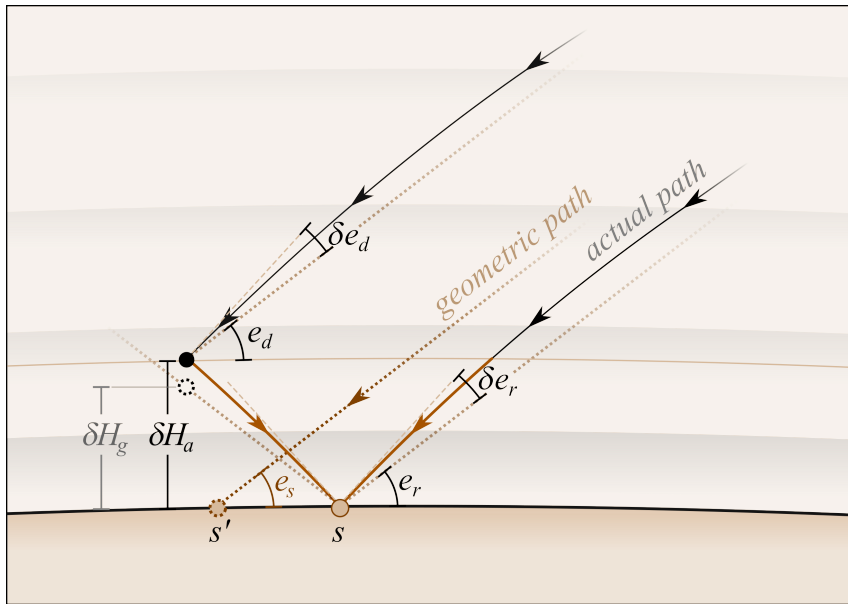
Figure 2.19: The effect of tropospheric refraction on ground-based GNSS-R altimetry.

Different approaches can be used for estimating the tropospheric effect in ground-based GNSS-R altimetry. For instance, Equation 2.37 can be modified to account for the bending of the signals [53]:

$$\delta\rho_a = 2\,\delta H_a \sin(e + \delta e) \tag{2.38}$$

$$\Delta_{tro} = \delta\rho_a - \delta\rho_g$$

$$\approx 2\,\delta H_g \cos e\,\sin\delta e \tag{2.39}$$

with δH_a being the actual reflector height, δe the excess of elevation angle due to the angular effect of the refraction, and Δ_{tro} the tropospheric bending effect on the interferometric path difference. As can be seen from the formula, the tropospheric effect is a function of the reflector height and elevation angle and is always positive. This means geometric approach in calculation of reflector height, i.e., δH_g, underestimates the actual reflector height δH_a (Figure 2.19). The effect is larger for low elevation angles and decreases at higher elevation angles. Moreover, a larger reflector height results in a larger tropospheric effect. The dashed lines in Figure 2.19 show the tangents to the actual rays. The estimated correction provided by Equation 2.39 corresponds to considering the dashed lines (the tangents) instead of the actual rays (solid lines), which can lead to overestimation of the actual reflector height. Moreover, this correction neglects linear refraction along the propagation path [61]. In contrast, another approach presented by [61] only considers the linear refraction and ignores the angular effect (the bending) on the elevation angle. The latter study utilizes Vienna Mapping Function (VMF1) [8] together with the Global Pressure and Temperature (GPT2w) model [9] to estimate total tropospheric delay at the antenna and reflection point using **??**. The difference between the two delays is multiplied by two to yield the total tropospheric correction. According to [61], GPS-derived sea levels show a scale error of 13 mm/m and 15 mm/m respectively for L1 and L2 signals due to the tropospheric refraction. This correction is added to the calculated geometric height, δH_g.

A widely used approach for estimating δH_g is based on the spectral analysis of SNR observations. To this end, the Doppler frequency shift caused by the interference of direct and reflected signals is estimated. This frequency describes the oscillation pattern observed in the SNR observations, otherwise known as the interferometric fringes. The following formulation relates the frequency of interference oscillations to the reflector height:

$$f = \frac{1}{\lambda} \frac{d(\delta \rho)}{dt} \tag{2.40}$$

where f is the interferometric Doppler shift. For simplicity, we introduce and use the variable $x = 2 \sin e / \lambda$ in the calculations. The new interferometric frequency, f_x, can be retrieved by [48]:

$$\delta \rho = \lambda \, \delta H_g \, x$$

$$f_x = \frac{1}{\lambda} \frac{d(\delta \rho)}{dx} = \delta H_g + x \frac{d}{dx}(\delta H_g) = \delta H_g + x \, \delta \dot{H}_g \frac{dt}{dx} \tag{2.41}$$

$$\delta \dot{H}_g = \frac{d(\delta H_g)}{dt} \tag{2.42}$$

where $\delta \dot{H}_g$ is the height rate. The sea level retrieval starts with detecting the predominant interferometric frequency (f_{int}) in a power spectrum produced by any spectral analysis. Let us denote the spectral analysis operator as $\mathscr{L}$, then:

$$P(f_x) \quad = \quad \mathscr{L}(x,Y) \tag{2.43}$$
$$\{P_{max}, f_{int}\} \quad = \quad max[P(f_x)] \tag{2.44}$$

where $P(f_x)$ is the power spectrum retrieved from the spectral analysis, Y is the SNR observation time series after removing the secular trend, and *max* is the function of detecting the maximum value in the spectrum. The frequency corresponding to the detected P_{max}, i.e., the maximum power within the power spectrum, estimates the reflector height:

$$\delta H_g \approx f_{int} \tag{2.45}$$

The approximation sign in the formula is based on the fact that the contribution of the height-rate, i.e., the second term of Equation 2.41, is not considered in the height estimation. Equation 2.45 is based on the assumption of $\delta \dot{H}_g = 0$. To account for the height-rate effect on the interferometric oscillation, the estimated height from Equation 2.45 can be used as an initial value in an iterative solution. An example of this approach is provided in the following.

Performance assessment of sea surface altimetry

Various setups have been used in GNSS-R experiments for altimetry purposes. Most of the experiments use a zenith-looking geodetic antenna and geodetic receiver. This thesis utilizes ground-based GNSS-R observations from a dedicated reflectometry receiver called the Occultation, Reflectometry, and Scatterometry (GORS) receiver [21, 55]. The receiver outputs data streams from multiple antennas at I/Q levels with a 200 Hz sampling rate for GPS L1 and L2 signals. We use these simultaneous observations for the performance assessment of GNSS-R sea level measurements in different scenarios.

Within separate studies [43, 48], we applied two different mathematical method for the spectral analysis (Equation 2.43). The first method, i.e., SSA, was used in the first study for the performance assessment in the presence of sea surface roughness. In the second study, we utilized a multivariate spectral analysis tool for different combinations of the GNSS-R I/Q observations. The method is called Least-Squares Harmonics Estimation (LS-HE) and can be applied to datasets with data gaps or unevenly-spaced time series [48]. Besides the harmonic terms with different periods, LS-HE can include some terms to capture the deterministic trend, e.g., linear trend. LS-HE has a multivariate formulation, which effectively detects common-mode signals in a group of time series. This feature enhances the retrieval of the common interferometric signal in I/Q observations.

The dataset used in the two performance assessment studies is acquired from a receiver with three antennas: one up-looking RHCP antenna as the master link and two sea-looking antennas with RHCP and LHCP designs as the slave links. Based on this setup, four sets of observations are formed in the following scenarios:

- A: The I component of the up-looking RHCP antenna (one time series)

- B: I/Q outputs of the sea-looking RHCP antenna (two time series)

- C: I/Q outputs of the sea-looking LHCP antenna (two time series)

- D: The I/Q components of both sea-looking antennas (four time series)

The observation matrices associated with each scenario include the following columns:

$$
\begin{aligned}
\text{A:} \quad Y &= [I_{m_+}^2] \\
\text{B:} \quad Y &= [I_{s_+}, Q_{s_+}] \\
\text{C:} \quad Y &= [I_{s_-}, Q_{s_-}] \\
\text{D:} \quad Y &= [I_{s_+}, Q_{s_+}, I_{s_-}, Q_{s_-}]
\end{aligned}
\tag{2.46}
$$

with subscripts $+$ and $-$ denoting the RHCP and LHCP, respectively. The subscripts m and s refer to the master and slave channels, respectively. For each scenario, the analysis is independently done on L1 and L2 observations. The observation matrices introduced in Equation 2.46 are separately analyzed by LS-HE method to retrieve the initial estimations of the reflector height. Then, the following cost function is iteratively minimized to reach a more precise estimation of the sea-level by accounting for the height rate [48]:

$$
\min_{\delta H_g, \delta \dot{H}_g} \sum_i^N \| \hat{Y}_i - a_i \sin(\frac{4\pi[\delta H_g + \eta]\sin e}{\lambda} + \phi_i) \|
\tag{2.47}
$$

$$
\eta = \frac{\delta \dot{H}_g \tan e}{\dot{e}}
\tag{2.48}
$$

where η is a correction term to compensate the height rate effect, $\dot{e}$ is the elevation angle rate ($\dot{e} = de/dt$), $\hat{Y}_i$ is the i-th time series in the observation matrix after removing the linear trend, N is the number of observations processed by LS-HE, which is one in scenario A, two in scenarios B and C, and four in scenario D, a_i and ϕ_i are the amplitude and phase offset of the interferometric signal in the i-th observation time series that are estimated by a least-squares analysis.

2.5.2 Sea surface estimation and tidal analysis using LS-HE and SSA

Least squares harmonic estimation (LS-HE)

The LS-HE method is utilized in our study for retrieving sea level variations from the GNSS-R I/Q interferometric observations and for the tidal harmonics analysis. The height retrieval uses multivariate LS-HE formulation while the tidal harmonics detection is based on univariate LS-HE. The multivariate LS-HE, as an extension of univariate harmonics estimation, can detect the common mode signals in a set of multiple time series [4]. In the following a brief introduction to this method is provided. Further details can be found in [5, 4, 45].

Univariate Model

Observation equations can be modeled through the following linear model, which includes deterministic and stochastic parts of the time series [5]:

$$E(y) = Ax \, , \, D(y) = Q_y, \tag{2.49}$$

with $E(\bullet)$ and $D(\bullet)$ indicating the expectation and dispersion operators. Deterministic behavior of the time series is captured by the first term $E(y) = Ax$ and the second term provides a stochastic model to describe the statistical characteristics of the observations. The vector of unknowns includes elements describing a low-order polynomial, e.g., two unknowns for a linear regression model.

Under null hypothesis, we assume that Eq. (2.49) can adequately model the time series. The model can be improved under the alternative hypothesis. For any periodic signal in the time series the deterministic part of the model can be extended by a two-column design matrix A_k:

$$E(y) = Ax + A_k x_k \, , \, D(y) = Q_y, \tag{2.50}$$

where the unknown vector x_k contains two elements to estimate the amplitudes of the signal $a_k \cos(\omega_k t) + b_k \sin(\omega_k t)$ at a frequency of ω_k. The unknown frequencies ω_k are detected through LS-HE, i.e., by maximizing the following functional:

$$\omega_k = arg \max_{\omega_j} P(\omega_j), \tag{2.51}$$

where

$$P(\omega_j) = tr(\hat{e}^T Q_y^{-1} A_j (A_j^T Q_y^{-1} P_A^\perp)^{-1} A_j^T Q_y^{-1} \hat{e}), \tag{2.52}$$

where tr is the trace operator and the least-squares residuals are $\hat{e} = P_A^\perp y$ with $P_A^\perp = I - A(A^T Q^{-1} A)^{-1} A^T Q^{-1}$ being an orthogonal projector. The values of $P(\omega_j)$

construct the power spectrum against a range of different frequencies. The frequency corresponding to the maximum value of the power spectrum indicates the frequency of interest, i.e., ω_K. The statistical significance of the detected frequency can be verified through a hypothesis testing procedure using the test statistic $T_k = P(\omega_j) = tr(\hat{e}^T Q_y^{-1} A_k (A_k^T Q_y^{-1} P_A^\perp)^{-1} A_k^T Q_y^{-1} \hat{e})$. Under the null hypothesis, if the covariance matrix Q_y is known and the distribution of the time series is normal, the test statistic has a central chi-square distribution with 2 degrees of freedom. The detected frequency is statistically significant if the null hypothesis is rejected. The detection process can be repeated for other frequencies with the new design matrix $A = [A \, A_k]$.

Multivariate Model

The LS-HE can be utilized for detecting common periodic signals in multiple time series through a multivariate power spectrum. Each time series can have a dedicated polynomial model with its corresponding unknown coefficients. In this case, if the design matrix A and covariance matrix Q_y are the same for all the time series, the deterministic model can be referred to as multivariate model represented by [5]:

$$E(vec(Y)) = (I_r \otimes A)\, vec(X) + (I_r \otimes A_k) vec(X_k) \tag{2.53}$$

with the multivariate covariance matrix

$$D(vec(Y)) = \Sigma \otimes Q, \tag{2.54}$$

with r being the number of the time series, $\otimes$ the Kronecker product, I the identity matrix, and vec the vector operator. A and A_k are the design matrices.

The second term in Eq. (2.53) includes the element $(I_r \otimes A_k)$ which is is meant to capture a common periodic pattern across all the time series. The common periodicity can have different phase and amplitude in different time series. The matrix Y is the observations matrix, which includes the time series as its columns. The matrices X and X_k are the unknowns. The frequency (ω_k) can be detected through the maximization of the Eq. (2.51) with:

$$P(\omega_j) = tr(\hat{E}^T Q^{-1} A_j (A_j^T Q^{-1} P_A^\perp)^{-1} A_j^T Q^{-1} \hat{E} \hat{\Sigma}^{-1}), \tag{2.55}$$

where $P(\omega_j)$ denotes the multivariate power spectrum, $\hat{E} = P_A^\perp Y$ is the least-squares residuals matrix and $P_A^\perp = I - A(A^T Q^{-1} A)^{-1} A^T Q^{-1}$ is the orthogonal projector and $\hat{\Sigma} = \hat{E}^T Q^{-1} \hat{E}/(m-n)$. The following test statistic can be used for testing the significance of the detected signal:

$$T = P(\omega_k) = tr(\hat{E}^T Q^{-1} A_k (A_k^T Q^{-1} P_A^\perp)^{-1} A_k^T \tag{2.56}$$

If Σ and Q are known and the original observations follow a normal distribution, the test statistic T under the null hypothesis is considered to follow a central chi-square distribution with $2r$ degrees of freedom, i.e., $T \sim \chi^2(2r, 0)$ with r being the number of the time series [5].

Applications of the LS-HE to height retrieval and tidal harmonics detection

The methodology of this study for performance assessment of antenna polarizations and orientations in terms of sea level retrieval contains three main stages (Fig. 2.20). The first stage is the data preparation through which the time series associated with each reflection event are created. In the second stage, we focus on finding the interferometric frequency using multivariate LS-HE in different scenarios. The frequency (L1/L2) and polarization (RHCP/LHCP) of the reflected signals as well as the orientation of the antenna (up-/sea-looking) are variable factors in these scenarios.

Four main scenarios for the estimation of the sea surface heights are designed as follows, each one using L1 and L2 separately: (A) using the I components of the up-looking RHCP antenna (one-time series), (B) using the I/Q components of the sea-looking RHCP antenna (two-time series), (C) using the I/Q components of the sea-looking LHCP antenna (two-time series), (D) using the I/Q components of both sea-looking antennas (four-time series). In addition, the sea surface heights are estimated by combining the retrieved heights from L1 and L2 for each main scenario for possible improvement. Consequently, the sea surface heights are retrieved in 12 different solutions. These products make it possible for us to assess the performance of polarimetric GNSS-R in different antenna angles plus the performance of L1, L2, and a combination of them (L12). The parameter of interest in the LS-HE analysis is the period of the interferometric signals.

The time series of the reflection events are divided into smaller segments by considering a time window. The time window for retrieving this periodic pattern is set to a minimum of 15 min but it is flexibly extended to 30 min until it includes at least two interferometric periods. It is worth mentioning that higher antenna height with respect to the sea surface could have reduced this window size resulting in a better temporal resolution. We move the overlapping window and analyze the segment with a time step of 1-min to cover the whole time series. The sea surface height is estimated from each segment.

To combine the estimated heights from different satellites we use an averaging window. For outlier detection, we use a native MATLAB function that utilizes the median absolute deviation (MAD) values. All the values beyond three scaled MAD with respect to the median are considered outliers. After outlier elimination, the

Data Set
- (A) Up looking samples
- (B) Sea looking I/Q samples (RHCP)
- (C) Sea looking I/Q samples (LHCP)
- (D) Sea looking I/Q samples (RHCP & LHCP)

Process
- Making time series for each reflection event
- Estimating interferometric period for each 15-min segment using LSHE
- Sea surface height estimation
- Averaging of the calculated heights from the different satellites for different time window

Products
- (A) h_{L1}, h_{L2}, h_{L12}
- (B) h_{L1}, h_{L2}, h_{L12}
- (C) h_{L1}, h_{L2}, h_{L12}
- (D) h_{L1}, h_{L2}, h_{L12}
- Evaluation of the result with respect to the tide gauge and wind speed

Figure 2.20: Methodology flowchart based on the Least Squares Harmonic Estimation (LS-HE).

median value of the estimates within the averaging window is considered the final height estimate. The final estimates are calculated every 5 minutes with different averaging windows ranging from 15 minutes to 6 hours (6 hours, 3 hours, 1 hour, and 15 minutes). The last stage of the methodology is the validation of the GNSS-R height estimates with the collocated tide gauge observations at different wind speeds.

We first apply multivariate LS-HE for SL calculation. The multivariate formulation provides a robust tool to find the common-mode interferometric period in the I/Q time series obtained from the GNSS-R receiver. The SL time series from GNSS-R and the nearby tide gauge are then analyzed by the univariate LS-HE to characterize the tidal harmonics.

The LS-HE method performs a numerical search to catch the dominant harmonic signals in the time series. The step size for finding the harmonic signals is determ-

ined with the following recursive formula:

$$T_i = T_{i-1}\left(1 + \alpha \, \frac{T_{i-1}}{T_{max}}\right), \; \alpha = 0.01 \, , \; i = 1, 2, ..., T_i \leq T_{max}, \qquad (2.57)$$

with T_i being the trial periods, T_0 and T_{max} the minimum and maximum periods in the time series based on Nyquist's theorem, respectively. The coefficient α controls the resolution or step of searching the periods. The recursive formula creates smaller step sizes for shorter periods and larger step sizes for longer periods. We assume the covariance matrix is the Identity matrix $Q_y = I$ for each time series. The observation matrices used in the SL retrieval and in the tidal harmonics analysis are as follows:

Observations matrix for finding interference pattern: $\quad Y = [I, Q]$

Observations matrix for tidal harmonic : $\quad Y = [h_{GNSS}], Y = [h_{TG}] \quad (2.58)$

It should be noted that the univariate formulation of LS-HE with $Q_y = I$ will act similarly to the ordinary least squares method.

Fig. 2.21 shows an example of sea level estimation using LS-HE.

Phase and amplitude estimation

We use the U-tide MATLAB package [15], implemented according to the equilibrium tide theory [16] for deriving the amplitude and phase of a standard table of tidal constituents from the GNSS-R and tide gauge SL measurements. The following model is used for the estimation of the amplitude and phase of the tidal constituents (equation (6) in [17]):

$$h(t_j) = Z_0 + a\,t_j + \sum_{k=1}^{n} f_k(t_j) \, [X_k \, \cos\left(V_k(t_j) + u_k(t_j)\right) +$$

$$Y_k \, \sin\left(V_k(t_j) + u_k(t_j)\right)] + R(t_j) \quad (2.59)$$

where X_k and Y_k are:

$$X_k \;\; = \;\; A_k \, \cos g_k \,, \qquad\qquad (2.60)$$
$$Y_k \;\; = \;\; A_k \, \sin g_k \qquad\qquad (2.61)$$

with $h(t_j)$ being the SL measurement at the time t_j; Z_0 and a are the unknown linear terms, and for each constituent k the unknown amplitude and phase are respectively denoted by A_k and g_k. In the process of tidal harmonic analysis, the unknown
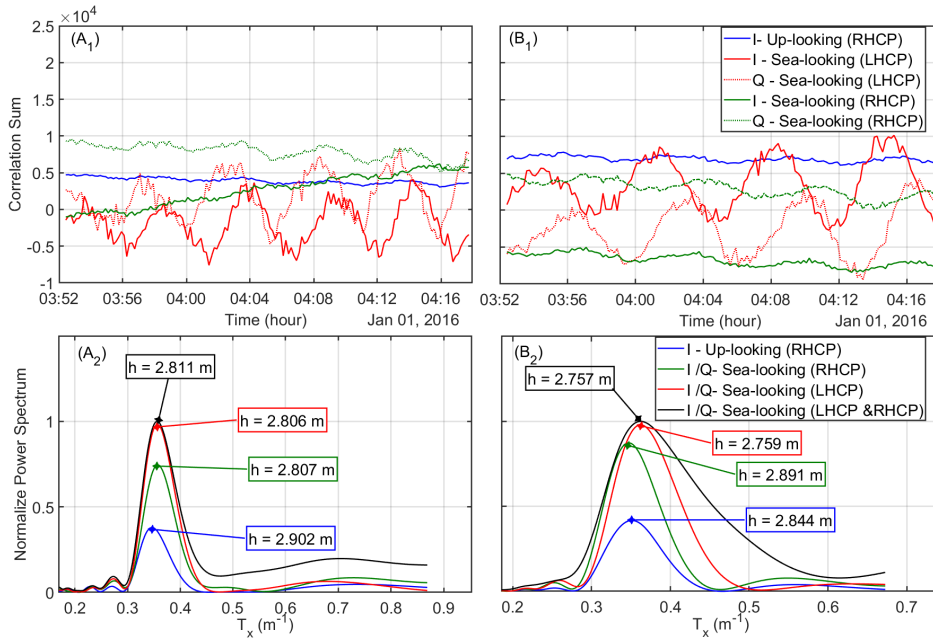
Figure 2.21: Examples of observation time series of PRN 26 for one segment which are used to retrieve interferometric period (T_{int}) using multivariate LS-HE formulation. (A_1) and (B_1) show the In-phase and Quadrature components for GPS L1 and L2, respectively. (A_2) and (B_2) illustrate the dominant interferometric period retrieved by LS-HE based on different combinations of the time series.

parameters are estimated by minimization of the residuals $R(t_j)$, while the nodal corrections [19] to the amplitude ($f_k(t_j)$) and phase ($u_k(t_j)$), and the astronomical argument $V_k(t_j)$ [19] can be calculated for each constituent k at the time of sea level measurement t_j [17].

Singular spectrum analysis for sea level estimation

SSA is a time series analysis tool with a wide range of applications such as extracting time series trend, noise mitigation, forecasting, and change-point detection [3]. Here, applying SSA to the I/Q time series to extract the interferometric fringes. The first step in SSA is to construct a trajectory matrix. The matrix is formed using the elements of the time series. In the following steps, the matrix is decomposed into its principal components and is reconstructed back using the most important principal components of the matrix. Finally, SSA rebuilds the time series using the reconstructed trajectory matrix. These steps are elaborated in the following:

A) Forming the trajectory matrix: By moving a window with the length of L over the entries of the time series (f_i), the trajectory matrix $(\mathbf{X})$ is constructed:

$$\overbrace{f_1, f_2, ..., f_L}^{window\rightarrow}, f_{L+1}, f_{L+2}, ..., f_N$$

$$\mathbf{X} = (x_{ij})_{i,j=1}^{L,K} = \begin{bmatrix} f_1 & f_2 & f_3 & \cdots & f_K \\ f_2 & f_3 & f_4 & \cdots & f_{K+1} \\ f_3 & f_4 & f_5 & \cdots & f_{K+2} \\ \vdots & \vdots & \vdots & \ddots & \vdots \\ f_L & f_{L+1} & f_{L+2} & \cdots & f_N \end{bmatrix} \tag{2.62}$$

with $K = N - L + 1$ and $1 < L < K$.

B) Decomposition of the trajectory matrix: Singular Value Decomposition (SVD)[60] of $\mathbf{X}$ can be written as:

$$\mathbf{X} = \mathbf{U}\Sigma\mathbf{V}^{\mathbf{T}} \tag{2.63}$$

with the superscript ^{T} being the transpose operator. $\mathbf{U}$ and $\mathbf{V}$ contain left and right singular vectors, respectively, and Σ is a diagonal matrix containing the singular values (σ_i) of $\mathbf{X}$. Now, the trajectory matrix can be expressed as the sum of its uncorrelated components $(\mathbf{X_i})$:

$$\mathbf{X} = \mathbf{X_1} + \mathbf{X_2} + ... + \mathbf{X_d}, \quad \mathbf{X_i} = \sigma_i \mathbf{U_i} \mathbf{V_i^T} \tag{2.64}$$

where d is the index of the smallest non-zero singular value.

C) Grouping components of the trajectory matrix: In the grouping step a group or subset of $\{\mathbf{X_1}, \mathbf{X_2}, ..., \mathbf{X_d}\}$ is selected in order to create a representative estimation of the original trajectory matrix $(\mathbf{X})$. The selected subset defines the smoothness of the final reconstructed time series. If the time series is not dominated by noise, the first few singular values can generally reflect a significant part of the total information within the time series. Details about the specific grouping approach chosen in our homogenization method can be found in [24].

D) Reconstruction of the time series: The selected group of trajectory matrix components, denoted by $\{\mathbf{X_1}, \mathbf{X_2}, ..., \mathbf{X_I}\}$, are added to reconstruct a matrix associated with the time series trend.

$$\mathbf{X_{trend}} = \mathbf{X_1} + \mathbf{X_2} + ... + \mathbf{X_I} = (\hat{x}_{ij})_{i,j=1}^{L,K} \tag{2.65}$$

Now, we retrieve the time series trend using the anti-diagonal elements of the trend matrix ($\mathbf{X_{trend}}$). Let $L < K$, then the trend of the time series $G = (g_1, g_2, ..., g_N)$ is:

$$
g_i = \begin{cases}
\frac{1}{i} \sum\limits_{m=1}^{i} \hat{x}_{m,i-m+1} & 1 \leq i < L \\
\frac{1}{L} \sum\limits_{m=1}^{L} \hat{x}_{m,i-m+1} & L \leq i \leq K \\
\frac{1}{N-i+1} \sum\limits_{m=i-K+1}^{N-K+1} \hat{x}_{m,i-m+1} & K \leq i \leq N
\end{cases}
\tag{2.66}
$$

where $\hat{x}_{i,j}$ is an entry of the reconstructed trajectory matrix, which estimates the original element of the time series f_{i+j-1}. Therefore, the SSA-estimation of the element f_k can be calculated by averaging all $\hat{x}_{i,j}$ satisfying: $k = i + j - 1$.
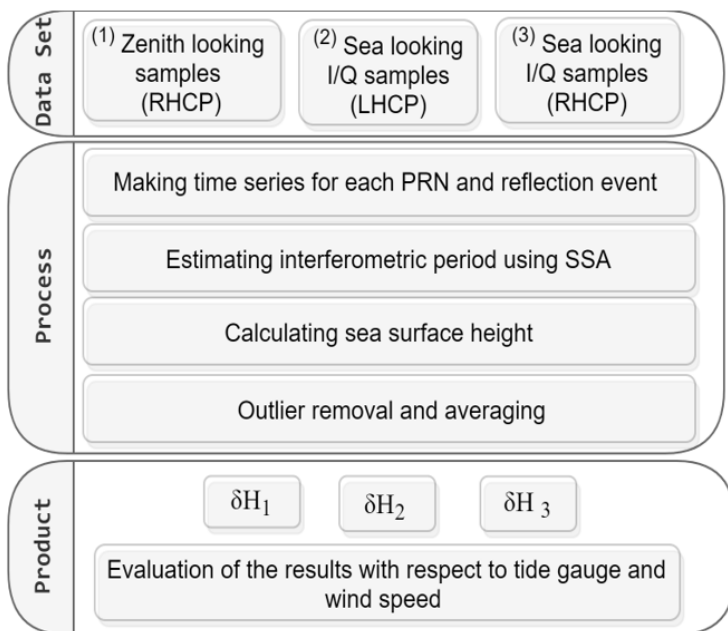
Figure 2.22: 1 Methodology flowchart based on the Singular Spectrum Analysis (SSA).

Briefly, the methodology contains three main steps illustrated in Fig. 2.22. The first step includes the data preparation described by [49]. The second or key step focuses on applying SSA to the time series of each PRN over reflection events. The retrieved interferometric signal is then inverted to the sea level estimate. We finish this step by outlier removal and finding the median of the sea surface height in the step of 5 min with a temporal window of 3 hours. In the final step, we evaluate the estimated sea surface heights with respect to the tide gauge observations and

different wind speeds. Fig. 2.23 shows an example of applying SSA to the I/Q time series to extract the interferometric fringes. The method can simultaneously mitigate other irrelevant components. As seen in the figure, the applied method can effectively reveal the amplitude variations of the interferometric signal. The detected peaks in the bottom panel of Fig. 2.22 are used to estimate the period of interest for the calculation of height

2.5.3 Flood detection and mapping using space-borne GNSS reflectometry

Natural disasters are the reason for many serious disturbances to communities and the environment. There have been many human, environmental, social, and economic losses, which are beyond the power of the community to tolerate [59]. Floods have been considered as one of the most catastrophic events, causing extensive damage to the artificial and natural environment and devastation to human settlements [52]. Economic losses due to the effects of damaging floods have increased significantly around the world [2]. Flooding happens when water bodies overflow riversides, lakes, dams, or dikes in low-lying lands during heavy rainfall [1]. The higher temperature at the Earth's surface leads to increased evaporation and greater overall precipitation [39]. Increased precipitation, although associated with inland flooding, can also increase the risk of coastal flooding [27].

Flood detection, and subsequently, produced maps, are beneficial in two important phases: During the flood, when we need emergency management planning, and after the flood, for land use planning, defining construction standards, and damage assessment [10]. Heavy precipitation has led floods to occur more frequently in different countries, which have drawn considerable attention over the past years. There are many regions of Iran affected by floods, for instance, heavy rainfall from mid-March to April 2019 led to flooding in 28 of 31 provinces, with the most severe flooding occurring in Golestan, Fars, Khuzestan, and Lorestan. The recent torrential rain in mid-January 2020 in the southeastern region of Iran caused a devastating flood in the Sistan and Baluchestan province. We investigated the latter case in this study.

Land surveying and airborne observations are the traditional methods for flood detection, but when flood detection is conducted on a large scale, these methods are costly and slow. Space-based Remote Sensing (RS) can be considered as a practical alternative that provides up-to-date information from various sensors that have been onboard different satellites. However, there are some limitations in using RS data products for the study of flooding. For instance, optical RS can have its limitations during severe weather conditions and during the night. Therefore, in some cases before and after a flood event, the optical RS imagery does not provide

the required information [10]. Radar RS in the microwave spectrum can surpass these restrictions because the wave can penetrate clouds and vegetation and can effectively work at night. Among the several radars RS sensors currently in operation, Synthetic Aperture Radar (SAR) imagery provides high spatial resolution data which is typically based on a monostatic configuration. However, the revisit time of satellites with the configuration of the monostatic radar (single satellites), like SAR, is long (more than one week) and cannot offer the desirable continuous high temporal resolution for flood detection purposes. Accordingly, owing to the highly dynamic nature of the flood, SAR images are not used operationally during floods [41, 29, 13, 46].

Global Navigation Satellite System Reflectometry (GNSS-R) is an innovative technique aimed at deriving geophysical parameters by analyzing GNSS signals reflected off the Earth's surface in a bistatic geometry. This technique is an efficient microwave remote sensing approach that utilizes transmitted navigation signals as sources of opportunity. Numerous GNSS satellites, including GPS, Galileo, GLONASS, and Bei-Dou/Compass, are currently transmitting navigation signals based on spread-spectrum technology. Thus, a constellation of GNSS-R small satellites, at a lower cost compared to ordinary RS satellites, can provide a much shorter revisit time using low-cost, low-power passive sensors. Many earlier studies have introduced the applications of GNSS-R on the oceans, land, and ice [63].

The soil moisture, surface roughness, vegetation, and topography are parameters which affect microwave signals. GNSS-R signals as a bistatic radar are also affected by those parameters [20]. However, GNSS signals are at the L-band, which is ideal for soil moisture and surface water remote sensing due to the higher capacity to penetrate vegetation compared to shorter wavelengths [12]. In addition, this technique uses the bistatic configuration, which has a lower sensitivity to surface roughness relative to monostatic [37]. The signals reflected off the surface have a direct relation with surface water and moisture content [13]. For example, the rise of soil moisture leads to an increase the signal strength. Using this mechanism could contribute to detecting soil saturation, flooded area, and inland water.

The Cyclone Global Navigation Satellite System (CYGNSS) mission is a constellation of eight microsatellites, each with a GNSS-R receiver onboard. The receiver can track and process four GPS signals simultaneously. The tracked GPS L1 C/A signals after reflection from the Earth's surface are used to produce Delay Doppler Maps (DDMs). The overall median revisit time is 2.8 h, and the mean revisit time is 7.2 h [51]. Theoretically, the footprint of reflection received by CYGNSS is nearly 0.5 km × 0.5 km. For the ocean, which has a very rough surface, the spatial resolution is approximately 25 km × 25 km [50]. Table 1 shows CYGNSS microsatellite parameters retrieved from [12]. The main mission of CYGNSS is

to measure the ocean surface wind speed in hurricanes and tropical cyclones, so a relatively low orbital inclination was designed for the satellites. CYGNSS continuously makes measurements over the oceans and provides useful information over the land [29]. CYGNSS offers distinct features compared to other remote sensing techniques such as optical and active monostatic radar. It uses a passive sensor at the L-band frequency wave, which works in all weather conditions regardless of the time of the day, i.e., it can penetrate clouds, fog, rain, storms, and vegetation, and works at night, unlike optical sensors. The CYGNSS constellation of eight microsatellites provides a relatively short revisit time with global coverage over equatorial regions. The products of CYGNSS are publicly available over the oceans and land.

In recent years, the frequency of heavy precipitation and consequently flooding has significantly increased in many regions all over the world. Figure 2.24 shows a global prediction for the return period of flooding for the 21st century [22]. Detection and mapping of flooding events are of particular importance for two phases, i.e., during flood for emergency management, and after flood, for the assessments of damages and destruction, land use planning, as well as re-construction standards [46]. Therefore, providing accurate and timely information about the extent of floods and destruction is crucial.

Spaceborne GNSS-R as an emerging remote sensing technique has the potential to be used for flood detection and mapping. This technique has specific features that can provide a robust solution for flooding applications. The L-band frequency used for the satellite navigation systems creates a measuring tool, which is almost insensitive to severe weather conditions or heavy precipitation. The instrumentation used for the GNSS-R sensors is relatively low-cost and low-power. This makes the GNSS-R sensors to be a suitable choice for small satellite technology. Therefore, an inexpensive constellation of small satellites with GNSS-R payloads can make a spaceborne global Earth monitoring system with high temporal resolution. Since 2017, the NASA CYGNSS mission has provided spaceborne GNSS-R observations over tropical regions. The coverage of this mission is marked in Figure 2.24 by gray lines. With the constellation of eight satellites, the mission delivers an average revisit time of about seven hours. This thesis includes the application of the CYGNSS dataset to flood detection and mapping during torrential rain in 2020 in the southeastern part of Iran, mainly over Sistan and Baluchestan province [46].

The peak power of each DDM generated by the GNSS-R receiver, includes several non-geophysical factors which should be accounted for. The following equation relates the factors to the coherent component of the power for the received GNSS

reflected signals [13]:

$$P^R = \frac{P^T G^T}{4\pi(R^T + R^R)^2} \frac{G^R \lambda^2}{4\pi} \Gamma \tag{2.67}$$

where P^T is the transmitted RHCP power, G^T is the gain of the transmitter antenna, R^T and R^R are the lengths of the transmitter to reflection point and reflection point to receiver paths, respectively, G^R is the gain of the receiver antenna, λ is the GPS wavelength ($\approx$0.19 m), and Γ is the Surface Reflectivity (SR).

For the simplicity of calculation, we can work in decibel (dB) scale. For conversion to dB scale, e.g., for a power value of P, the following formula can be used:

$$P_{dB} = 10\log_{10}(P) \tag{2.68}$$

Then, the surface reflectivity in dB scale can be calculated by [13]:

$$\Gamma_{dB} = P_{dB}^R - P_{dB}^T - G_{dB}^T - G_{dB}^R - 20\log\lambda + 20\log(R^T + R^R) + 20\log(4\pi) \tag{2.69}$$

There are the following variables in the CYGNSS Level-1 (L1) data that can be used for the calculation of SR:

- **ddm_snr** is the SNR value in dB scale, which is the ratio of DDM peak power to the noise floor. SNR value is proportional to P_{dB}^R.

- **gps_tx_power_db_w** (P_{dB}^T)

- **gps_ant_gain_db_i** (G_{dB}^T)

- **sp_rx_gain** (G_{dB}^R)

- **tx_to_sp_range** (R^T)

- **rx_to_sp_range** (R^R)

By retrieving the above-mentioned variables from the CYGNSS L1 data, we can calculate a value that in magnitude is not equal to SR but it is directly proportional to Γ [13]:

$$\Gamma_{dB} \propto SNR_{dB} - P_{dB}^T - G_{dB}^T - G_{dB}^R - 20\log\lambda + 20\log(R^T + R^R) + 20\log(4\pi) \tag{2.70}$$

Detection of flooded areas is done by applying a certain threshold to the calculated Γ values. This means the SR-proportional values (right side of Equation 4.1) above a specific limit are considered to be associated with inundated or partially

inundated areas [13, 46]. This approach stems from the fact that the presence of water significantly changes the permittivity of the reflecting surface. The difference in reflection power losses due to different permittivities of dry soil and water are depicted in Figure 2.15, right panel.

Several issues can affect the accuracy of flood detection using GNSS-R measurements. The transmitting power of GPS satellites (P^T) can be different for different GPS blocks and can also decay due to aging. Inaccurate information about the transmitter antenna gain or the attitude of the satellite can be another error source. The issue of attitude determination is also valid for the receiver satellite. The attitude determination errors can be translated to incorrect gain value for the receiving antenna and misinterpreted as a geophysical effect. Another issue is related to the combined effect of incidence angle and topography of the reflecting surface. We apply a data preparation procedure to reduce some of the impacts of the mentioned issues. The key items of the data preparation procedure are as follows:

- *Calibration of transmitting power biases:* GPS satellites in different blocks or with different ages might have different transmission powers. This variation introduces some biases compared to the approximated values of the transmitter power and should be taken into account during the analysis. Different GPS PseudoRandom Noise (PRN) codes also contribute to the biases [46]. To address this issue, we calibrate the SNR values of different GPS satellites (SNR_{dB}) using empirically estimated biases, which can be found in [46].

- *Filtering high incidence angles:* high incidence angles can influence the coherent reflection from the surface. Therefore, we have removed all the observations with incidence angles above 65 degrees in our study [46].

- *Removing poor quality observations:* each observation made by CYGNSS satellites is accompanied with a quality control flag, which is a number indicating possible issues related to that specific observation. We eliminate all the observations with quality flags indicating the following issues: S-band transmitter powered up, spacecraft attitude error, black body DDM, DDM is a test pattern, the direct signal in DDM, and low confidence in the GPS Equivalent Isotropically Radiated Power (EIRP) estimate [46].

- *Additional filtering:* the CYGNSS observations with SNR_{dB} below 2 dB or with receiving antenna gains beyond the range of 0 to 13 dB are removed from the analysis after [12].

As a summary Fig 2.25 shows the methodology for flood detection using space-born GNSS-R in our study which includes five main steps. The steps are (1) Data collection, (2) data preparation, (3) calculating the surface reflectivity, (4) data calibration, and (5) flood detection and validation.
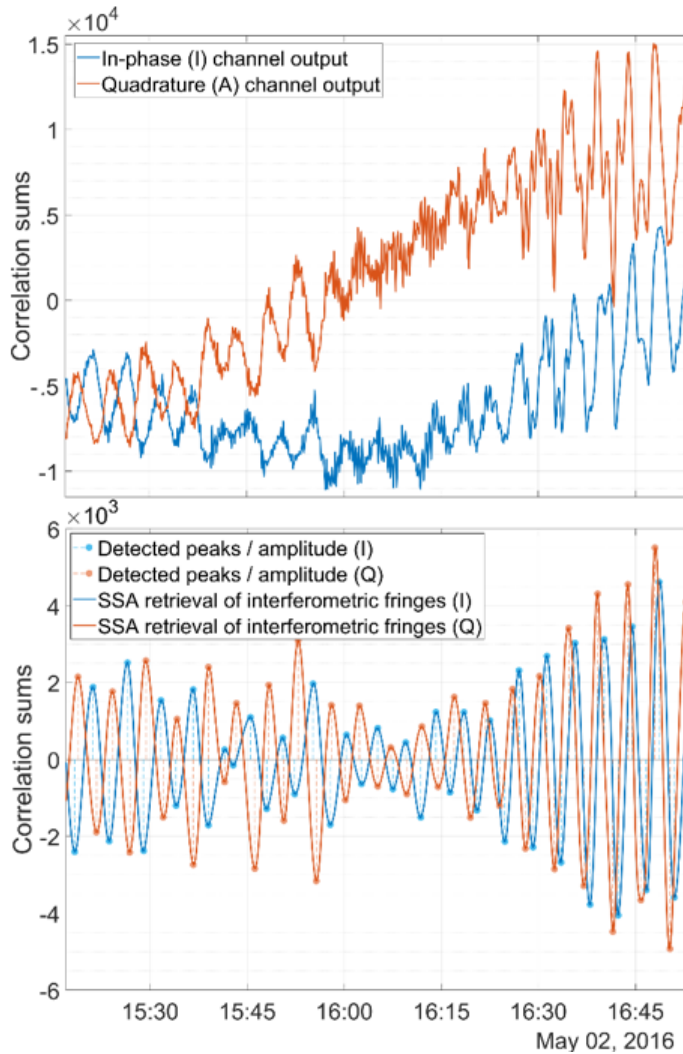
Figure 2.23: Top panel: an example of the in-phase / quadrature (I/Q) time series from GPS PRN 12 on May 02, 2016. Bottom panel: the result of retrieving interferometric fringes from the I/Q correlation sums using Singular Spectrum Analysis (SSA). The dark and light blue separate the in-phase and quadrature samples, respectively. The dots in the bottom panel show the detected peaks after applying SSA. The dashed lines illustrate the estimated amplitude.
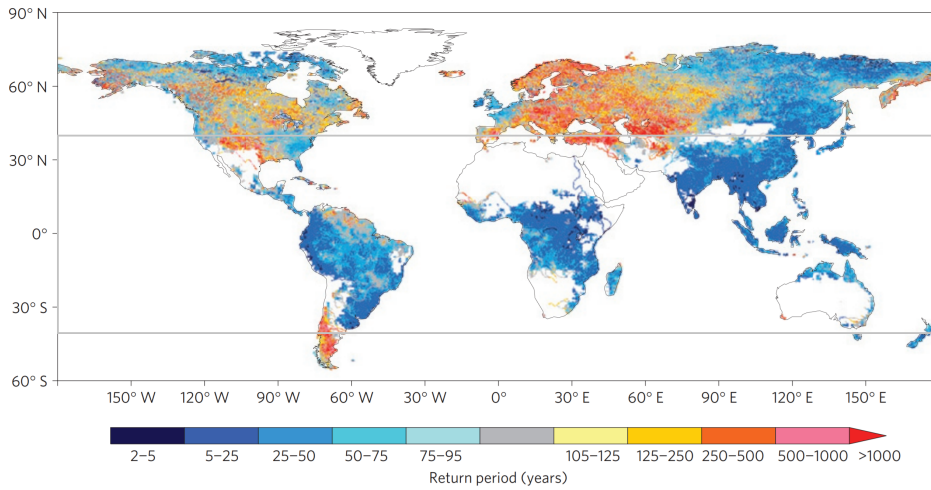
Figure 2.24: Global prediction map of flooding return period for 21st century. The gray lines show the coverage limits of the CYGNSS GNSS-R mission (image source: [22]).
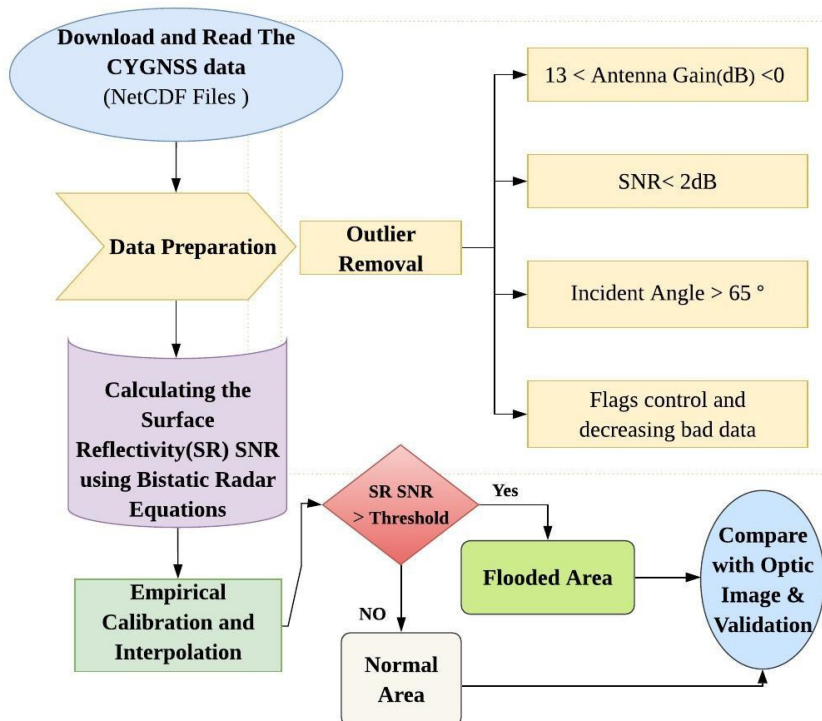
Figure 2.25: Methodology flowchart based on the bistatic radar concept and using CYGNSS data [46].

Chapter 3

Results

In this chapter, the key outcomes of this dissertation are succinctly outlined. Furthermore, the interrelations between the papers in this dissertation and the research questions articulated in Section 1.3 are elucidated.

3.1 Overview

The primary objective of this thesis is to enhance the quality of GNSS data products and explore innovative applications of GNSS remote sensing measurements in climate and environmental monitoring. In pursuit of this objective, a series of research papers have been presented, each addressing specific research inquiries.:

In *Paper A* the spaceborn observations of surface reflectivity are used to detect and map a flooding event during torrential rain. The observations have a revisit time of about 7 hours, making the technique a suitable candidate for natural hazard monitoring purposes. The results of this study confirm the successful detection of inundated areas ($\rightarrow$RQ 1.3 and $\rightarrow$RQ 1.4). Based on the results achieved from the studies mentioned above, a GNSS-R CubeSat concept is proposed to perform high-resolution observations over selected regions ($\rightarrow$RQ 1.2) and we could understand how we can use the spaceborn GNSS-R data for environment monitoring ($\rightarrow$RQ 1.1). A description of the proposed CubeSat concept is included in Chapter 4.

Paper B. This paper investigates the possible effects of sea surface roughness on sea-level measurements. The results confirm that the surface roughness, or sea state, has a degrading impact on the sea surface height estimation ($\rightarrow$RQ 2.1, 2.2, and 2.3).

Paper C describes the roles of polarization and orientation of the antenna as well as using signals with different wavelengths for sea level measurements. This study elucidates which configuration can improve the performance of GNSS-R sea-level measurements (→RQ 2.1). Based on these studies, a favorable setup for a coastal GNSS-R station is suggested to use a tilted antenna towards the reflection zone to assign the maximal gain to the reflected signals (→RQ 2.2). Using two antennas with different polarization and combining the results can enhance the quality of measurements (→RQ 2.2). The multi-frequency feature should be considered for a GNSS-R station since it significantly increases the number of observations leading to more robust sea surface characterization (→RQ 2.2). Also, we can see the mathematical signature in the results (→RQ 2.3)

Paper D shows the tidal harmonics retrieval results using GNSS-R. The paper results indicated very good agreements between GNSS and TG retrieved results and we can see the better functionality of GNSS-R in the lower periods (→RQ 2.1, 2.2 and 2.3)

3.2 Papers of the dissertation

This section provides a short description of the content, methodology, results, and contribution of the authors in each paper of this dissertation.

3.2.1 Paper A: Evaluation of CYGNSS Observations for Flood Detection and Mapping during Sistan and Baluchestan Torrential Rain in 2020

Content

This paper evaluates a remote sensing application of spaceborne GNSS-R observations for the detection of a flooding event and mapping the affected areas. The main dataset used for the evaluation is obtained from the level-1 data product of NASA CYGNSS mission during a heavy rain in January 2020 over south-eastern part of Iran. The selected study area faces a high risk of flood, proven by similar events during recent years and needs continuous monitoring. The forward-scattered GNSS signals are exploited to calculate the surface reflectivity using the bistatic radar equation. The flooded areas are detected based on the analysis of the derived reflectivity. For the verification purpose, the study uses Moderate-Resolution Imaging Spectroradiometer (MODIS) images.

Research Method

The main parameter of interest used in the analysis was the delay doppler map SNR, which was retrieved from the level-1 data product of NASA CYGNSS mis-

sion. First, a data preparation procedure was applied to remove outliers and discard low-quality data. In the next step, inverse bistatic radar formula was used to calculate the corrected SNR, which was closely related to surface reflectivity and hydrological conditions. The corrected SNR values were calibrated and interpolated to a regular grid over the study area. After calibration and gridding, the corrected SNR was verified with the MODIS optical image. A threshold of about 11 dB or more could be distinguished between the inundated and noninundated areas in the regions of interest. Finally, the flood-affected areas were mapped on Google Maps. The area of the flooded regions was estimated to be about 19,644 km^2 or 10.8% of the province.

Results

This study demonstrated the potential of timely spaceborne GNSS-R observations over land for detecting and mapping floods. The investigation specifically focuses on a flood occurred in Sistan and Baluchestan province of Iran where a heavy rain in mid-January 2020 caused a destructive flood. The analysis estimates the inundated area to be about 19,644 km^2 (Figure 3.1). Many cities, roads, and other infrastructures were affected by the flood in these regions. The results indicate the regions close to depression, lakes, and coastal areas are at a high risk of flooding in this province (Figure 3.2). This study confirms that CYGNSS data is of value for hydrological investigations, particularly flood detection in the Sistan and Baluchestan province. Despite a relatively short revisit time of CYGNSS observations, the spatial resolution of the data products needs to be improved for mapping purposes. This issue could be addressed in future missions by, e.g., increasing the number of onboard processing channels, as well as by processing the reflected signals from other GNSS constellations such as GLONASS, Galileo, and BeiDou.

Authors Contributions

Conceptualization, H.N., M.R.; Data curation, M.R., M.H.; Formal analysis, M.R.; Funding acquisition, M.R. and H.N.; Investigation, M.R. and M.H.; Methodology, M.R.; Software, M.R. and M.H.; Supervision, H.N.; Validation, M.R.; Visualization, M.R.; Writing—original draft, M.R.; Writing—review and editing, H.N. and M.H. All authors have read and agreed to the published version of the manuscript.

3.2.2   Paper B: A Performance Assessment of Polarimetric GNSS-R Sea Level Monitoring in the Presence of Sea Surface Roughness

Content

This paper appraises the performance of sea level measurements derived from ground-based GNSS-Reflectometry observations during different sea states. The
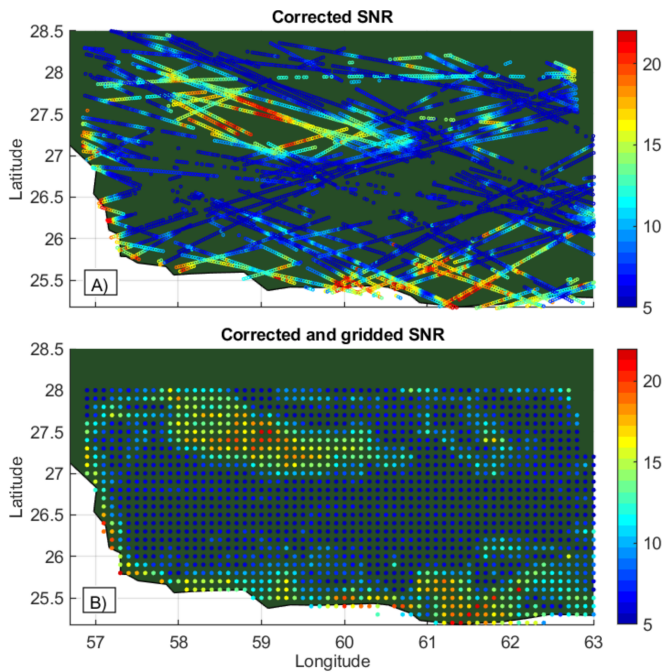
Figure 3.1: The outcome of interpolation process for the corrected SNR over the period of three days from 13 January to 15 January 2020. (A) Representation of the CYGNSS measurements along the satellite tracks, (B) the interpolated data at $0.1° \times 0.1°$ grid points using the natural neighbor interpolation method (reused from [46]).
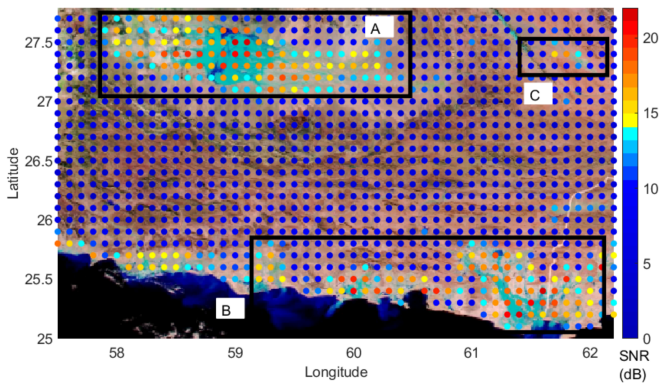
Figure 3.2: The georeferenced optical satellite imagery of the flood from MODIS (13 January 2020) overlaid by the corrected signal to noise ratio derived from CYGNSS observations (13 January to 15 January 2020). The regions labeled A, B, and C show significant SNR anomalies (reused from [46]).

GNSS-R observations which are used to retrieve sea surface height are obtained from a dedicated GNSS-R receiver with three links. The master links uses an up-looking RHCP antenna and two slave links use RHCP and LHCP antennas. The tilted seaward antennas are meant to capture the sea reflections with the highest gain value while the up-looking antenna is simulating the antenna orientation in an ordinary geodetic GNSS station. To analyze the effect of wind, the GNSS-R dataset is collocated with wind measurements from a nearby meteorological station. The study validates the GNSS-R derived sea surface heights against the tide gauge measurements which is about 300 meters away. The Root Mean Squared Error (RMSE) and bias of the measured sea level with respect to the tide gauge is then evaluated based on different wind speed ranges.

Research Method

The ground-based sea level measurements is based on the analysis of interferometric fringes which are results of the interference of direct and reflected GNSS signals. To extract these fringes, the study utilizes SSA technique. This technique can effectively separate different components of the GNSS-R observations and provide a clean retrieval of interferometric pattern. The periods of these patterns are then calculated using a peak detection algorithm. The periods is accompanied with satellite orbit information to estimate the sea level at each epoch. The epochs are classified based on sea states using the wind speed information. The GNSS-R derived sea level anomalies are compared to tide gauge measurements for evaluating the results at different sea states.

Results

This study suggests that the height estimates from the sea-looking LHCP antenna provide higher level of accuracy compared to both up- and sea-looking RHCP antennas. The RMSE of GNSS-R water levels compared to the nearest tide gauge measurements are 2.8 and 3.9 cm for the sea-looking LHCP and RHCP antennas, respectively, and 4.7 cm for the zenith-looking RHCP antenna. The corresponding correlation coefficients of the measurements pairs are 97.63, 95.02, 95.35 percent, respectively. The paper reports on a degrading impact of sea surface roughness on all types of the GNSS-R observations. The impact is prominent both in the bias and RMSE of the measurements with respect to the tide gauge data (Figure 3.3).

It is noteworthy that the estimated biases in this experiment could be different from other similar setups. This stems from the fact that the wind effect on coastal regions depends on the location of the station and wind direction. Therefore, different
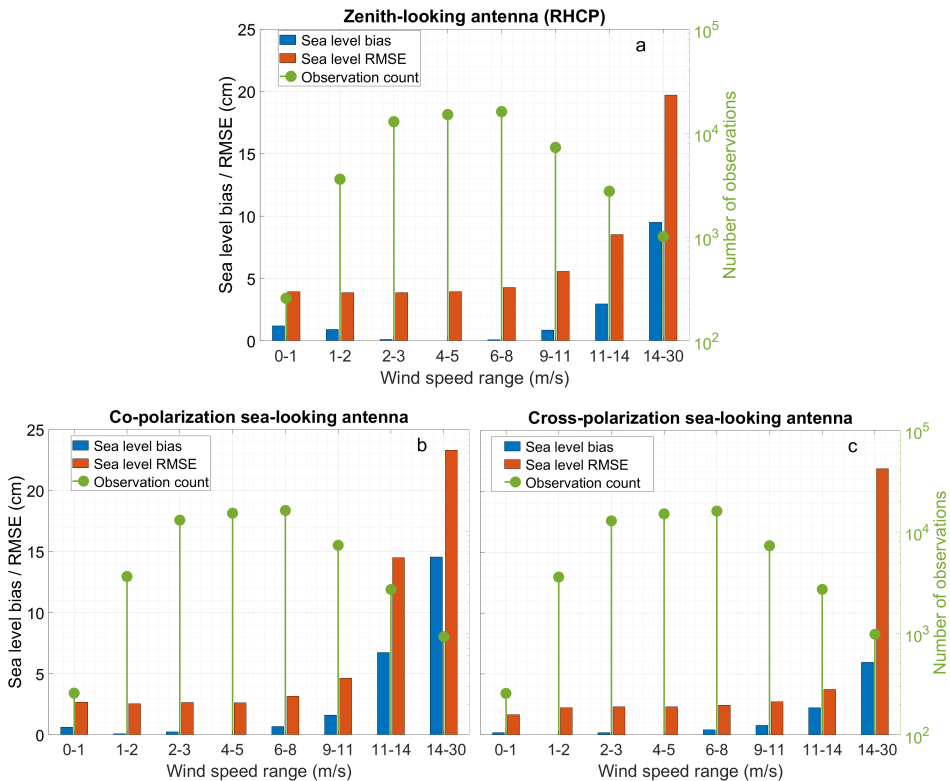
Figure 3.3: An evaluation of the performance of GNSS-R sea level measurements at different sea state based on the observations from RHCP and LHCP antennas with zenith-looking and sea-looking orientations. The panels show the results from the zenith-looking RHCP (a), sea-looking RHCP (b), and sea-looking LHCP (c) antennas. The blue bars show the bias of the GNSS-R measurements with respect to the tide gauge over each wind speed range. The red bars are the associated RMSE values (reused from [44]).

directions of wind can induce different impact on a coastal GNSS-R experiment.

Authors Contributions

Conceptualization, M.R. and M.H.; GNSS-R experiment and data, M.Ram., J.W.; Match-up wind data: R.H.; Data curation, M.R. and M.H.; Formal analysis, M.R., M.H., M.S.; Funding acquisition, M.R. and H.N.; Investigation, M.R. and M.H.; Methodology, M.R. and M.H.; Software, M.R., M.H. and M.S.; Supervision, H.N. and J.W.; Validation, M.R., M.H.; Visualization, M.R., M.H.; Writing—original draft, M.R., M.H.; Writing—review and editing, M.H., H.N., M.S., R.H. and J.W. All authors have read and agreed to the published version of the manuscript.

3.2.3 Paper C: Polarimetric GNSS-R Sea Level Monitoring using I/Q Interference Patterns at Different Antenna Configurations and Carrier Frequencies

Content

In this paper, the performance of GNSS-R monitoring of sea surface height based on different scenarios is evaluated. The flexible setup used in the GNSS-R experiment allows a multi-parameter evaluation in terms of frequency of the signals, polarization and orientation of the antennas, as well as the impact of temporal averaging. The quality of final sea level products based on each satellite Pseudorandom Noise (PRN) is determined for either of L1 and L2 GPS frequencies. The study also includes quality assessment of multi-frequency, dual-polarization GNSS-R data products. The evaluation uses an ancillary dataset including tide gauge measurements. The ancillary dataset also provides wind data which is used to examine the impact of wind on each GNSS-R data product.

Research Method

The methodology of sea level retrieval in this study is based on the estimation of interferometric frequency in the ground-based GNSS-R observations. To this end, the Least-Squares Harmonic Estimation (LS-HE) method is applied to a dataset of one year over 2016 for retrieving the interferometric frequency and calculating the height of reflecting surface. The LS-HE method can be simultaneously applied to estimate the frequency of interest in multiple sets of observations in the presence of data gaps or unevenly spaced data. The GNSS-R dataset includes I/Q output streams from each antenna. This gives the opportunity of using multiple series in the LS-HE analysis to boost the spectral analysis process. Using a sliding window, the LS-HE spectral analysis is partially applied to the time series of the reflection events from each GPS PRN. The size of this window is set to a minimum of 15-min but it is flexibly extended to 30-min to include at least two interferometric periods. The estimated heights from different satellites are combined by calculating the median value of the estimations.

Results

The results show that the combination of observations from L1 and L2 frequencies (L12) from a sea-looking LHCP antenna provides the best performance. Regarding the comparison of the products based on L1 and L2 frequencies, the L2 observations generally provides a lower degree of accuracy most likely suffering from fewer observations. In terms of antenna orientation, a seaward tilting with the angle of 90 degrees with respect to the zenith, optimizes the antenna again for capturing the sea-reflected signals and magnifies interferometric patterns. Concerning

the polarization, the analysis confirms that while the RHCP antenna can be readily used for grazing angles altimetry, using an antenna with LHCP design is the right choice for capturing the reflections at higher elevation angles.
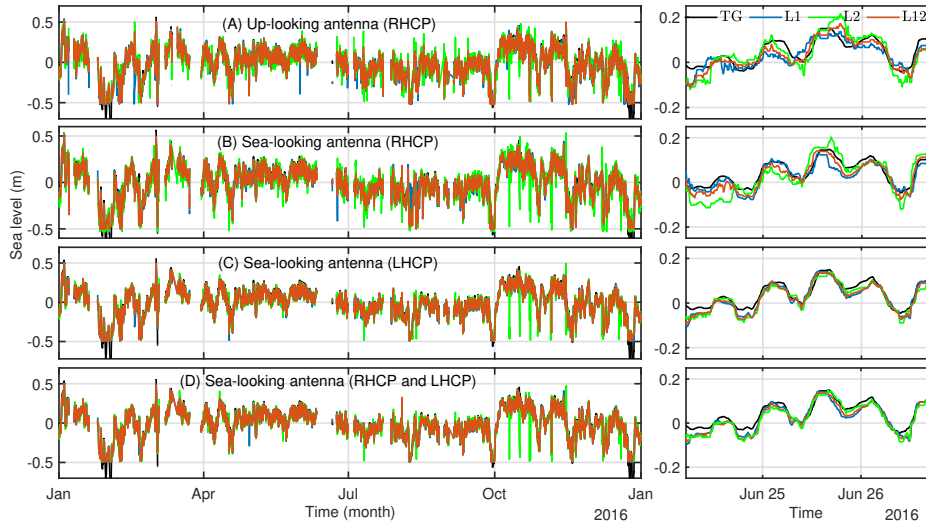
Figure 3.4: Time series of sea level anomalies derived from a one-year GNSS-R dataset (left panels), and zoomed views of a 2-day window (right panels), overlaid on the tide gauge (TG) measurements. The antennas used for the measurements are: (A) up-looking RHCP, (B) sea-looking RHCP, (C) sea-looking LHCP, and (D) sea-looking RHCP and LHCP. The lines with different colors show the estimates from different frequencies, i.e., L1 (blue), L2 (green), and combined L1 and L2 or L12 (red) (reused from [47]).

Figure 3.4 compares the sea level retrievals based on four different scenarios. Usage of different averaging windows can also affect the quality of final products. The RMSE values of GNSS-R sea levels from the LHCP sea-looking antenna compared to collocated tide gauge measurements are 2.4, 3.0, 4.5, 5.6 cm for 6, 3, 1, and 0.25-hour window size, respectively. The performance assessments of the measurement scenarios based on different averaging windows are summarized in Table 3.1. The investigation of wind effect on the accuracy of GNSS-R sea level measurements reports lower degree of accuracy during higher wind speeds. The RMSE value of the products can be more than 2 times larger in wind speeds above 14 m/s compared to calm sea surface, i.e., during wind speeds below 2 m/s. However, the final L12 sea level estimates show a better tolerance against the degrading effect of wind speeds.

Authors Contributions

Conceptualization, M.R. and M.H.; GNSS-R experiment and data, M.Ram., J.W.;

Table 3.1: The root mean square deviation (ε) and correlation coefficient (ρ) based on one-year GNSS-R sea level measurements compared to nearby tide gauge measurements. The values are based on different averaging windows for four measurement scenarios. *Scenario A* is based on observations from a zenith-looking RHCP antenna, *scenario B* includes observations from a seaward-oriented RHCP antenna, *scenario C* shows the results from a sea-looking LHCP antenna, and *scenario D* combines the observations from the RHCP and LHCP antennas. For each scenario, the columns L1, L2, and L12 respectively indicate the sea level measurements using the GPS L1, L2 carrier frequencies as well as their combined solution in the averaging step. The table is reused from [47].

Win = 6 h	L1	L2	L12
ε_A (cm)	4.6	5.7	4.1
ρ_A	0.963	0.943	0.969
ε_B (cm)	4.2	5.7	3.1
ρ_B	0.968	0.948	0.982
ε_C (cm)	2.4	3.6	2.4
ρ_C	0.990	0.977	0.990
ε_D (cm)	2.4	3.8	2.3
ρ_D	0.990	0.973	0.990
Win = 3 h			
ε_A (cm)	6.1	7.8	5.7
ρ_A	0.940	0.901	0.946
ε_B (cm)	5.3	7.1	4.4
ρ_B	0.951	0.923	0.967
ε_C (cm)	3.2	4.0	3.0
ρ_C	0.982	0.972	0.984
ε_D (cm)	3.1	4.2	3.0
ρ_D	0.983	0.970	0.984
Win = 1 h			
ε_A (cm)	8.6	10.4	8.14
ρ_A	0.893	0.847	0.901
ε_B (cm)	7.4	9.1	6.6
ρ_B	0.912	0.884	0.930
ε_C (cm)	4.7	5.3	4.5
ρ_C	0.964	0.954	0.967
ε_D (cm)	4.6	5.4	4.5
ρ_D	0.965	0.952	0.967
Win = 15 min			
ε_A (cm)	11.7	12.1	10.3
ρ_A	0.827	0.811	0.854
ε_B (cm)	9.3	10.9	8.7
ρ_B	0.870	0.846	0.886
ε_C (cm)	5.8	6.4	5.6
ρ_C	0.946	0.935	0.949
ε_D (cm)	5.6	6.3	5.6
ρ_D	0.948	0.837	0.949

Match-up wind data: R.H.; Data curation, M.R. and M.H.; Formal analysis, M.R., M.H., M.S.; Funding acquisition, M.R., M.G. and H.N.; Investigation, M.R. and M.H.; Methodology, M.R. and M.H.; Software, M.R., M.H. and M.S.; Supervision, H.N. and J.W.; Validation, M.R., M.H.; Visualization, M.R., M.H.; Writing—original draft, M.R., M.H.; Writing—review and editing, M.H., H.N., M.S., M.G., R.H. and J.W. All authors have read and agreed to the published version of the manuscript.

3.2.4 Paper D: Tidal Harmonics Retrieval using GNSS-RDual-Frequency Complex Observations

Content

This study investigated the potential of the ground-based GNSS-R technique for detecting and analyzing tidal constituents. The analysis is conducted using a relatively long dataset of six years obtained from a coastal GNSS-R experiment installed at Onsala Space Observatory. A highlight of this study was to utilize dual-frequency I/Q interferometric observations to retrieve sea level and tidal harmonics. We applied uni- and multi-variate Least Squares Harmonic Estimation (LS-HE) method for sea level calculation and estimating tidal constituents. The U-tide software is used to retrieve the amplitude and phase of a list of standard tidal harmonics.

Research Method

This study consists of three main stages (Fig. 3.5). The first stage is the data preparation through the time series associated with each reflection event. In the second stage, we focus on finding the interferometric frequency in the I/Q observations using multivariate Least Squares Harmonic Estimation (LS-HE) for the LHCP antenna. Then we calculate the sea surface heights based on the retrieved interferometric frequency from L1 and L2 observations. To combine the estimated sea surface heights from different satellites, we use an averaging window of 15 minutes for every 5 minutes time step. Overall, each height measurement is based on up to eight reflection events from one to four satellites at L1 and L2 frequencies. satellites reflection We use a native MATLAB function for outlier detection based on the median absolute deviation (MAD) values. All the values beyond three scaled MAD with respect to the median are considered outliers. To suppress the effect of any remaining outliers, the median value of the estimates within the averaging window is considered as the final height estimate. The last stage of the methodology is the validation of the GNSS-R height estimates with the collocated tide gauge observations and detecting of the tidal harmonics for both datasets, and comparing them in terms of amplitudes, period, and initial phases.

2. DATA AND METHODOLOGY

The dataset used in this study is the correlation sums at In-phase and Quadrature (I/Q) levels produced by the dedicated GNSS Occultation, Reflectometry, and Scatterometry (GORS) receiver [2, 5] from three antennas: a zenith-looking and two sea-looking antennas with a 98° tilt with respect to the zenith. The antennas are installed at about 3 meters above the sea surface level. We collocate two ancillary datasets from the nearest meteorological station and a tide gauge located about 300 meters away from the GNSS-R station.

The methodology of this study is focused on estimating sea levels during different wind speeds. The frequency of interferometric oscillations in the I/Q time series is related to sea level as follow [2]:

$$\delta\rho = 2\,\delta H\,sin(e)\,, \delta f = \frac{2\,\delta H\,cos(e)}{\lambda}\cdot\frac{de}{dt} \qquad (1)$$

where $\delta\rho$ is the path difference between the direct and reflected signals, e is elevation angle of the tracked satellite, δH is the height between the antenna and sea surface, λ is the signal wavelength and δf is the interferometric frequency which is retrieved using SSA.

Briefly, the methodology contains three main steps illustrated in Figure 1. The first step includes the data preparation described by [2]. The second or key step focuses on applying SSA to the time series of each PRN over reflection events. For detailed Information about SSA, readers could refer to [11]. The retrieved interferometric signal is then inverted to the sea level estimate. We finish this step by outlier removal and finding the median of the sea surface height in the step of 5 min with a temporal window of 3 hours. In the final step, we evaluate the estimated sea surface heights with respect to the tide gauge observations and different wind speeds.
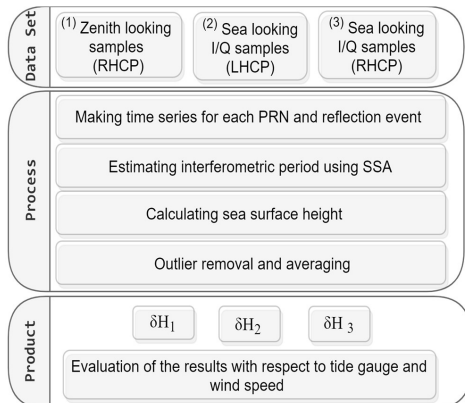
Fig. 1 Methodology flowchart based on the Singular Spectrum Analysis (SSA).

3. RESULTS AND DISCUSSION

The results of the SSA-based sea level retrievals from the GNSS-R dataset are presented and discussed in this section. Figure 2 shows an example of applying SSA to the I/Q time series to extract the interferometric fringes. The method can simultaneously mitigate other irrelevant components. As seen in the figure, the applied method can effectively reveal the amplitude variations of the interferometric signal. The detected peaks in the bottom panel of Fig. 1 are used to estimate the period of interest for the calculation of height according to (1).
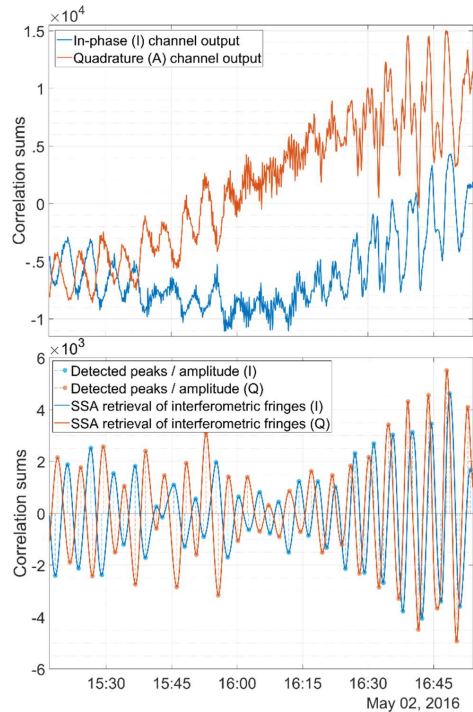
Fig. 2 - Top panel: an example of the in-phase / quadrature (I/Q) time series from GPS PRN 12 on May 02, 2016. Bottom panel: the result of retrieving interferometric fringes from the I/Q correlation sums using Singular Spectrum Analysis (SSA). The dark and light blue separate the in-phase and quadrature samples, respectively. The dots in the bottom panel show the detected peaks after applying SSA. The dashed lines illustrate the estimated amplitude.

Figure 3 shows the distribution of sea level anomalies from GNSS-R against tide gauge observations. The measurements from the sea-looking LHCP antenna shown on the right panel represent the best performance compared to both zenith-looking and sea-looking RHCP antennas.

8329
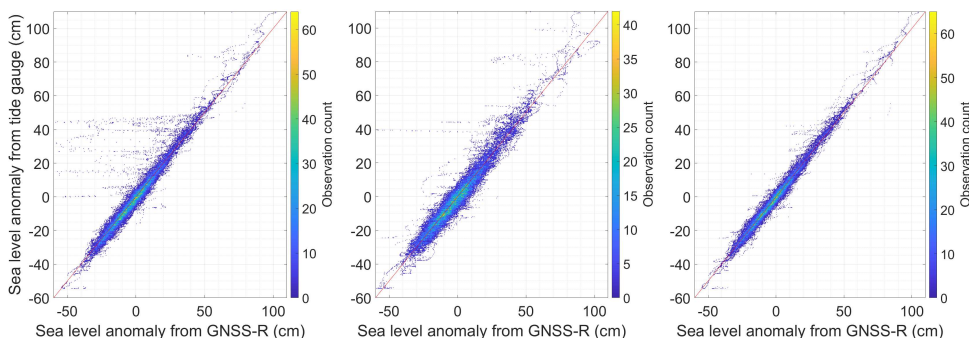
Fig. 3 – Comparisons of GNSS-R sea level measurements with respect to tide gauge data. The GNSS-R measurements are based on the application of Singular Spectrum Analysis (SSA) to the observations from the antennas in different polarizations, i.e. Right- and Left-Handed Circular Polarization (RHCP and LHCP), and two orientations, i.e. zenith-looking and sea-looking. The left panel shows the results of the zenith-looking RHCP antenna, the middle panel is associated with the sea-looking RHCP antenna, and the right panel depicts the measurements from the sea-looking LHCP antenna. The red lines overlaid on the plots show the one-to-one relationship.

The larger errors from the zenith-looking antenna in the left panel compared to the middle panel shows that the change of the antenna orientation towards the sea improves the accuracy of the GNSS-R sea level measurements.

To evaluate the possible impact of sea surface roughness on the sea level measurement, we use the collocated wind measurements. Figure 4 gives an overview of the impact of different sea states on the accuracy of the measurements. The figure shows that as the wind speed increases, the accuracy of the retrieved sea level degrades for all the antenna configurations. The investigation also reveals that the wind speeds can impose a bias in the measurements. The bias, in turn, has a contribution to the accuracy.

It should be noted that the limited fetch at coastal GNSS-R experiments can partially shield the nearby sea surface against some wind directions. As reported by [2], this can result in different sea surface roughness for wind speeds from different directions. The roughness estimates from the latter study based on the same dataset are used here to evaluate possible dependency between the roughness and the GNSS-R sea level retrievals. The top panel in Fig. 5 provides an overview of roughness estimates against different wind speeds and directions. A delicate dependency between the height measurement errors and the roughness estimates can be seen in the bottom panel of Fig. 5.
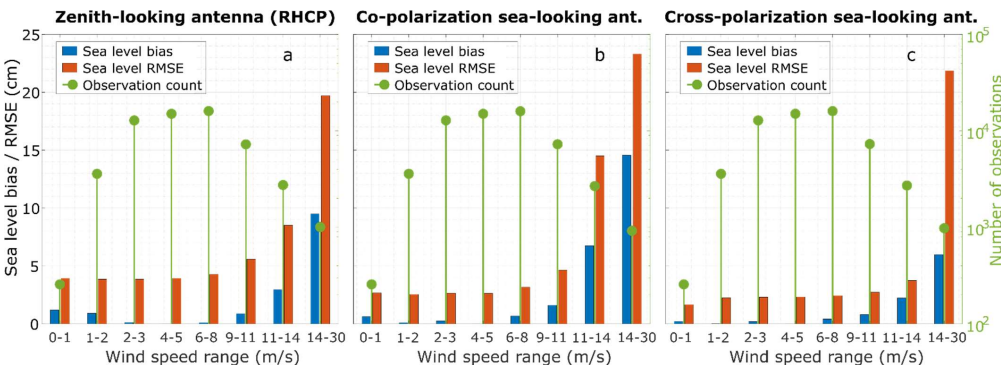
Fig. 4 - A performance assessment of GNSS-R sea level measurements at different ranges of wind speed. The sea level measurements are based on the application of Singular Spectrum Analysis (SSA) to the observations from the antennas in different polarizations, i.e. Right and Left Handed Circular Polarization (RHCP and LHCP), and two orientations, i.e. zenith-looking and sea-looking. The left, middle, and right panels show the results from a zenith-looking RHCP antenna, a sea-looking RHCP antenna, and a sea-looking LHCP antenna, respectively. The blue bars show the bias of the two datasets, i.e. the GNSS-R and tide gauge data, over each wind speed range. The red bars depict the Root Mean Squared Errors (RMSE) of the GNSS-R sea level measurements with respect to the tide gauge observations. The number of observations over each wind speed range is shown by green lines.

8330
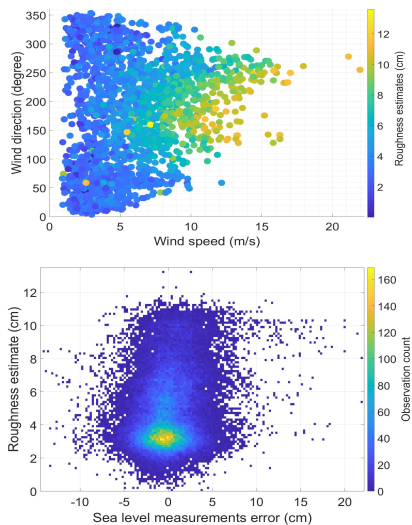
Fig. 5 - Top panel: the estimates of sea surface roughness in terms of the standard deviation of height. The estimates are obtained from [2]. Bottom panel: the distribution of GNSS-R sea level measurement errors with respect to the sea surface roughness.

4. CONCLUSION

The results of sea level measurements from GNSS-Reflectometry observations in a coastal experiment are presented in this study. To retrieve these measurements, we applied Singular Spectrum Analysis to the in-phase and quadrature observations from three antennas with different polarizations and orientations. Comparison of collocated tide gauge observations with the GNSS-R sea level retrievals from different antenna polarizations and orientations reports an overall Root Mean Square Error (RMSE) ranging from 2.8 to 4.7 cm for a period of one year, i.e. from January to December 2016. The measurements from a seaward-tilted LHCP antenna showed the best performance for sea level monitoring. The presence of measurement bias during different wind speeds was detected in the analysis. However, the reported biases could be different for other GNSS-R experiments since the location of our setup is surrounded by complex coastlines. These coastlines can minimize the impact of winds for some of the directions.

5. ACKNOWLEDGMENT

6. REFERENCES

[1] F. Geremia-Nievinski *et al.*, "SNR-based GNSS reflectometry for coastal sea-level altimetry: results from the first IAG inter-comparison campaign," *Journal of Geodesy,* vol. 94, no. 8, pp. 1-15, 2020.

[2] M. Hoseini *et al.*, "On the Response of Polarimetric GNSS-Reflectometry to Sea Surface Roughness," *IEEE Transactions on Geoscience and Remote Sensing,* 2020.

[3] C. Chew and E. Small, "Soil moisture sensing using spaceborne GNSS reflections: Comparison of CYGNSS reflectivity to SMAP soil moisture," *Geophysical Research Letters,* vol. 45, no. 9, pp. 4049-4057, 2018.

[4] M. Rajabi, H. Nahavandchi, and M. Hoseini, "Evaluation of CYGNSS Observations for Flood Detection and Mapping during Sistan and Baluchestan Torrential Rain in 2020," *Water,* vol. 12, no. 7, p. 2047, 2020.

[5] A. M. Semmling *et al.*, "Sea-Ice Concentration Derived From GNSS Reflection Measurements in Fram Strait," *IEEE Transactions on Geoscience and Remote Sensing,* vol. 57, no. 12, pp. 10350-10361, 2019.

[6] M. Hoseini, M. Asgarimehr, V. Zavorotny, H. Nahavandchi, C. Ruf, and J. Wickert, "First evidence of mesoscale ocean eddies signature in GNSS reflectometry measurements," *Remote Sensing,* vol. 12, no. 3, p. 542, 2020.

[7] M. Asgarimehr, V. Zavorotny, J. Wickert, and S. Reich, "Can GNSS reflectometry detect precipitation over oceans?," *Geophysical Research Letters,* vol. 45, no. 22, pp. 12,585-12,592, 2018.

[8] G. Foti, C. Gommenginger, and M. Srokosz, "First Spaceborne GNSS-Reflectometry Observations of Hurricanes From the UK TechDemoSat-1 Mission," *Geophysical Research Letters,* vol. 44, no. 24, pp. 12,358-12,366, 2017.

[9] K. M. Larson, J. S. Löfgren, and R. Haas, "Coastal sea level measurements using a single geodetic GPS receiver," *Advances in Space Research,* vol. 51, no. 8, pp. 1301-1310, 2013.

[10] M. Rajabi, A. Amiri-Simkooei, H. Nahavandchi, and V. Nafisi, "Modeling and Prediction of Regular Ionospheric Variations and Deterministic Anomalies," *Remote Sensing,* vol. 12, no. 6, p. 936, 2020.

[11] M. Hoseini, F. Alshawaf, H. Nahavandchi, G. Dick, and J. Wickert, "Towards a zero-difference approach for homogenizing gnss tropospheric products," *GPS Solutions,* vol. 24, no. 1, p. 8, 2020.

[12] M. Rajabi, A. Amiri-Simkooei, J. Asgari, V. Nafisi, and S. Kiaei, "Analysis of TEC time series obtained from global ionospheric maps," *Journal of Geomatics Science and Technology,* vol. 4, no. 3, pp. 213-224, 2015.

Polarimetric GNSS-R Sea Level Monitoring using I/Q Interference Patterns at Different Antenna Configurations and Carrier Frequencies

Mahmoud Rajabi, Mostafa Hoseini, Hossein Nahavandchi, Maximilian Semmling, Markus Ramatschi, Mehdi Goli, Rüdiger Haas, Jens Wickert

Abstract—Coastal sea level variation as an indicator of climate change is extremely important due to its large socio-economic and environmental impact. The ground-based Global Navigation Satellite System (GNSS) reflectometry (GNSS-R) is becoming a reliable alternative for sea surface altimetry. We investigate the impact of antenna polarization and orientation on GNSS-R altimetric performance at different carrier frequencies. A one-year dataset of ground-based observations at Onsala Space Observatory using a dedicated reflectometry receiver is used. Interferometric patterns produced by the superposition of direct and reflected signals are analyzed using the Least-Squares Harmonic Estimation (LS-HE) method to retrieve sea surface height. The results suggest that the observations from GPS L1 and L2 frequencies provide similar levels of accuracy. However, the overall performance of the height products from the GPS L1 show slightly better performance owing to more observations. The combination of L1 and L2 observations (L12) improves the accuracy up to 25% and 40% compared to the L1 and L2 heights. The impacts of antenna orientation and polarization are also evaluated. A sea-looking Left-Handed Circular Polarization (LHCP) antenna shows the best performance compared to both zenith- and sea-looking Right-Handed Circular Polarization (RHCP) antennas. The results are presented using different averaging windows ranging from 15-minute to 6-hour. Based on a 6-hour window, the yearly Root Mean Square Error (RMSE) between GNSS-R L12 sea surface heights with collocated tide gauge observations are 2.4, 3.1, and 4.1 cm with the correlation of 0.990, 0.982, and 0.969 for LHCP sea-looking, RHCP sea-looking, and RHCP up-looking antennas, respectively.

Index Terms—Global Navigation Satellite Systems-Reflectometry (GNSS-R), Coastal Sea Level Monitoring, Polarimetric GNSS-R, Altimetry, GPS, GNSS, L-Band Remote Sensing, Least-Squares Harmonic Estimation (LS-HE)

I. INTRODUCTION

SEA surface level is a key parameter in many scientific disciplines, including geology, geodesy, oceanography and archaeology which could contribute to recognizing climate and environmental variation. Modern civilization could be affected by major and minor changes in sea surface level due to global warming and natural causes such as floods, tsunami and volcanoes [1]. The information about sea surface level is also vital due to the large population, economic and commercial activities in coastal areas. In addition, sea surface level is essential to defining vertical datum (geoid) and consequently, measuring and understanding Earth's geometric shape. Therefore, it is essential to monitor sea surface level using accurate and reliable methods.

Two prevalent methods have been used for sea level monitoring, traditional tide gauges, and spaceborne radar altimeters. These methods have some limitations. The tide gauge measurements are point-wise and also affected by subsidence, tectonics and human activities [1]. Close to the coastal area, data accuracy of the radar altimeters is degraded due to the effect of the land on its large footprint, and the corrections which are applied for geophysical effects. Consequently, we do not have reliable and accurate spaceborne radar observations in the coastal area besides the limitation on the spatiotemporal resolution of this method [2].

Global Navigation Satellite Systems (GNSS) were designed primarily for providing positioning, navigation, and timing services. The GNSS signals are also being used for numerous remote sensing applications of the Earth's surface and atmosphere, in addition to its primary aim. GNSS-Reflectometry (GNSS-R) as a state-of-the-art remote sensing technique, uses reflected GNSS signals to retrieve and investigate numerous geophysical parameters and phenomena over the Earth's surface (land, ocean, and ice). GNSS-R is a multi-static radar technique in the L-band range of the electromagnetic signals, which works in all weather conditions, day and night, and is ideal for measuring or detecting many variables and natural events, such as sea level [3], sea surface roughness [4], ocean eddies [5], sea ice and snow depth [6], flood [7], precipitation [8], wind speed [9] .

Ground-based GNSS-R can act as a multi-purpose sensor, which has drawn attention over the past decades. The method is an alternative option for traditional tide gauges for monitoring sea surface level in coastal areas. A GNSS-R sensor can cover a wider area of the sea surface and collect additional useful data from the reflecting surface, e.g. sea surface roughness and ice coverage. Tide-gauges measurements can be affected by local vertical displacements and require extra procedures to

M. Rajabi, M. Hoseini and H. Nahavandchi are with the Department of Civil and Environmental Engineering, Norwegian University of Science and Technology, 7491 Trondheim, Norway (e-mail: mahmoud.rajabi@ntnu.no).

M. Semmling is with the German Aerospace Center DLR, Institute for Solar-Terrestrial Physics, Neustrelitz, Germany.

M. Ramatschi is with the Department of Geodesy, German Research Center for Geosciences (GFZ), 14473 Potsdam, Germany.

M. Goli is with Faculty of Civil and Architectural Engineering, Shahrood University of Technology, Iran.

R. Haas is with the Department of Space, Earth and Environment, Chalmers University of Technology, Gothenburg, Sweden

J. Wickert is with the Department of Geodesy, German Research Centre for Geosciences (GFZ), 14473 Potsdam, Germany, and also with the Institute of Geodesy and Geoinformation Science, Technische Universität Berlin, Germany

connect the measured relative sea level to the global reference frame. In contrast, coastal GNSS-R stations can monitor and correct the local vertical displacements and provide sea level measurements in the global reference frame. The concept of sea surface level monitoring using GNSS-R was conceived in 1993 [3] and applied for ground-based GNSS-R stations signals in 2000 [10]. Afterward, the performance and reliability of the method have been studied in several cases, e.g. [11, 12, 13, 14, 15, 16, 17].

Most of the ground-based GNSS-R altimetry experiments have used an up-looking geodetic antenna and ordinary surveying receiver based on the Signal to Noise Ratio (SNR) observations of the Global Positioning System (GPS). In addition, various configurations have been considered in different studies in terms of antenna orientation, polarization, and receiver type. For example, Santamaria-Gomez and Watson [18] used three weeks of SNR data in Spring Bay, Australia, from a side-looking GNSS Right-Handed Circular Polarization (RHCP) antenna to improve the SNR altimetry performance compared to a zenith-looking antenna. Padokhin et al. [19] used a four-day dataset obtained from a side-looking and a zenith-looking geodetic antenna to investigate the influence of the antenna layout and the impact of wind waves on GNSS-R altimetry. Alonso-Arroyo et al. [20] utilized three-month data based on a tilted antenna to see how the reflected GNSS signals were affected by coastal sea state. Rodriguez-Alvarez et al. [21] and Hongguang et al. [22] also used a single side-looking antenna for sea level altimetry.

A few studies have utilized dedicated reflectometry receivers with tilted antennas. For example, Semmling et al. [23] use an Occultation, Reflectometry, and Scatterometry (GORS) receiver. Liu et al. [24] reports a monthly RMSE of 4.37 cm with respect to tide gauge observations using GPS L1 and a tilted Left-Handed Circular Polarization (LHCP) antenna [24]. The latter study uses phase observations during coherent reflection events which limits the measurements to the reflection at low elevation angles or during lower sea states. Fran Fabra et al. [25] used coherent differential phase between direct and both LHCP and RHCP reflected signals for the retrieval of absolute ellipsoidal heights over sea ice. Lifeng Bao et al. [26] to improve precision and spatial resolution of GNSS-R altimetry used one up-looking geodetic GNSS receiver, one downward LHCP antenna, and an atomic clock.

This study aims to give an inter-comparison overview of GNSS-R altimetry observations recorded using different antenna designs and carrier frequencies. Compared to the typical geodetic installations, the tilted antenna orientation coupled with different polarizations strengthens the power of captured interferometric patterns. This can prolong the detectability of these patterns at higher elevation angles. A multivariate spectral analysis method is used here to take the advantage of available concurrent observations. Moreover, the quality of the observations made by each satellite Pseudo Random Noise (PRN) is assessed.

We design different scenarios for the investigation using a dedicated reflectometry receiver under similar conditions, i.e. the same processing method, antenna model, location and weather conditions. The variable parameters in the scenarios are antenna polarizations and orientations, as well as carrier frequency of the signal. The analysis includes the impact of different wind speeds and averaging windows. A relatively long-term dataset from a coastal GNSS-R station with special design and unique features, which is established by the German research center for geosciences (GFZ) is used. The Least-Squares Harmonic Estimation (LS-HE) method is used for spectral analysis and finding the frequency of interferometric signals. The interferometric or compound signal is generated as a result of interference of direct and reflected signals. The frequency observations of the interferometric signals are used to calculate sea surface height. The LS-HE method has the capacity of multivariate formulation and is not limited to integer frequencies and evenly spaced data [27]. The rest of this paper is organized as follows. The study area and dataset are presented in Section 2. The methodology and mathematical concepts are described in Section 3. The discussion of data processing and the results are explained in Section 4. Finally, the paper is finalized by a conclusion in Section 5.

II. DATA AND SITE

We use a one-year dataset from January to December 2016 obtained from a dedicated GNSS-R site installed and operated by GFZ. This is one of the two GNSS-R stations at Onsala Space Observatory in Sweden ($57.393°N$, $11.914°E$). The observations with elevation angles between 5 and 40 degrees are selected for the investigation. Besides the GNSS-R observations, we use two ancillary datasets including the wind and sea level measurements from a close by meteorological station and a traditional tide gauge. Both are operated by the Onsala Space Observatory and located at about 300 m distance from the GNSS-R station. Figure 1 shows the study area, reflection points for different PRNs, and a picture of the station antennas and their orientations. A schematic view of the experiment setup and an example of the receiver outputs for satellite PRN 3 during a reflection event is shown in Figure 2.

The station antennas are installed on a concrete foundation with an approximate height of 3 meters from the sea surface. Three types of antennas are installed at the station, one is up-looking and the two others are sea-looking. The up-looking antenna is RHCP and assigns higher gain values to direct GPS signals for acquisition and tracking purposes. The sea-looking antennas with RHCP and LHCP designs are considered for tracking sea reflected GPS signals at two different polarizations. The tilt angle between the up-looking and sea-looking antennas is 98°. Usage of a single side-looking antenna would cause difficulty to continuously track the direct signals due to significant contributions from the reflected signals. Therefore, an upright antenna needs to be used as the master link for the tracking. It should be noted that the side-looking antennas can partially block the reception of reflections in the up-looking antenna. Therefore, the up-looking antenna used at Onsala station might not provide exactly equivalent configuration compared to a single isolated upright antenna.

A GORS receiver [28] with four antenna inputs is utilized in the experiment. The first input is dedicated to the master channel of the receiver and is connected to the up-looking
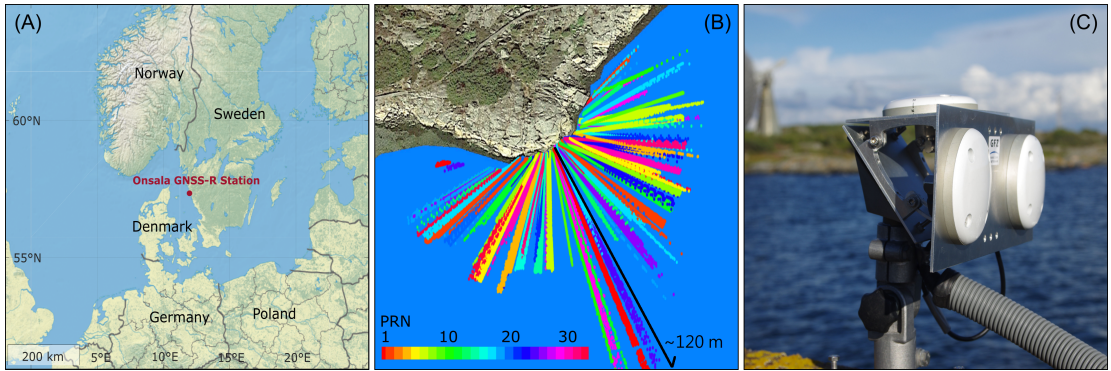
Fig. 1. (A) The red point on the map shows the Onsala GNSS-R station in the southwest of Sweden which the experiment setup is installed there. (B) The scatter plot of the reflection points over the sea surface. The colors show the GPS PRN numbers related to the reflection tracks. (C) The experiment setup and antenna orientations (up- and sea-looking).
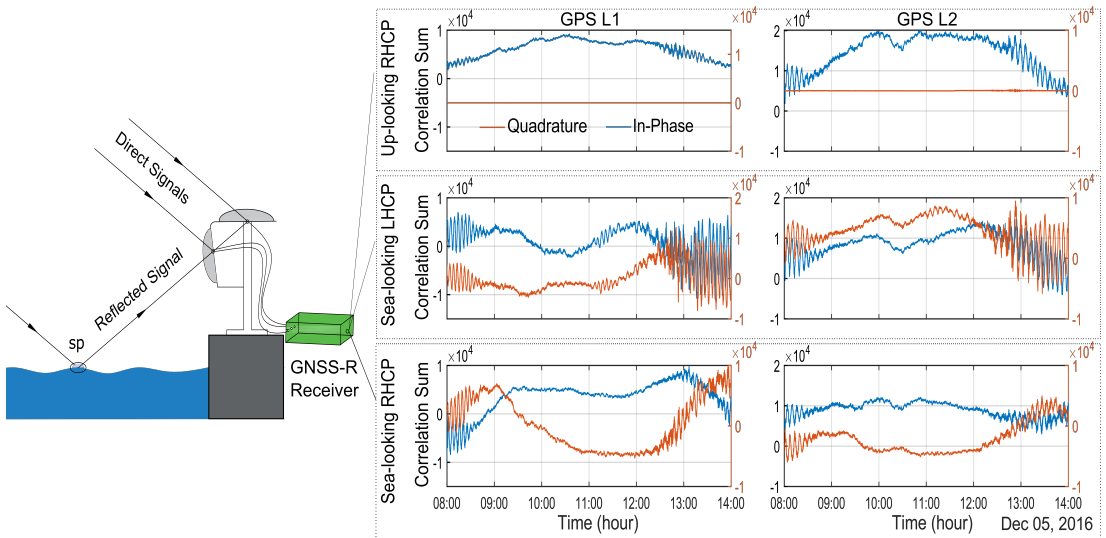
Fig. 2. A schematic view of the GNSS-R experiment setup on the left. The right graphs illustrate example time series of the in-phase and quadrature correlation sums from each antenna in GPS L1 and L2 bands. The graphs are related to a reflection event on December 5, 2016 from the GPS PRN 3. The specular point is denoted by "sp".

antenna. The second and third inputs are used for the slave channels and are connected to the sea-looking antennas.

According to [29] the signal processing flow in the dedicated reflectometry receiver can be briefly described as follows (See Figure 3 for a schematic representation of the receiver architecture). The received signal, i.e. $E_d + E_r$ in Figure 3, after digitization in the receiver can be written as:

$$s(t) = A\,D(t - \tau)\,C(t - \tau)\,cos(2\pi(f_{IF} + f_D)t + \varphi) \quad (1)$$

with $s(t)$ being the received signal, A the amplitude, D and C respectively the modulated navigation data and the PRN code,

t the time, τ the code delay, f_{IF} an intermediate frequency, f_D the Doppler frequency shift, and φ is an initial phase. The receiver generates the following models of the carrier signal at In-phase and Quadrature (I/Q) levels in the master channels:

$$
\begin{aligned}
\text{in-phase}: \quad & \cos(2\pi(f_{IF} + \tilde{f}_D)t + \tilde{\varphi}) \\
\text{quadrature}: \quad & \sin(2\pi(f_{IF} + \tilde{f}_D)t + \tilde{\varphi}) \quad (2)
\end{aligned}
$$

where $\tilde{f}_D$ and $\tilde{\varphi}$ are estimated Doppler frequency and initial phase which are produced by a closed-loop tracking process in the receiver. After multiplying the received signal by the two models and applying a low pass filter, the results are correlated

E_d : Direct electromagnetic signal
E_r : Reflected electromagnetic signal
f_IF : Intermediate Frequency
f̃_D : Estimated Doppler frequency
τ̃ : Delay of the direct signal path
φ̃ : Estimated initial phase

δf_D : Doppler frequency shift of the reflected signal
δτ : The reflection path extra delay
LPF: Low pass filter
$\otimes$: Multiplier

Fig. 3. A schematic diagram of the dedicated GNSS-Reflectometry receiver architecture used in this study.

with the PRN code of the satellite. The navigation data is then demodulated to yield a phasor (γ_m) as the output of the master channel [23]:

$$\gamma_m(\tilde{\tau}) \quad = \quad e^{-j\delta\varphi}[A_d + A_r e^{jk\delta\rho}\Lambda(\Delta\tau)] \qquad (3)$$

where $\tilde{\tau}$ is the delay of direct signal which is estimated within the closed-loop tracking process, j is the imaginary unit ($j^2 = -1$), $\delta\varphi$ is the phase difference between the compound and direct signals, the amplitudes of the direct and reflected signals are A_d and A_r, respectively, and $k = 2\pi/\lambda$ is the carrier wavenumber with λ being the carrier wavelength. Figure 4 shows phasor representations of the direct, reflected, and compound signals with the reflectometry relative phase
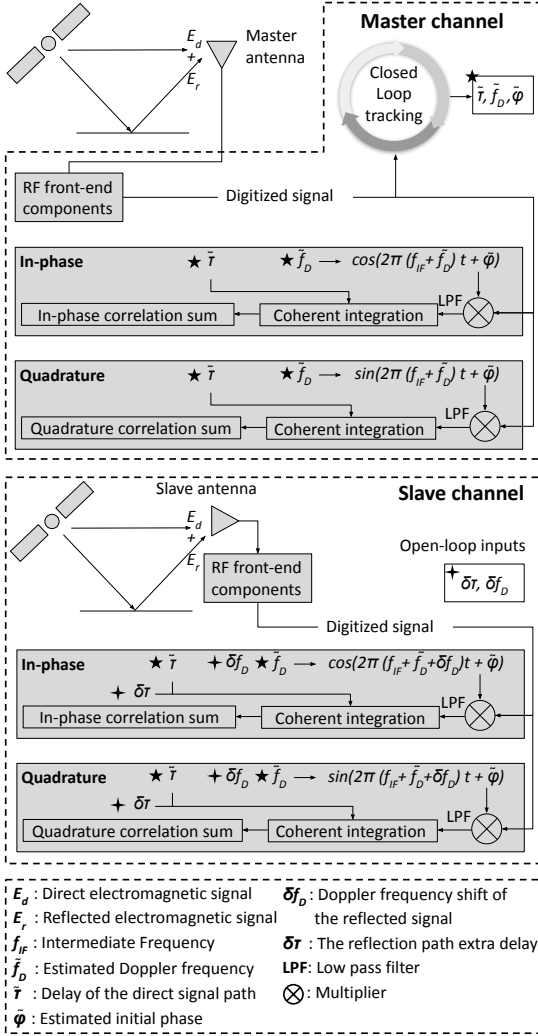
$\psi = k\,\delta\rho$. The parameter $\Delta\tau$ denotes the time delay due to the excess path ($\delta\rho$) traveled by the reflected signal compared to the direct path. The function $\Lambda(\Delta\tau)$ is triangular auto-correlation function with the properties: $\Lambda(0) = 1$ and $\Lambda(\tau) = \Lambda(-\tau)$. Under successful operation of the phase lock-loop (Fig. 4-B), the amplitude of the signal is completely tracked in the in-phase component of the master channel, I_m [29]. Therefore, the quadrature component of the master channel, Q_m, vanishes and the signal SNR can be calculated by squaring I_m, expressed by:

$$A_c^2 = I_m^2 = A_d^2 + A_r^2 + 2A_d A_r \cos(k\delta\rho) \qquad (4)$$

where A_c is the amplitude of the compound signal. The SNR value expressed in (4) is similar to the SNR observations from geodetic receivers described in [30]. The parameter $\delta\rho$ will be later used for the sea level retrieval (see section III).

For the slave channels, the receiver can be steered through an open-loop scheme using external inputs for tracking the signals intercepted by the slave antennas. The external inputs, δf_D and $\delta\tau$, are relative values with respect to the reference values $\tilde{\tau}$ and $\tilde{f}_D$. The parameter δf_D is used during carrier wipeoff and $\delta\tau$ for the code correlation in the slave channel. The slave channel output can be expressed by:

$$\gamma_s(\tilde{\tau} + \delta\tau) \quad = \quad e^{-j\,\delta\varphi}[A_d'\,\Lambda(\delta\tau) + $$
$$A_r'\,e^{j\,k\,\delta\rho}\,\Lambda(\delta\tau - \Delta\tau)] \qquad (5)$$

where subscript s refers to the slave channels. A_d' and A_r' are respectively the amplitudes of direct and reflected signals in the slave channel. The amplitudes of direct and reflected signals are different in the master and slave channels, mainly because of the different antenna gains. Figure 4-C shows a simplified phasor representation of direct, reflected, and compound signals in the slave channel.

The low reflector height at the Onsala GNSS-R station with respect to the sea surface results in $\delta f_D \approx 0$ and $\delta\tau \approx \Delta\tau \approx 0$. Therefore, the receiver outputs for the slave channels at I/Q levels can be simplified to:

$$\gamma_s \quad = \quad A_c'\,e^{j\Delta\varphi} = I_s + jQ_s$$
$$= \quad e^{-j\delta\varphi}[A_d' + A_r'\,e^{j\,k\,\delta\rho}] \qquad (6)$$

where $\Delta\varphi$ is the slave-master phase difference and A_c' is the amplitude of the compound signal in the slave channel. The I/Q components of the slave channel output can be written as:

$$I_s \quad = \quad A_d'\cos(\delta\varphi) + A_r'\cos(k\,\delta\rho - \delta\varphi)$$
$$Q_s \quad = \quad -A_d'\sin(\delta\varphi) + A_r'\sin(k\,\delta\rho - \delta\varphi) \qquad (7)$$

The first terms of (7) are related to the contribution of the direct signal while the second terms comprise the effect of the reflected signal:

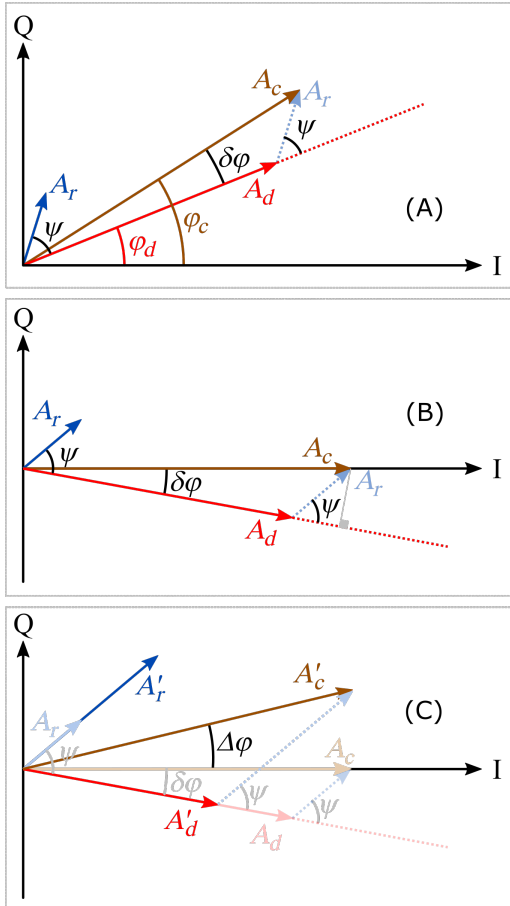$$I_s \quad = \quad I_d + I_r$$
$$Q_s \quad = \quad Q_d + Q_r \qquad (8)$$

Fig. 4. The phasor diagrams of direct, reflected, and compound signals respectively denoted by subscript d, r, and c in the in-phase/quadrature (I/Q) axes: (A) before and (B) after tracking the phase of the compound signal in the master channel. The phasor diagram shown in (C) is related to the slave channel. The angle ψ is the reflectometry-relevant phase, $\delta\varphi$ is the phase difference between the compound and direct signals, and $\Delta\varphi$ is the phase of the compound signal in the slave channel. The phase shifts due to baseline between the master and slave antennas and different carrier phase wind-up effects for the up-looking and side-looking antennas are not included in the figure.

The direct signal terms, i.e. I_d and Q_d, can be extracted e.g. by fitting a low-order polynomial. The amplitude and frequency of the interferometric patterns in the reflected signal terms, i.e. I_r and Q_r, can be determined through different spectral analysis or modeling methods. The LS-HE method, which is further described in the next section, can simultaneously model the direct signal effects and retrieve period of the interferometric oscillations from the I/Q samples. The amplitude of the direct,

reflected, and compound signals in the slave channels can be respectively calculated by:

$$
\begin{aligned}
A_d'^2 &= I_d^2 + Q_d^2 \\
A_r'^2 &= I_r^2 + Q_r^2 \\
A_c'^2 &= I_s^2 + Q_s^2 \\
&= A_d'^2 + A_r'^2 + 2A_d'A_r'\cos(k\delta\rho + \phi_0) \quad (9)
\end{aligned}
$$

where ϕ_0 is an initial phase shift. The original output of the GORS receiver is based on 5-millisecond coherent integration, i.e. 200 Hz sampling rate. In this study, the 200 Hz correlation sums are down-sampled using a 10-second (0.1 Hz) integration at I/Q levels for each of the antennas.

In general, having access to the I/Q outputs gives the opportunity of looking at the signal in a 3D sense and retrieving the phase of interferometric signal and the coherence state [24]. In this study, we directly utilize the I/Q outputs. Both of the components encompass the oscillating interferometric patterns regardless of the coherency of the reflection. This feature in both of the I/Q components is used here to detect the corresponding Doppler residual in a multivariate approach as described below.

III. METHOD

The methodology of this study contains three main stages (Fig. 5). The first stage is the data preparation through which the time series associated with each reflection event are created. In the second stage, we focus on finding the interferometric frequency using multivariate LS-HE in different scenarios. The frequency (L1/L2) and polarization (RHCP/LHCP) of the reflected signals as well as the orientation of the antenna (up-/sea-looking) are variable factors in these scenarios.

Four main scenarios for the estimation of the sea surface heights are designed as follow, each one using L1 and L2 separately: (A) using the I components of the up-looking RHCP antenna (one time series), (B) using the I/Q components of the sea-looking RHCP antenna (two time series), (C) using the I/Q components of the sea-looking LHCP antenna (two time series), (D) using the I/Q components of the both sea-looking antennas (four time series). In addition, the sea surface heights are estimated by combining the retrieved heights from L1 and L2 for each main scenario for possible improvement. Consequently, the sea surface heights are retrieved in 12 different solutions. These products make it possible for us to assess the performance of polarimetric GNSS-R in different antenna's angle plus the performance of L1, L2, and combination of them (L12). The parameter of interest in the LS-HE analysis is the period of the interferometric signals.

The time series of the reflection events are divided into smaller segments by considering a time window. The time window for retrieving this periodic pattern is set to a minimum of 15 min but it is flexibly extended to 30 min until it includes at least two interferometric periods. It is worth mentioning that higher antenna height with respect to the sea surface could have reduce this window size resulting in a better temporal
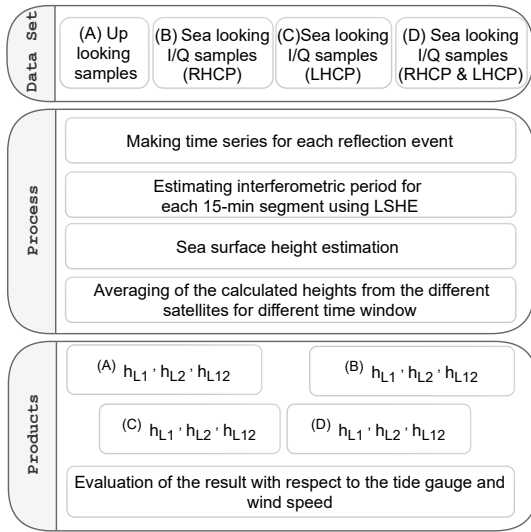
Fig. 5. Methodology flowchart based on the Least Squares Harmonic Estimation (LS-HE).

resolution. We move the overlapping window and analyze the segment with a time step of 1-min to cover the whole time series. The sea surface height is estimated from each segment.

To combine the estimated heights from different satellites we use an averaging window. For outlier detection, we use a native MATLAB function that utilizes the median absolute deviation (MAD) values. All the values beyond three scaled MAD with respect to the median are considered as outliers. After outlier elimination, the median value of the estimates within the averaging window is considered as the final height estimate. The final estimates are calculated every 5 minutes with different averaging windows ranging from 15 minutes to 6 hours (6-hours, 3-hours, 1-hours, and 15 minutes). The last stage of the methodology is the validation of the GNSS-R height estimates with the collocated tide gauge observations at different wind speeds.

A. Least-Squares Harmonic Estimation (LS-HE)

The LS-HE is one of the frequency analysis methods from the generation of the Fourier spectral analysis. The method is restricted to neither integer frequencies nor evenly-spaced time series and can be applied to datasets with gaps. The LS-HE method can efficiently include a linear trend as a deterministic part of the model and the covariance matrix as the stochastic part of the model [31]. One important feature of the method compared to the least squares spectral analyses described by earlier studies e.g. [32, 33, 34] is the multivariate formulation to identify common-mode signals of multiple time series. This feature has been utilized in scenarios B, C, and D to enhance retrieval of the common interferometric signal. For scenario A which includes only one time series, the analysis becomes univariate. The LS-HE method was presented and

utilized by [27] for the GPS position time series, then applied by [35] for the estimation of GNSS-R lake ice thickness and here is introduced for GNSS-R altimetry. For more information about the theory of LS-HE, we may refer to [36, 27, 31].

B. Sea surface height calculation

The superposition of direct and reflected signals constructs compound signals. The concept of calculating the sea surface height from the GNSS-R observations is based on the retrieval of the interferometric patterns in the compound signal. The LS-HE method used in this study includes individual linear terms for each of the I/Q components of the master or slave samples. These linear terms can absorb the effect of direct signal variations (see (7)). Therefore, the effect of direct signal and interferometric oscillations can be effectively separated within the LS-HE analysis. The estimated interferometric period by LS-HE can then be related to the geometry of the reflection as described below.

The difference between the direct and reflected signals paths creates a Doppler shift which is in fact the frequency of the interferometric fringes [28]:

$$\delta f = \frac{1}{\lambda} \frac{d(\delta \rho)}{dt} \tag{10}$$

$$\delta \rho = \rho_{ref} - \rho_{dir}, \tag{11}$$

Fig. 6. Schematic geometry of the ground-based GNSS-R altimetry based on the path difference between the direct and reflected satellite signals. ρ_{sat-sp} is the distance between the satellite and specular point, $\rho_{sat-rec}$ is the distance between the satellite and receiver antenna, ρ_{sp-rec} is the distance between the specular point and receiver antenna, e is the satellite elevation angle, $\delta \rho$ is the extra path of the reflected signal compared to the direct signal, and h is the height difference between the phase center of the antenna and sea surface.

Fig. 7. Examples of observation time series of PRN 26 for one segment which are used to retrieve interferometric period (T_{int}) using multivariate LS-HE formulation. (A_1) and (B_1) show the In-phase and Quadrature components for GPS L1 and L2, respectively. (A_2) and (B_2) illustrate the dominant interferometric period retrieved by LS-HE based on different combinations of the time series.
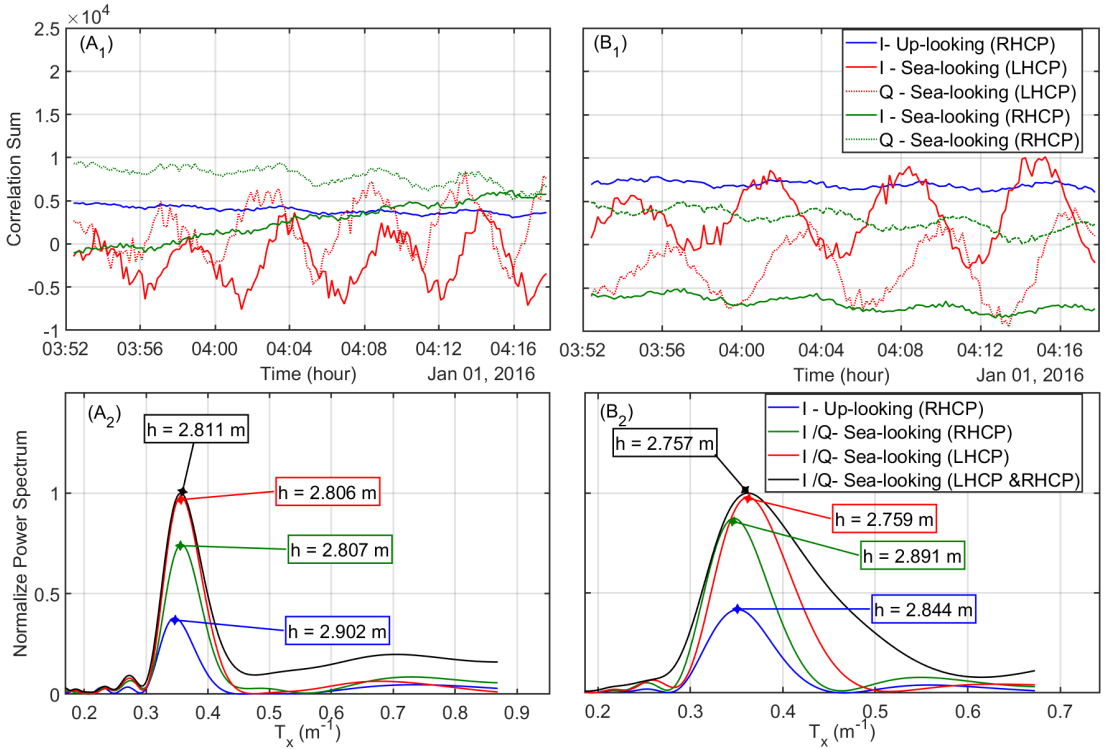
where ρ_{dir} and ρ_{ref} are the distance between the satellite and the antenna for direct and reflected signals, respectively, δf is the Doppler shift, and λ is the wavelength of the signal carrier. As shown in Figure 6, $\delta\rho$ can be estimated by:

$$\delta\rho = 2\,h\,sin(e) \qquad (12)$$

where e is the satellite elevation angle, h is the height difference between the phase center of the antennas and sea surface. Let us introduce the variable $x = 2\sin(e)/\lambda$. The interferometric frequency with respect to x denoted by δf_x can be retrieved by:

$$\delta\rho = \lambda\,h\,x$$
$$\delta f_x = \frac{1}{\lambda}\frac{d(\delta\rho)}{dx} = h + x\frac{dh}{dx} = h + x\dot{h}\frac{dt}{dx} \qquad (13)$$

with $\dot{h} = dh/dt$ being the height rate. To account for the height rate in the height retrieval process, we first calculate a sea level estimate using the detected interferometric period (T_{int}) in the LS-HE analysis:

$$P(T_x) = LSHE(x, Y)$$

$$\{P_{max}, T_{int}\} = max[P(T_x)]$$
$$h \approx \delta f_x = \frac{1}{T_{int}} \qquad (14)$$

where $P(T_x)$ is the power spectrum, Y is the matrix of observations, P_{max} is the detected maximum power using the max function. The columns of Y for each scenario include the following time series:

Solution A: $\quad Y = [I_m^2]$

Solution B: $\quad Y = [I_s^R, Q_s^R]$

Solution C: $\quad Y = [I_s^L, Q_s^L]$

Solution D: $\quad Y = [I_s^R, Q_s^R, I_s^L, Q_s^L] \qquad (15)$

with superscript R and L denoting the RHCP and LHCP sea-looking antennas. Having the sea level estimate h from the LS-HE analysis and $\dot{h} = 0$ as the initial value, we find final values of h and $\dot{h}$ through iterative minimization of the following cost function:

$$\min_{h,\dot{h}} \sum_i^N \|\hat{Y}_i - a_i \sin(\frac{4\pi[h + \delta h]\sin(e)}{\lambda} + \phi_i)\| \qquad (16)$$

$$\delta h = \frac{\dot{h}\tan(e)}{\dot{e}} \qquad (17)$$

where δh is a correction term to compensate the height rate effect, $\dot{e}$ is the elevation angle rate, $\hat{Y}_i$ is the i-th observation time series after removing the linear trend, N is the number of observations processed by LS-HE which is 1 in scenario A, 2 in scenarios B and C, and 4 in scenario D, a_i and ϕ_i are the amplitude and phase offset of the interferometric signal in the i-th observation time series that are estimated by least squares analysis.

It should be noted that the side-looking outputs might be contaminated by small phase differences. Two possible causes can be antenna phase center variations [24] and the offset vectors between the master and slave antennas shown in Fig. 6. These effects can introduce low-frequency components to the I/Q outputs. However, at this station these components have much lower frequency compared to the prominent interferometric fringes [37] and would not significantly affect our sea level measurements.

IV. RESULTS AND DISCUSSION

A. Data preparation

The data preparation starts with selecting valid observations which include reflected signals from the sea surface. For this purpose, the precise location of the specular points is estimated within a ray tracing algorithm described by [38] which considers earth surface curvature. A spatial mask using a polygon is then created and applied to the observations to keep the specular points on the sea surface and filter out the reflections from land. To decrease atmospheric effect observations with elevation angles below 5 degrees are excluded. The remaining atmospheric effect is neglected due to the low reflector height. The receiver position is calculated by precise analysis of the direct signals using broadcast ephemerides for the satellite position. The Earth Gravitational Model (EGM96) is used as a reference height. For more information we may refer to [23]. Figure 1-B illustrates the sea-reflected specular points for different GPS satellites used in this study.

B. Applying the LS-HE

For utilizing the LS-HE method, we use a numerical search to catch the dominant interferometric signals in each segment. The step size for searching the interferometric periods is small for the lower periods and gets larger at higher periods using the following recursive formula:

$$T_i = T_{i-1}(1 + \alpha \frac{T_{i-1}}{T_{max}}), \ \alpha = 0.01, \ i = 1, 2, ..., T_i \le T_{max}, \qquad (18)$$

where T_i are the trial periods, T_0 and T_{max} are the minimum and maximum detectable periods in the time window of the segments based on the Nyquist's theorem and the α coefficient allows us to make the initial step bigger and smaller for frequency searching. We assume the covariance matrix is the Identity matrix $Q_y = I$ for each time series.

Figure 7 shows an example outcome of the LS-HE on the time series which is generated from a segment of one event for satellite PRN 26 in L1 and L2 bands. Figure 7-A_1 and B_1 show the I and Q components from each antenna and frequency. Figure 7-A_2 and B_2 depict the results of frequency analysis based on the four scenarios for L1 and L2. As can be recognized from the frequency analysis results in the figure, the highest power of the interferometric period belongs to multivariate analysis of time series of both sea-looking antennas. Slightly lower power can be seen for the time series of the LHCP sea-looking antenna.

C. GNSS-R height retrieval and evaluation

The RMSE values of GNSS-R height estimates from the time series of 31 GPS satellites based on different antenna configurations are summarized in Fig. 8. The heights are estimated using the median of each PRN's observations over a 6-hour window and are compared to tide gauge measurements. The RMSE values shown in this figure are related to individual performance assessments of each satellite. The analysis shows that changing the orientation of the antenna towards the reflecting surface can improve Accuracy. This can be recognized by relatively smaller errors in the estimated heights from the sea-looking RHCP antenna (Fig. 8-A) compared to the up-looking RHCP antenna (Fig. 8-B). The sea-looking LHCP antenna (Fig. 8-C), however, shows a better accuracy compared to the sea-looking RHCP antenna. The fully polarimetric solution, i.e. by the combination of the LHCP and RHCP sea-looking antennas, exhibits the best performance with more consistency between the L1 and L2 measurements and over all the PRNs. Discrepancies in the performance of different PRNs shown in Fig. 8 might be related to various factors including the performance of the antennas in different azimuth angles in terms of phase center variations and antenna gain, as well as satellites Equivalent Isotropically Radiated Power (EIRP) variations. In the next step, we retrieve the final sea level products by combining the observations from all the satellites.

The polarization of the antenna can also affect the GNSS-R height estimation. This can originate from the strength of the reflected signals in different polarizations. The direct GNSS signals with RHCP design will have both RHCP and LHCP components after reflection. The strength of these components can be calculated from Fresnel equations and are functions of the elevation angle of satellites and permittivity of the reflecting surface. The power loss due to reflectivity of seawater at Onsala station [37] suggests that the RHCP component is the dominant component at very low elevation angles. The strengths of the RHCP and LHCP components are almost the same at the elevation angle of about 7 degrees. For higher elevation angles the LHCP component is the predominant part of the signal. Therefore, the LHCP antenna can capture stronger reflections at higher elevation angles. This provides improved performance for retrieving interferometric periods from the LHCP time series (Fig. 8-C). The combination of retrievals from the RHCP and LHCP antennas provide the best performance as can be seen from Fig. 8-D.

Figure 9 presents estimated sea surface height anomalies, using the described method based on the scenarios A, B, C, D. The anomalies are the sea surface heights minus their mean
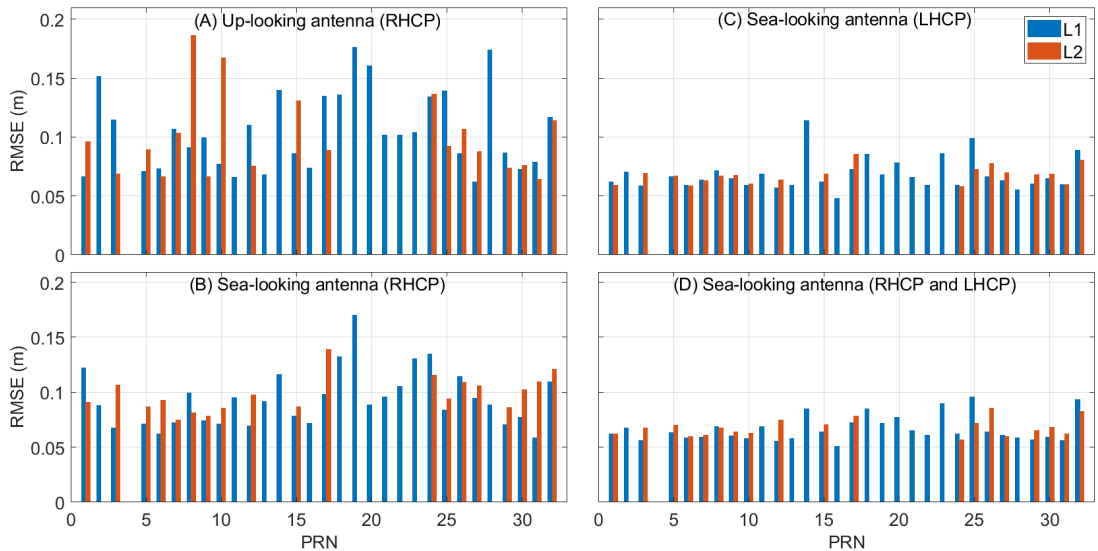
Fig. 8. The Root Mean Squared Error (RMSE) values based on the comparison of GNSS-R sea surface heights with the tide gauge measurements for each GPS Pseudo Random Noise (PRN) numbers from A) up-looking antenna with Right-Handed Circular Polarization (RHCP), B) sea-looking RHCP antenna, C) sea-looking Left-Handed Circular Polarization (LHCP) antenna, and D) combined sea-looking RHCP and LHCP antennas. The red bars are RMSE values of the L2 retrieved heights and the blue bars belong to the L1 retrieved heights. The empty L2 bars are related to the GPS IIR satellites block which do not transmit the L2C signal. The time step and the averaging window for calculating the heights are 5-min and 6-h.

value calculated separately for each solution. The collocated tide gauge measurements are overlaid for comparison. The left panels show the results for the whole dataset (one year) and the right panels illustrate a closer look over a time span of 2 days. As shown in the figure, in all of the four scenarios, the height estimates from the combination of L1 and L2 observations (L12), closely follow the tide gauge measurements. The height retrievals from the L1 observations show almost similar performance compared to L12, although the L1 results from both of the sea-looking antennas show noticeable improvements with respect to the up-looking antenna. The quality of the height measurements from the L2 observations are slightly degraded compared to the L1 and L12 measurements, especially for the RHCP antennas. Considering the fact that not all GPS satellites transmit L2C signal, the lower quality of L2 observations in RHCP antennas can adversely impact the final height retrievals.

We evaluate the final height results using the RMSE values of the GNSS-R measurements with respect to the collocated tide gauge. The correlation values of the GNSS-R and tide gauge measurements are also calculated. Table I shows the RMSE and correlation values based on the described scenarios and four different time windows. The height estimates from the combination of the L1 and L2 observations (L12) provide the best accuracy and robustness. The L12 solution can improve the results up to 25% and 40% compared to the L1 and L2, respectively. The results from L1 observations provide the

closest accuracy with respect to the L12 results. Figure 10 is a visualization of Table I . As seen in the table and figure the best accuracy is achieved with the 6-hour window in the mode of L12 using either LHCP antenna or the combination of the two sea-looking antennas. The results for the combination of the sea-looking antennas in L12 mode is 2.3, 3.0, 4.5, and 5.6 cm for the window size of 6, 3, 1 hour, and 15 minutes.

The overall improvement of the RHCP sea-looking antenna compared to the RHCP up-looking antenna in L2 observations is smaller compared to the L1 results. Despite the fact that the combination of sea-looking RHCP and LHCP antennas for each GPS PRN improves the corresponding accuracy (Fig. 8), the final sea level products from the sea-looking LHCP antenna (Fig. 10-C) shows almost the same performance compared to the combined solution (Fig. 10-D). The earlier inter-comparison study conducted by [16] at another GNSS-R station at Onsala has reported to have an RMSE range of 2.6 to 8.1 cm based on four different SNR-based methods and the window size of 6 to 8 hours. Compared to our study,¨the second GNSS-R station uses a geodetic receiver and an up-looking antenna with approximate height of 4 meters from the sea surface.

Wind speed is one of the parameters which affects the accuracy of the sea surface altimetry due to the change of the sea surface roughness. To assess the impact of wind on the accuracy of the estimated sea surface heights, the data are divided based on the Beaufort wind force scale, which
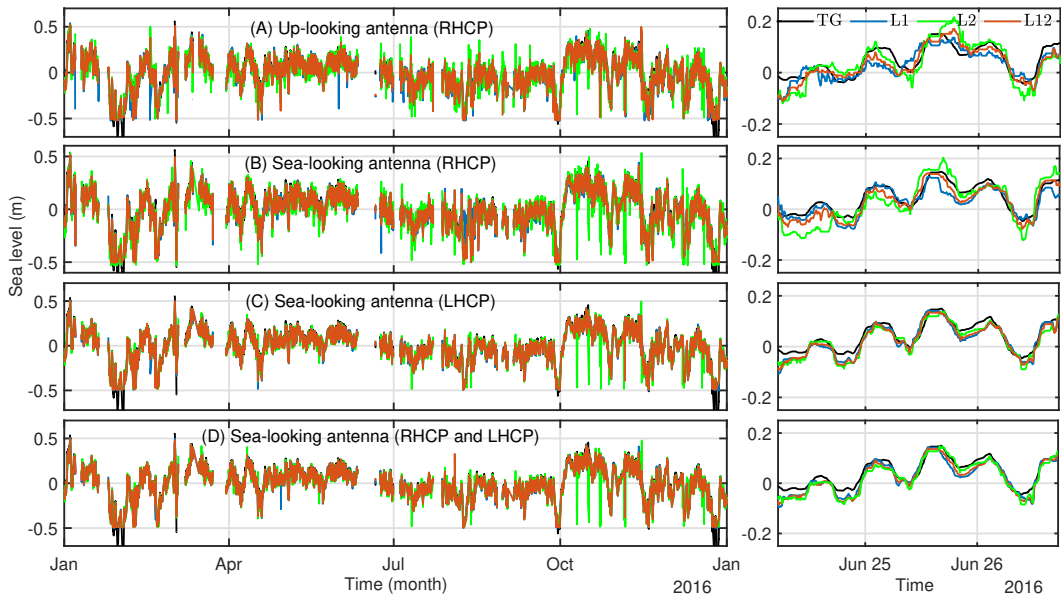
Fig. 9. Time series of sea surface height anomalies derived from GNSS-R observations at Onsala station for the year 2016 (left panels), and closer looks over a period of 2 days (right panels), overlaid on the collocated tide gauge measurements. The height measurements are estimated based on the GNSS-R observations from (A) the up-looking RHCP antenna, (B) the sea-looking RHCP antenna, (C) the sea-looking LHCP antenna, and (D) both sea-looking antennas. The black graph shows the tide gauge measurements, the blue, green, and red colors are the GNSS-R height estimates from the L1, L2, and combined L1 and L2 (L12) sea surface heights. The time step and the averaging window for calculating the heights are 5-min and 6-h.

is an empirical scale related to wind speed and observed conditions at sea or land. The right panels of Fig. 11 show the yearly RMSE values of the retrieved sea surface heights compared with tide gauge in different Beaufort wind force scale for solution C and D. The heights are estimated in 5-min time step and 6-h averaging window. As seen in the figure with the increase of the wind speed the accuracy degrades. This effect is more pronounced in the products related to L2 signals. Overall, the fully-polarimetric solution (D) shows slightly better performance compared to solution C. The left and middle panels of the figure also present the scatter plots of the GNSS-R sea surface height changes compared to the tide gauge sea level variations. As seen in the figure the distribution of the data in L1 and L12 height measurements are better than L2. The L2 sea level results are more sensitive to possible low-quality measurements due to fewer observations from the satellites transmitting L2C signal compared to L1. Generally, the results show excellent agreement with the tide gauge measurements in terms of the correlation and distribution. The solid red and dashed black lines respectively show the fitted linear line and 1:1 ideal correlation. The best agreement is related to L12 retrieved heights.

V. SUMMARY AND CONCLUSION

The study presents the results of sea level measurements using the reflected signals of the Global Navigation Satellite Systems (GNSS) from a coastal experiment at the Onsala Space Observatory in Sweden. The GNSS-Reflectometry (GNSS-R) experiment is equipped with three antennas with different polarizations and orientations. The measurements are calculated based on the application of the Least-Squares Harmonic Estimation method to a dataset of one year over 2016. Based on the flexible configuration of the experiment setup, the effects of polarization, antenna orientation, and the frequency of the GNSS signals are investigated and discussed. The dataset is accompanied by two collocated datasets from the nearest meteorological and tide gauge stations.

Our analysis shows that the best performance can be achieved by a combination of observations from L1 and L2 frequencies (L12) recorded by a sea-looking Left-Handed Circular Polarization (LHCP) antenna. Turning the antenna orientation towards the sea, i.e. a tilt angle of about 90 degrees with respect to the zenith, maximizes the gain of the antenna for capturing the reflections and thus stronger interferometric patterns. The seaward orientation can improve the accuracy of RHCP sea level results up to 20%, 13%, and 25% respectively for L1, L2, and L12. This improvement can reach about 48%, 50% and 47% for L1, L2, and L12 if the tilted antenna

TABLE I: The yearly Root Mean Squared Error (R) and the correlation (C) values of GNSS-R sea surface heights with tide gauge measurements based on four averaging windows, two antenna orientations (up-looking and sea-looking), and two polarizations, i.e. Right- and Left-Handed Circular Polarization (RHCP and LHCP). Subscript A, B, C, and D indicate the results from the up-looking RHCP antenna, sea-looking RHCP antenna, sea-looking LHCP antenna, and combination of both sea-looking antennas, respectively. $L1$, $L2$, and $L12$ respectively represent the sea level results of $L1$, $L2$, and combination of $L1$ and $L2$ height measurements (in the averaging step).

Win = 6 h	L1	L2	L12
R_A (cm)	4.6	5.7	4.1
C_A	0.963	0.943	0.969
R_B (cm)	4.2	5.7	3.1
C_B	0.968	0.948	0.982
R_C (cm)	2.4	3.6	2.4
C_C	0.990	0.977	0.990
R_D (cm)	2.4	3.8	2.3
C_D	0.990	0.973	0.990
Win = 3 h			
R_A (cm)	6.1	7.8	5.7
C_A	0.940	0.901	0.946
R_B (cm)	5.3	7.1	4.4
C_B	0.951	0.923	0.967
R_C (cm)	3.2	4.0	3.0
C_C	0.982	0.972	0.984
R_D (cm)	3.1	4.2	3.0
C_D	0.983	0.970	0.984
Win = 1 h			
R_A (cm)	8.6	10.4	8.14
C_A	0.893	0.847	0.901
R_B (cm)	7.4	9.1	6.6
C_B	0.912	0.884	0.930
R_C (cm)	4.7	5.3	4.5
C_C	0.964	0.954	0.967
R_D (cm)	4.6	5.4	4.5
C_D	0.965	0.952	0.967
Win = 15 min			
R_A (cm)	11.7	12.1	10.3
C_A	0.827	0.811	0.854
R_B (cm)	9.3	10.9	8.7
C_B	0.870	0.846	0.886
R_C (cm)	5.8	6.4	5.6
C_C	0.946	0.935	0.949
R_D (cm)	5.6	6.3	5.6
C_D	0.948	0.837	0.949
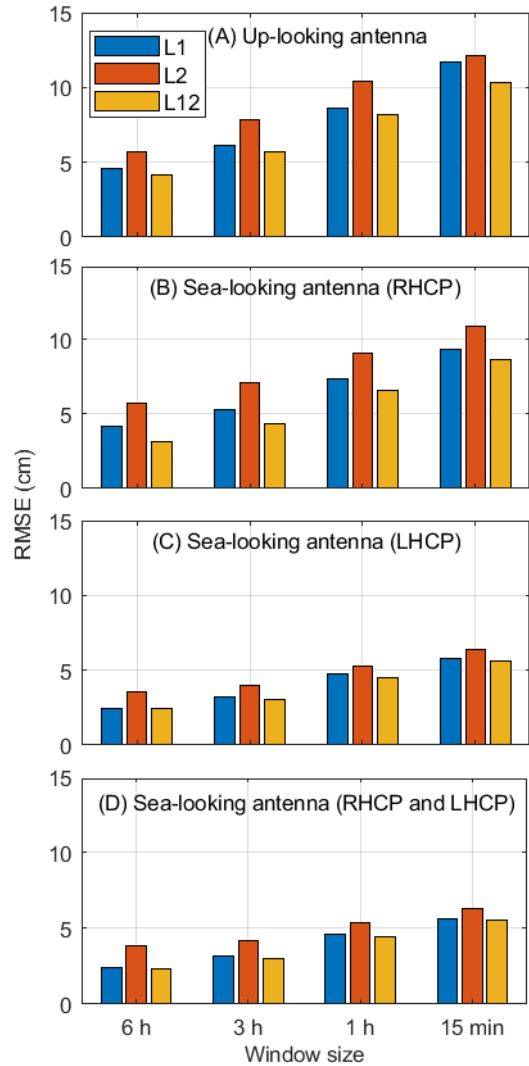
Fig. 10. The annual RMSE values of the GNSS-R sea surface height with respect to the tide gauge measurements for up-looking and sea-looking antennas in four types of window size to average sea surface heights.

is LHCP. The accuracy supremacy of LHCP measurements compared to the RHCP measurements can be attributed to the stronger reflections from the seawater at LHCP. Except for very low elevation angles, the LHCP component of the reflected signals is the dominant part. Therefore, while the RHCP antenna is an appropriate option for grazing angles

Fig. 11. The left and middle panels illustrate the scatter plots of the GNSS-R height anomalies and tide gauge height anomalies with respect to the wind speed. The graphs are related to the solutions C and D for L1, L2, and the combination of them (L12). The time step and the averaging window for calculating the heights are 5-min and 6-h. The fitted line and 1:1 ideal correlation are shown by the solid r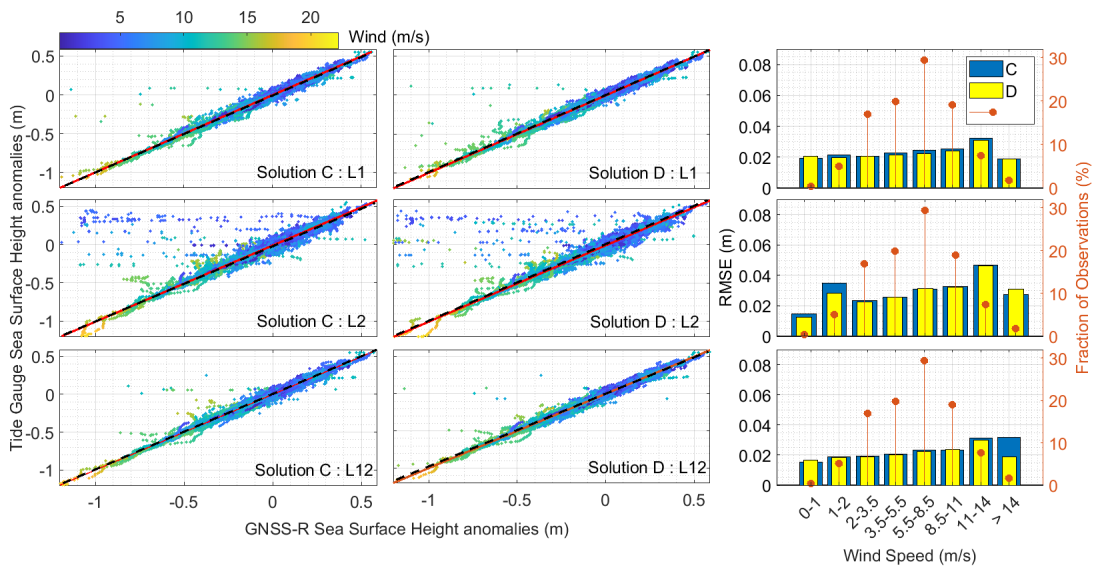ed line and dashed black line, respectively. The right panels show the RMSE values between the obtained GNSS-R heights and tide gauge measurements overlaid by the fraction of the data in red bars.

altimetry, using a LHCP antenna would be inevitable for higher elevation angles.

The effects of using L1 or L2 carrier frequencies are also investigated. The results from L2 frequency generally show a lower degree of accuracy most likely because of fewer observations (as not all satellites transmit L2C). We combined the L2 sea level products with the L1 products to form L12 measurements for robustness and enhancement. The size of the averaging window also is one of the parameters that affect the accuracy of final products. Longer averaging window improves the quality of the results. The Root Mean Square Error (RMSE) between GNSS-R sea surface heights for LHCP sea-looking antenna with respect to collocated tide gauge measurements are 2.4, 3.0, 4.5, and 5.6 cm for 6, 3, 1, and 0.25-hour window size, respectively.

The investigation of wind effect on the accuracy of GNSS-R sea level measurements reports a lower degree of accuracy during higher wind speeds. The RMSE value of the products can be two times larger in wind speeds above 11 m/s compared to calm sea surface during wind speeds below 2 m/s. However, the final L12 sea level estimates show a remarkable tolerance against high wind speeds, especially for the combined fully-polarimetric solution. The multivariate formulation of the method used in this study shows to be a promising tool for multi-frequency multi-constellation GNSS-R altimetry.

ACKNOWLEDGMENT

REFERENCES

[1] K. O. Emery and D. G. Aubrey, *Sea levels, land levels, and tide gauges*. Springer Science & Business Media, 2012, ISBN: 978-1-4613-9101-2.

[2] M. Fernandes, L. Bastos, and M. Antunes, "Coastal satellite altimetry–methods for data recovery and validation," in *3rd meeting of the international gravity and geoid commission "Gravity and Geoid*. Citeseer, 2002, pp. 26–30.

[3] Martin-Neira, "A passive reflectometry and interferometry system (PARIS): Application to ocean altimetry," *ESA journal*, vol. 17, no. 4, pp. 331–355, 1993.

[4] O. Germain, G. Ruffini, F. Soulat, M. Caparrini, B. Chapron, and P. Silvestrin, "The eddy experiment: Gnss-r speculometry for directional sea-roughness retrieval from low altitude aircraft," *Geophysical research letters*, vol. 31, no. 21, 2004.

[5] M. Hoseini, M. Asgarimehr, V. Zavorotny, H. Nahavandchi, C. Ruf, and J. Wickert, "First evidence of mesoscale ocean eddies signature in GNSS reflectometry measurements," *Remote Sensing*, vol. 12, no. 3, p. 542, 2020.

[6] F. Fabra, E. Cardellach, O. Nogués-Correig, S. Oliveras, S. Ribo, A. Rius, M. Belmonte-Rivas, M. Semmling, G. Macelloni, S. Pettinato *et al.*, "Monitoring sea-ice and dry snow with GNSS reflections," in *2010 IEEE international geoscience and remote sensing symposium*. IEEE, 2010, pp. 3837–3840.

[7] M. Rajabi, H. Nahavandchi, and M. Hoseini, "Evaluation of CYGNSS Observations for Flood Detection and Mapping during Sistan and Baluchestan Torrential Rain in 2020," *Water*, vol. 12, no. 7, p. 2047, 2020.

[8] M. Asgarimehr, M. Hoseini, M. Semmling, M. Ramatschi, A. Camps, H. Nahavandchi, R. Haas, and J. Wickert, "Remote Sensing of Precipitation Using Reflected GNSS Signals: Response Analysis of Polarimetric Observations," *IEEE Transactions on Geoscience and Remote Sensing*, pp. 1–12, 2021.

[9] G. Foti, C. Gommenginger, and M. Srokosz, "First Spaceborne GNSS-Reflectometry Observations of Hurricanes From the UK TechDemoSat-1 mission," *Geophysical Research Letters*, vol. 44, no. 24, pp. 12–358, 2017.

[10] K. D. Anderson, "Determination of water level and tides using interferometric observations of GPS signals,"

Journal of Atmospheric and Oceanic Technology, vol. 17, no. 8, pp. 1118–1127, 2000.

[11] F. Soulat, M. Caparrini, O. Germain, P. Lopez-Dekker, M. Taani, and G. Ruffini, "Sea state monitoring using coastal GNSS-R," *Geophysical Research Letters*, vol. 31, no. 21, 2004.

[12] J. Löfgren, R. Haas, H.-G. Scherneck, and M. Bos, "Three months of local sea level derived from reflected GNSS signals," *Radio Science*, vol. 46, no. 6, 2011.

[13] J. S. Löfgren and R. Haas, "Sea level measurements using multi-frequency GPS and GLONASS observations," *EURASIP Journal on Advances in Signal Processing*, vol. 2014, no. 1, pp. 1–13, 2014.

[14] J. Strandberg, T. Hobiger, and R. Haas, "Improving GNSS-R sea level determination through inverse modeling of SNR data," *Radio Science*, vol. 51, no. 8, pp. 1286–1296, 2016.

[15] K. M. Larson, R. D. Ray, and S. D. Williams, "A 10-year comparison of water levels measured with a geodetic GPS receiver versus a conventional tide gauge," *Journal of Atmospheric and Oceanic Technology*, vol. 34, no. 2, pp. 295–307, 2017.

[16] F. Geremia-Nievinski, T. Hobiger, R. Haas, W. Liu, J. Strandberg, S. Tabibi, S. Vey, J. Wickert, and S. Williams, "SNR-based GNSS reflectometry for coastal sea-level altimetry: results from the first IAG intercomparison campaign," *Journal of Geodesy*, vol. 94, no. 8, pp. 1–15, 2020.

[17] S. Tabibi, F. Geremia-Nievinski, O. Francis, and T. van Dam, "Tidal analysis of GNSS reflectometry applied for coastal sea level sensing in antarctica and greenland," *Remote Sensing of Environment*, vol. 248, p. 111959, 2020.

[18] A. Santamaría-Gómez and C. Watson, "Remote leveling of tide gauges using GNSS reflectometry: case study at

Spring Bay, Australia," *GPS solutions*, vol. 21, no. 2, pp. 451–459, 2017.

[19] A. Padokhin, G. Kurbatov, M. Nazarenko, and V. Smolov, "GNSS Reflectometry of the Black Sea level in the experiments at the Stationary Oceanographic Platform," *Moscow University Physics Bulletin*, vol. 73, no. 4, pp. 422–427, 2018.

[20] A. Alonso-Arroyo, A. Camps, H. Park, D. Pascual, R. Onrubia, and F. Martín, "Retrieval of significant wave height and mean sea surface level using the GNSS-R interference pattern technique: Results from a three-month field campaign," *IEEE Transactions on Geoscience and Remote Sensing*, vol. 53, no. 6, pp. 3198–3209, 2014.

[21] N. Rodriguez-Alvarez, X. Bosch-Lluis, A. Camps, I. Ramos-Perez, E. Valencia, H. Park, and M. Vall-Llossera, "Water level monitoring using the interference pattern GNSS-R technique," in *2011 IEEE International Geoscience and Remote Sensing Symposium*. IEEE, 2011, pp. 2334–2337.

[22] W. Hongguang, K. Shifeng, and Z. Qinglin, "A model for remote sensing sea level with GPS interferometric signals using RHCP antenna," in *ISAPE2012*. IEEE, 2012, pp. 624–626.

[23] A. M. Semmling, G. Beyerle, R. Stosius, G. Dick, J. Wickert, F. Fabra, E. Cardellach, S. Ribó, A. Rius, A. Helm *et al.*, "Detection of Arctic ocean tides using interferometric GNSS-R signals," *Geophysical Research Letters*, vol. 38, no. 4, 2011.

[24] W. Liu, J. Beckheinrich, M. Semmling, M. Ramatschi, S. Vey, J. Wickert, T. Hobiger, and R. Haas, "Coastal sea-level measurements based on GNSS-R phase altimetry: A case study at the Onsala Space Observatory, Sweden," *IEEE Transactions on Geoscience and Remote Sensing*, vol. 55, no. 10, pp. 5625–5636, 2017.

[25] F. Fabra, E. Cardellach, A. Rius, S. Ribó, S. Oliveras, O. Nogués-Correig, M. B. Rivas, M. Semmling, and S. D'Addio, "Phase altimetry with dual polarization GNSS-R over sea ice," *IEEE Transactions on Geoscience and Remote Sensing*, vol. 50, no. 6, pp. 2112–2121, 2011.

[26] L. Bao, N. Wang, and F. Gao, "Improvement of Data Precision and Spatial Resolution of cGNSS-R Altimetry Using Improved Device With External Atomic Clock," *IEEE Geoscience and Remote Sensing Letters*, vol. 13, no. 2, pp. 207–211, 2015.

[27] A. R. Amiri-Simkooei, C. C. Tiberius, and P. J. Teunissen, "Assessment of noise in GPS coordinate time series: methodology and results," *Journal of Geophysical Research: Solid Earth*, vol. 112, no. B7, 2007.

[28] A. M. Semmling, A. Rösel, D. V. Divine, S. Gerland, G. Stienne, S. Reboul, M. Ludwig, J. Wickert, and H. Schuh, "Sea-ice concentration derived from GNSS reflection measurements in Fram Strait," *IEEE Transactions on Geoscience and Remote Sensing*, vol. 57, no. 12, pp. 10 350–10 361, 2019.

[29] M. Semmling, "Altimetric monitoring of Disko Bay using interferometric GNSS observations on L1 and L2," Ph.D. dissertation, Deutsches GeoForschungsZentrum GFZ Potsdam, 2012.

[30] K. M. Larson, E. E. Small, E. Gutmann, A. Bilich, P. Axelrad, and J. Braun, "Using GPS multipath to measure soil moisture fluctuations: initial results," *GPS solutions*, vol. 12, no. 3, pp. 173–177, 2008.

[31] M. Rajabi, A. Amiri-Simkooei, H. Nahavandchi, and V. Nafisi, "Modeling and prediction of regular ionospheric variations and deterministic anomalies," *Remote Sensing*, vol. 12, no. 6, p. 936, 2020.

[32] P. Vaníček, "Further development and properties of the spectral analysis by least-squares," *Astrophysics and Space Science*, vol. 12, no. 1, pp. 10–33, 1971.

[33] N. R. Lomb, "Least-squares frequency analysis of un-

equally spaced data," *Astrophysics and space science*, vol. 39, no. 2, pp. 447–462, 1976.

[34] J. D. Scargle, "Studies in astronomical time series analysis. II-Statistical aspects of spectral analysis of unevenly spaced data," *The Astrophysical Journal*, vol. 263, pp. 835–853, 1982.

[35] Y. Ghiasi, C. R. Duguay, J. Murfitt, J. J. van der Sanden, A. Thompson, H. Drouin, and C. Prévost, "Application of gnss interferometric reflectometry for the estimation of lake ice thickness," *Remote Sensing*, vol. 12, no. 17, p. 2721, 2020.

[36] A. Amiri-Simkooei, "On the nature of GPS draconitic year periodic pattern in multivariate position time series," *Journal of Geophysical Research: Solid Earth*, vol. 118, no. 5, pp. 2500–2511, 2013.

[37] M. Hoseini, M. Semmling, H. Nahavandchi, E. Renn-spiess, M. Ramatschi, R. Haas, J. Strandberg, and J. Wickert, "On the Response of Polarimetric GNSS-Reflectometry to Sea Surface Roughness," *IEEE Transactions on Geoscience and Remote Sensing*, 2020.

[38] A. M. Semmling, V. Leister, J. Saynisch, F. Zus, S. Heise, and J. Wickert, "A phase-altimetric simulator: Studying the sensitivity of Earth-reflected GNSS signals to ocean topography," *IEEE Transactions on Geoscience and Remote Sensing*, vol. 54, no. 11, pp. 6791–6802, 2016.

Mahmoud Rajabi graduated in Geodesy and geomatics from the University of Isfahan, Iran. He is currently PhD student at the Norwegian University of Science and Technology (NTNU). His research interests include atmospheric, ocean and land Remote Sensing using Mono- and Bi-static radar systems. His current research focuses on the monitoring of the ocean and land using both ground-based and space-borne GNSS-Reflectometry .

Markus Ramatschi received the Dipl.-rer. nat. in geophysics and the Ph.D. degree in geophysics from the Technical University of Clausthal, Clausthal-Zellerfeld, Germany, in 1992 and 1998, respectively. He is currently a Senior Scientist at the German Research Centre for Geosciences (GFZ), Potsdam, Germany. His research interests include the operation of a global GNSS sensor station network.

Mostafa Hoseini Mostafa Hoseini graduated in geodesy from the University of Tehran, Tehran, Iran. He has worked for several institutions as a GNSS Engineer in the field of positioning and navigation. Before starting his Ph.D. studies in 2018 at the Norwegian University of Science and Technology (NTNU), Trondheim, Norway, he worked on the analysis of GNSS atmospheric products at the German Research Centre for Geosciences (GFZ), Potsdam, Germany. His research interest includes GNSS-based sensors and techniques for remote sensing applications. His research interest also includes the monitoring of the ocean and Arctic using GNSS-Reflectometry onboard CubeSats. .

Mehdi Goli is an assistant professor of geodesy at the Faculty of Civil and Architectural Engineering, Shahrood University of Technology, Iran. He received his PhD degrees in geodesy from K. N. Toosi University of Technology, Iran. His research interests focus on space geodesy and geoid determination methods.

Hossein Nahavandchi received the Ph.D. degree from the Royal Institute of Technology (KTH), Stockholm, Sweden in 1998. He is currently a Professor of Geodesy and Geophysics with the Norwegian University of Science and Technology (NTNU), Trondheim, Norway. His research interests involve Global Geodetic Observations System (GGOS) including satellite gravimetry, satellite altimetry, satellite radar interferometry and GNSS to understand the dynamic Earth system by quantifying Earth's change in space and time.

Rüdiger Haas is a full professor for space geodesy at the Department of Space, Earth and Environment at Chalmers University of Technology, Sweden. He received his MSc and his PhD degrees in geodesy from Bonn University, Germany. He is the head of the research group for space geodesy at Chalmers and responsible for the geoscience activities at the Onsala Space Observatory. His research interests focus primarily on space geodetic techniques, such as Global Navigation Satellite Systems (GNSS), including GNSS reflectometry, and Very Long Basline Interferometry (VLBI).

Maximilian Semmling graduated in physics from Leipzig University, Leipzig, Germany, in 2007. He received the Ph.D. degree from Technische Universität Berlin, Berlin, Germany, in 2012. For his doctoral and post-doctoral studies, he was with the German Research Centre for Geosciences (GFZ), Potsdam, Germany, the Institute for Space Studies of Catalonia (IEEC), Barcelona, Spain, and the University of the Littoral Opal Coast (ULCO), Dunkirk, France. In 2020, he joined the Observation Department, German Aerospace Center (DLR), Institute for Solar-Terrestrial Physics, Neustrelitz, Germany. He is experienced in GNSS for Earth observation with a research focus on ocean altimetry and sea ice remote sensing. His work concentrates on the influence of atmosphere and space weather. Corresponding methods cover a wide range from ground-based measurements over maritime, and airborne to satellite platforms..

Jens Wickert received the graduate degree in physics from the Technical University Dresden, Germany, in 1989, and the Ph.D.degree in geophysics/meteorology from the Karl-Franzens-University Graz, Austria, in 2002. He currently holds a joint professorship of GFZ with the Technical University of Berlin on GNSS remote sensing, navigation and positioning. He is also the Deputy GFZ Section Head Space Geodetic Techniques and the GFZ Research Topic Director "The Atmosphere in Global Change". He has authored/co-authored around 250 ISI listed publications on GNSS Earth observation. He was Principal Investigator of the pioneering GPS radio occultation experiment aboard the German CHAMP satellite and coordinates numerous research projects on GNSS remote sensing.

ORIGINAL ARTICLE

Tidal harmonics retrieval using GNSS-R dual-frequency complex observations

Mahmoud Rajabi[1] [ORCID] · **Mostafa Hoseini[1]** · **Hossein Nahavandchi[1]** · **Milad Asgarimehr[2]** · **Maximilian Semmling[3]** · **Markus Ramatschi[4]** · **Mehdi Goli[5]** · **Jens Wickert[4,6]**

Abstract

Tidal analysis and methods for estimation and prediction of ocean tidal constitutes are essential in a large area of scientific disciplines, for example, navigation, onshore and offshore engineering, and production of green energy. Ground-based Global Navigation Satellite System-Reflectometry (GNSS-R) has been proposed as an alternative method for measuring sea surface height. We use 6 years of GNSS-R observations at In-phase and Quadrature levels from July 2015 to May 2021 obtained from a dedicated receiver and sea-looking left hand circular polarization antenna for estimating sea level (SL). In the first step, the multivariate least-square harmonic estimation (LS-HE) method is applied for SL estimation. Then, final SL time series are generated by combining estimated SL from all satellites at L1 and L2 frequencies in the averaging step. The 6-year root-mean-square error between GNSS-R L12 sea surface heights and a collocated tide gauge (TG) is 5.8 cm with a correlation of 0.948 for a high temporal resolution of 5 min with 15 min averaging window. Afterward, using the univariate LS-HE, we detect tidal harmonics with periods between 30 min to 1 year. The detection results highlight a good match between GNSS-R and TG. Higher harmonics, i.e., the periods shorter than 3 h, show stronger signatures in GNSS-R data. Finally, we estimate the amplitude and phase of standard tidal harmonics from the two datasets. The results show an overall good agreement between the datasets with a few exceptions.

1 Introduction

Tides are periodic fluctuations of the sea level due to astronomical objects, for example, sun, moon, and earth rotation

Mahmoud Rajabi
mahmoud.rajabi@ntnu.no

1. Civil and Environmental Engineering, Norwegian University of Science and Technology, 7491 Trondheim, Norway

2. German Research Centre for Geosciences (GFZ), 14473 Potsdam, Germany

3. German Aerospace Center DLR, Institute for Solar-Terrestrial Physics, Neustrelitz, Germany

4. Department of Geodesy, German Research Center for Geosciences (GFZ), 14473 Potsdam, Germany

5. Faculty of Civil and Architectural Engineering, Shahrood University of Technology, Shahrood, Iran

6. The Institute of Geodesy and Geoinformation Science, Technische Universität, Berlin, Germany

gravity effects (Doodson 1954; Shum et al. 2001; Devlin 2016). Knowledge of the tide is essential for safe ship navigation, coastal engineering, marine pollution management, surveying engineering, marine tourism, and commercial and recreational fishermen. Moreover, tidal energy is on its way to being one of the important sources of clean, reliable, and sustainable energy (Rourke et al. 2010). Sea level has long been an essential parameter for numerous coastal and offshore services, for example, defining national reference level systems, easing port operation, security, and safety, facilitating navigation, and as an important index of climate changes (Adebisi et al. 2021). Besides tide gauge as the main method for sea-level monitoring, satellite altimetry, and Global Navigation Satellite Systems Reflectometry (GNSS-R) have also been used. The history of using tide poles goes back to the 1770s (Church and White 2011). Tide gauges measure sea level, relative to a local geodetic monument as a reference level. Although tide gauges can obtain precise relative sea level, there are some limitations and challenges, for exam-

ple, vertical land movement (Cipollini et al. 2017), stability of the area, and connecting the relative sea level to a global reference frame. The limitation of satellite altimetry lies primarily in its low repeat period, limiting its ability to capture rapid changes in ocean dynamics. Additionally, it is often restricted in its use near coastlines due to contamination from land reflections. (Marti et al. 2019).

The utilization of the Global Navigation Satellite Systems (GNSS) for remote sensing (GNSS-RS) purposes has been gaining in popularity in recent decades besides its primary services (timing, navigation, and positioning). Over 100 GNSS satellites, including GPS, Galileo, GLONASS, and BeiDou/Compass, transmit navigation signals. The signal generated by these satellites which pass through the atmosphere can contribute information about the atmospheric layers and their variability (Rajabi et al. 2020a, 2015). Reflected GNSS signals from land or oceans in a bi-static geometry provide an opportunity to study different parameters of the reflecting surfaces for natural hazards and environmental monitoring applications such as sea level (Martin-Neira 1993), sea surface roughness (Hoseini et al. 2020b), ocean eddies (Hoseini et al. 2020a), sea ice concentration (Semmling et al. 2019), flood (Rajabi et al. 2020b), precipitation (Asgarimehr et al. 2021), wind speed (Foti et al. 2017), snow depth (Tabibi 2016), river water height (Zeiger et al. 2021), and storm detection (Vu et al. 2019). This innovative technique represents a significant advancement in remote sensing, as it utilizes passive sensors that can operate effectively in ground-based, airborne, and space-borne modes (Zavorotny et al. 2014).

Ground-based GNSS-R as a multi-purpose sensor has been introduced as an alternative option for traditional tide gauges over the past decades. Compared to the tide gauges, this sensor is easier to install, covers a wider area, gives sea surface height in a global height coordinate system, is capable of correcting the station's vertical displacement, and can deliver extra information such as sea surface roughness and ice coverage. The conceptualization of sea level retrieval using GNSS-R was proposed in 1993 (Martin-Neira 1993) and used for ground-based GNSS-R stations signals in 2000 (Anderson 2000). Several studies have assessed the performance of the GNSS-R heights time series for tidal constituents analysis.

Semmling et al. (2012) used a 60-day GNSS-R height time series at Godhavn to detect diurnal (K_1) and semi-diurnal (M_2, S_2) constituents with decimeter range. Löfgren et al. (2014) presented sea-level measurements retrieved from the analysis of signal-to-noise ratio (SNR) data recorded by five coastal geodetic GPS stations. They showed that the harmonic analysis of the residuals reveals remaining signal power at multiples of the GPS draconitic day. Furthermore, they illustrated that the observed SNR data were, to some level, disturbed by additional multi-path signals, in partic-

ular for GPS stations that are located in harbors. Larson et al. (2017) used 10 years of L1 SNR GPS data at Friday Harbor and found an RMSE of 12 cm from individual satellite passes. They showed that the tidal component (between S_a and M_6) retrieved from both the GNSS-R and tide gauge time series was in good agreement with the absolute differences of up to 1 cm in case of amplitudes. Tabibi et al. (2020) showed there is a millimetric agreement between SNR-based GNSS-R height and the tide gauge observation for eight major tidal components, except lunisolar diurnal (K_1), principal solar (S_2), and lunisolar semi-diurnal (K_2) components. They stated that differences were due to leakage from the GPS orbital period. Gravalon et al. (2022) used SNR-based GNSS-R at four stations and noticed an error in the $K1/K2$ tidal constituents. Geremia-Nievinski et al. (2020) utilized 1 year of SNR data for the GPS L1-C/A signal collected at the Onsala Space Observatory and compared the performance of the methods developed by four research groups. They concluded that all four groups captured semi-diurnal and diurnal variations and most GNSS-R solutions showed harmonics at integer fractions of one sidereal day.

In most of the GNSS-R studies, the tidal harmonics with periods shorter than 3 h (higher harmonics) are poorly represented due to the low temporal resolution of the measurements (Geremia-Nievinski et al. 2020). The studies predominantly utilized L1 SNR observations from geodetic receivers. This study uses around 6 years of In-phase and Quadrature (I/Q) datasets collected by multi-front-end dedicated GNSS-R receiver located in the Onsala Space Observatory. We evaluate the effect of using more observations at lower level, i.e., direct I/Q outputs, to retrieve SL variations. The final SL is the result of a combination of L1 and L2 generated height using a Left-Handed Circular Polarization (LHCP) antenna for detecting and analyzing the tidal harmonics. We estimate the SL using a 15-minute averaging window (near real-time and combined SL product) to increase time resolution. The rest of this paper is organized as follows. The study area and dataset are presented in Sect. 2. The methodology and mathematical concepts are described in Sect. 3. The discussion of data processing and the results are explained in Sect. 4. Finally, the paper is finalized by a conclusion in Sect. 5.

2 Data

2.1 GNSS-R site and dataset

We use just under 6 years of GNSS-R data from July 2015 to May 2021 obtained from a dedicated GNSS-R site mounted and operated by the German Research Center for Geosciences (GFZ) together with Onsala Space Observatory in Sweden (57.393° N, 11.914° E). The experiment uses multi-

ple antennas installed on a concrete structure with a height of about 3 m from the sea surface. The station has three types of antennas, one is zenith-looking and the two others are tilted toward the sea with the angle of 98° relative to the zenith. The zenith-looking antenna is RHCP and is assigned to track direct GPS signals. The sea-looking antennas with RHCP and LHCP can effectively acquire reflected GPS signals at two different polarizations with the highest antenna gain values of up to 4.7 dB. A GNSS occultation, reflectometry, and scatterometry (GORS) receiver (Rajabi et al. 2021a; Helm et al. 2007) with four antenna inputs is used in the GNSS-R site. The receiver can only process GPS L1 and L2 signals. The first input is utilized for the master channel and is linked to the up-looking antenna. The second and third inputs are dedicated to the slave channels and are connected to the sea-looking antennas.

Based on our previous study (Rajabi et al. 2022), the best performance for the altimetry can be achieved using the LHCP antenna. Therefore, we just use the data output of the LHCP link. To select valid observations which include reflected signals from the sea surface, the location of the specular points is calculated via a ray-tracing algorithm described by Semmling et al. (2016) concerning the earth's surface curvature. Afterward, we select the reflections from the sea surface using a polygon mask. The observations with elevation angles between 5° and 30° are selected for the investigation. The I/Q data with elevation angles below 5° are excluded to reduce the atmospheric effect and the rest of the effect is considered negligible because of the low reflector height. However, the atmospheric effect could introduce a small-scale error proportional to the reflector height (Williams and Nievinski 2017). As will be presented in the results section, the retrieved amplitudes from GNSS-R and the tide gauge show very close correspondence, highlighting a minimal atmospheric effect.

Figure 1a, b shows the GNSS-R experiment setup from the top view and the antenna installation setup. The data suffer from some gaps accounting for about 21% of the whole data. Although the method used in this study can handle datasets with gaps, the presence of missing values in the analyzed GNSS-R dataset can leave its signature on the accuracy of the results. In order to create the same situation for both datasets in the analysis, we utilize tide gauge measurements only at the epochs when GNSS-R data is available.

2.2 Tide gauge measurements

The dataset used in this study includes ancillary sea-level measurements from a nearby tide gauge located about 300 m away from our GNSS-R experiment setup (Fig. 1a). The tide gauge (Fig. 1c) was developed and constructed in-house, with advice from the Swedish Meteorological and Hydrological Institute (SMHI). The official tide gauge sta-
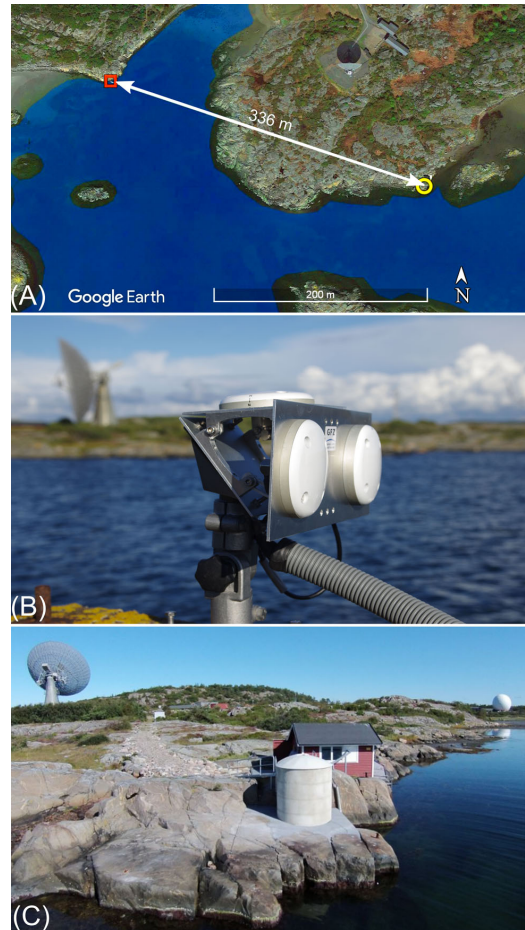
Fig. 1 **a** The red square and yellow circle represent the GNSS-R experiment setup and the tide gauge station from the top view, respectively, **b** the GNSS-R station antenna configuration, **c** the tide gauge station located in Onsala Space Observatory

tion consists of several sensors, and the main sensor is the Campbell CS476 radar with an 8° beam angle and millimeter-level accuracy. The data are open access through the SMHI website (https://www.smhi.se/kunskapsbanken/oceanografi/tide-gauge-onsala-1.94732).

3 Method

This study consists of three main stages (Fig. 2). The first stage is the data preparation through the time series associated with each reflection event. In the second stage, we focus on finding the interferometric frequency in the I/Q
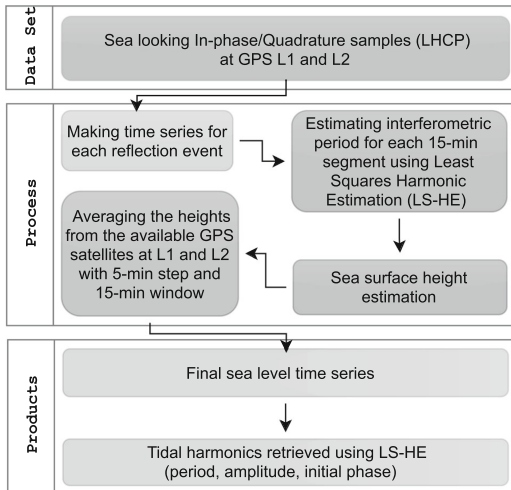
Fig. 2 A schematic diagram of methodology based on the univariate and multivariate least-squares harmonic estimation (LS-HE) method

observations using multivariate least-squares harmonic estimation (LS-HE) for the LHCP antenna. Then, we calculate the sea surface heights based on the retrieved interferometric frequency from L1 and L2 observations. To combine the estimated sea surface heights from different satellites, we use an averaging window of 15 min for every 5 min time step. Overall, each height measurement is based on up to eight reflection events from one to four satellites at L1 and L2 frequencies satellites reflection. We use a native MATLAB function for outlier detection based on the median absolute deviation (MAD) values. All the values beyond three scaled MAD with respect to the median are considered as outliers. To suppress the effect of any remaining outliers, the median value of the estimates within the averaging window is considered as the final height estimate. The last stage of the methodology is the validation of the GNSS-R height estimates with the collocated tide gauge observations and detecting the tidal harmonics for both datasets, and comparing them in terms of amplitudes, period, and initial phases.

3.1 GNSS-R height estimation

The interference of a reflected signal with the direct signal generates a compound signal. The SNR of the compound signal fluctuates due to the constructive or destructive phases of the direct and reflected signals. This oscillation is known as interference pattern and can be used to retrieve different information from the reflecting surface. Here, we aim to retrieve sea-level variations from the interference patterns. The geometry of reflection affects the frequency of the oscillation. Therefore, the main observation used in this study is

the interferometric frequency. We apply the LS-HE method to I/Q observations to effectively detect this frequency. The method uses individual linear terms for the I/Q time series. The linear terms can compensate the effect of the direct signal on the time series variations. Therefore, the LS-HE can separate the contributions of the direct signal from the interferometric fringes. The interferometric period are then inverted to the reflector height, i.e., the height between the phase center of the receiving antenna and the reflecting surface. The details of this procedure are given in (Rajabi et al. 2022).

The reflected signals travel an excess path to reach the antenna. The path difference between the direct and reflected signals ($\delta\rho$) changes over time which creates a Doppler frequency shift (δf) that characterizes the interferometric pattern's frequency (Hoseini et al. 2020b):

$$\delta f = \frac{1}{\lambda} \frac{d(\delta\rho)}{dt} \tag{1}$$

where λ is the carrier signal's wavelength. We use the period of interferometric oscillations to calculate the sea surface height. As shown in Fig. 3, $\delta\rho$ can be estimated by:

$$\delta\rho = 2\,h\,\sin(e) \tag{2}$$

with e being the satellite elevation angle, h the height difference between the sea surface and the antenna phase center. The variable $x = 2\sin(e)/\lambda$ is used here to simplify the calculations. The frequency of interferometric fringes in terms of the variable x is shown by δf_x and can be formulated as:

$$\delta\rho = \lambda\,h\,x$$
$$\delta f_x = \frac{1}{\lambda} \frac{d(\delta\rho)}{dx} = h + x\frac{dh}{dx} = h + x\,\dot{h}\frac{dt}{dx} \tag{3}$$

where $\dot{h} = dh/dt$ is the rate of change for the reflector height. We apply an iterative process to simultaneously estimate the effect of height rate and retrieve accurate reflector height. In doing so, we first apply LS-HE method denoted by $\mathcal{L}$ to the I/Q samples of the LHCP slave antenna with respect to x:
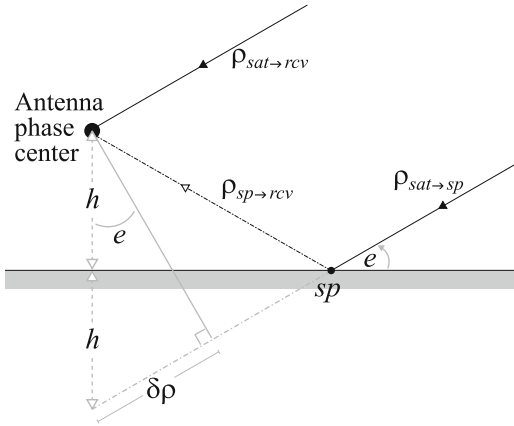
$$P(T_x) = \mathcal{L}(x, Y)$$
$$Y = [I_s^L, Q_s^L]$$
$$\{P_{\max}, T_{\text{int}}\} = \max[P(T_x)]$$
$$h \approx \delta f_x = \frac{1}{T_{\text{int}}} \tag{4}$$

where $P(T_x)$ is the output of LS-HE spectral analysis, which is a power spectrum against different periods, Y is the matrix of I/Q time series. The superscript ^{L} is used to refer to the LHCP polarization of the slave antenna denoted by the subscript $_s$. The function max detects the maximum power and

Fig. 3 The path difference between the direct and reflected signals in a ground-based reflectometry experiment with low reflector height. ρ_{sat-sp} is the distance between the satellite and specular point, $\rho_{sat-rec}$ is the distance between the satellite and receiver antenna, ρ_{sp-rec} is the distance between the specular point and receiver antenna, e is the satellite elevation angle, $\delta\rho$ is the extra path of the reflected signal compared to the direct signal, and h is the height difference between the phase center of the antenna and sea surface

returns the corresponding period, which is the period of interferometric pattern (T_{int}). The iterative process to find the accurate reflector height starts with the assumption $\dot{h} = 0$. The values of h and $\dot{h}$ are calculated within the following minimization problem (Rajabi et al. 2022):

$$\min_{h,\dot{h}} \sum_i^2 \left\| \hat{Y}_i - a_i \sin\left(\frac{4\pi[h + \delta h]\sin(e)}{\lambda} + \phi_i\right)\right\| \quad (5)$$

$$\delta h = \frac{\dot{h}\tan(e)}{\dot{e}} \quad (6)$$

where δh is the height rate correction, $\dot{e}$ denotes the rate of satellite elevation angle, $\hat{Y}_i$ are the detrended I/Q time series (linear trends removed), and a_i and ϕ_i are the amplitude and initial phase of the interferometric oscillation.

3.2 Least-squares harmonic estimation (LS-HE)

The LS-HE method is utilized in our study for retrieving sea-level variations from the GNSS-R I/Q interferometric observations and for the tidal harmonics analysis. The height retrieval uses multivariate LS-HE formulation while the tidal harmonics detection is based on univariate LS-HE. The multivariate LS-HE, as an extension of univariate harmonics estimation, can detect the common-mode signals in a set of multiple time series (Amiri-Simkooei et al. 2007). In the following, a brief introduction to this method is pro-

vided. Further details can be found in (Amiri-Simkooei 2013; Amiri-Simkooei et al. 2007; Rajabi et al. 2020a).

3.2.1 Univariate model

Observation equations can be modeled through the following linear model, which includes deterministic and stochastic parts of the time series (Amiri-Simkooei 2013):

$$E(y) = Ax, \ D(y) = Q_y, \quad (7)$$

with $E(\bullet)$ and $D(\bullet)$ indicating the expectation and dispersion operators. Deterministic behavior of the time series is captured by the first term $E(y) = Ax$ and the second term provides a stochastic model to describe the statistical characteristics of the observations. The vector of unknowns includes elements describing a low-order polynomial, e.g., two unknowns for a linear regression model.

Under null hypothesis, we assume that Eq. (7) can adequately model the time series. The model can be improved under the alternative hypothesis. For any periodic signal in the time series, the deterministic part of the model can be extended by a two-column design matrix A_k:

$$E(y) = Ax + A_k x_k, \quad D(y) = Q_y, \quad (8)$$

where the unknown vector x_k contains two elements to estimate the amplitudes of the signal $a_k \cos(\omega_k t) + b_k \sin(\omega_k t)$ at a frequency of ω_k. The unknown frequencies ω_k are detected through LS-HE, i.e., by maximizing the following functional:

$$\omega_k = arg \max_{\omega_j} P(\omega_j), \quad (9)$$

where

$$P(\omega_j) = \text{tr}(\hat{e}^T Q_y^{-1} A_j (A_j^T Q_y^{-1} P_A^\perp)^{-1} A_j^T Q_y^{-1} \hat{e}), \quad (10)$$

where tr is the trace operator and the least-squares residuals are $\hat{e} = P_A^\perp y$ with $P_A^\perp = I - A(A^T Q^{-1} A)^{-1} A^T Q^{-1}$ being an orthogonal projector. The values of $P(\omega_j)$ construct the power spectrum against a range of different frequencies. The frequency corresponding to the maximum value of the power spectrum indicates the frequency of interest, i.e., ω_K. The statistical significance of the detected frequency can be verified through a hypothesis testing procedure using the test statistic $T_k = P(\omega_j) = tr(\hat{e}^T Q_y^{-1} A_k (A_k^T Q_y^{-1} P_A^\perp)^{-1} A_k^T Q_y^{-1} \hat{e})$. Under the null hypothesis, if the covariance matrix Q_y is known and the distribution of the time series is normal, the test statistic has a central Chi-square distribution with 2 degrees of freedom. The detected frequency is statistically significant if the null hypothesis is rejected. The detection process can be repeated for other frequencies with the new design matrix $A = [A \ A_k]$.

3.2.2 Multivariate model

The LS-HE can be utilized for detecting common periodic signals in multiple time series through a multivariate power spectrum. Each time series can have a dedicated polynomial model with its corresponding unknown coefficients. In this case, if the design matrix A and covariance matrix Q_y are the same for all the time series, the deterministic model can be referred to as multivariate model represented by (Amiri-Simkooei 2013):

$$E(\text{vec}(Y)) = (I_r \otimes A)\,\text{vec}(X) + (I_r \otimes A_k)\text{vec}(X_k) \quad (11)$$

with the multivariate covariance matrix

$$D(\text{vec}(Y)) = \Sigma \otimes Q, \quad (12)$$

with r being the number of the time series, $\otimes$ the Kronecker product, I the identity matrix, and vec the vector operator. A and A_k are the design matrices.

The second term in Eq. (11) includes the element $(I_r \otimes A_k)$ which is meant to capture a common periodic pattern across all the time series. The common periodicity can have different phase and amplitude in different time series. The matrix Y is the observations matrix, which includes the time series as its columns. The matrices X and X_k are the unknowns. The frequency (ω_k) can be detected through the maximization of Eq. (9) with:

$$P(\omega_j) = \text{tr}(\hat{E}^T Q^{-1} A_j (A_j^T Q^{-1} P_A^{\perp})^{-1} A_j^T Q^{-1} \hat{E} \hat{\Sigma}^{-1}), \quad (13)$$

where $P(\omega_j)$ denotes the multivariate power spectrum, $\hat{E} = P_A^{\perp} Y$ is the least-squares residuals matrix and $P_A^{\perp} = I - A(A^T Q^{-1} A)^{-1} A^T Q^{-1}$ is the orthogonal projector and $\hat{\Sigma} = \hat{E}^T Q^{-1} \hat{E}/(m-n)$. The following test statistic can be used for testing the significance of the detected signal:

$$T = P(\omega_k) = \text{tr}(\hat{E}^T Q^{-1} A_k (A_k^T Q^{-1} P_A^{\perp})^{-1} A_k^T \quad (14)$$

If Σ and Q are known and the original observations follow a normal distribution, the test statistic T under the null hypothesis is considered to follow a central Chi-square distribution with $2r$ degrees of freedom, i.e., $T \sim \chi^2(2r, 0)$ with r being the number of the time series (Amiri-Simkooei 2013).

3.3 Applications of the LS-HE to height retrieval and tidal harmonics detection

We first apply multivariate LS-HE for SL calculation. The multivariate formulation provides a robust tool to find common-mode interferometric period in the I/Q time series

obtained from the GNSS-R receiver. The SL time series from GNSS-R and the nearby tide gauge are then analyzed by the univariate LS-HE to characterize the tidal harmonics.

The LS-HE method performs a numerical search to catch the dominant harmonic signals in the time series. The step size for finding the harmonic signals is determined with the following recursive formula:

$$T_i = T_{i-1}\left(1 + \alpha\,\frac{T_{i-1}}{T_{\max}}\right), \quad \alpha = 0.01, \quad i = 1, 2, \ldots, T_i \leq T_{\max}, \quad (15)$$

with T_i being the trial periods, T_0 and $T_{\max}$ the minimum and maximum periods in the time series based on Nyquist's theorem, respectively. The coefficient α controls the resolution or step of searching the periods. The recursive formula creates smaller step size for shorter periods and larger step size for longer periods. We assume the covariance matrix is the Identity matrix $Q_y = I$ for each time series. The observation matrices used in the SL retrieval and in the tidal harmonics analysis are as follows:

Observations matrix for finding interference pattern:

$$Y = [I, \; Q]$$

Observations matrix for tidal harmonic:

$$Y = [h_{\text{GNSS}}], \; Y = [h_{\text{TG}}] \quad (16)$$

It should be noted that univariate formulation of LS-HE with $Q_y = I$ will act similar to the ordinary least-squares method.

3.4 Phase and amplitude estimation

We use the U-tide MATLAB package (Codiga 2011), implemented according to the equilibrium tide theory (Foreman and Henry 1989) for deriving the amplitude and phase of a standard table of tidal constituents from the GNSS-R and tide gauge SL measurements. The following model is used for the estimation of the amplitude and phase of the tidal constituents [equation (6) in Foreman et al. (2009)]:

$$h(t_j) = Z_0 + a\,t_j + \sum_{k=1}^{n} f_k(t_j)[X_k\,\cos\,(V_k(t_j) + u_k(t_j))$$
$$+ Y_k\,\sin\,(V_k(t_j) + u_k(t_j))] + R(t_j) \quad (17)$$

where X_k and Y_k are:

$$X_k = A_k\,\cos\,g_k, \quad (18)$$
$$Y_k = A_k\,\sin\,g_k \quad (19)$$

with $h(t_j)$ being the SL measurement at the time t_j; Z_0 and a are the unknown linear terms, and for each constituent k

Fig. 4 Examples of observation time series of PRN 26 for one segment which are used to retrieve interferometric period (T_{int}) using multivariate LS-HE formulation. **a** The In-phase and Quadrature components for GPS L1 and L2 for the LHCP antenna. **b** The dominant interferometric period retrieved by applying LS-HE method to the combinations of the I/Q time series
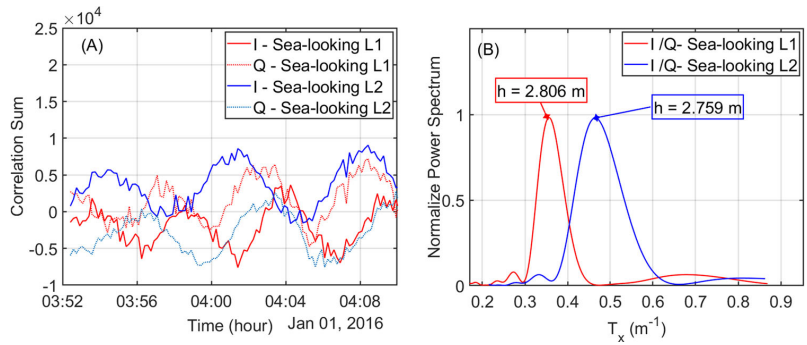

the unknown amplitude and phase are, respectively, denoted by A_k and g_k. In the process of tidal harmonic analysis, the unknown parameters are estimated by minimization of the residuals $R(t_j)$, while the nodal corrections (Godin 1972) to the amplitude ($f_k(t_j)$) and phase ($u_k(t_j)$), and the astronomical argument $V_k(t_j)$ (Godin 1972) can be calculated for each constituent k at the time of sea-level measurement t_j (Foreman et al. 2009).

4 Results and discussion

The performance of SL retrieval from the I/Q interference patterns at different antenna settings and sea states has been already discussed in (Rajabi et al. 2021a, b, 2022). According to these investigations, the sea-looking LHCP antenna performs better compared to both up- and sea-looking RHCP antennas. The improvement is significant and can reach 48% and 50% for L1 and L2 frequencies, respectively. Moreover, combining the SL measurements from L1 and L2 improves the accuracy of final sea surface heights by up to 25% and 40%. Therefore, we use the SL measurements from the combined L1 and L2 I/Q observations of the sea-looking LHCP antenna. The measurements have a temporal resolution of 5 min. This setting is chosen to provide an adequate dataset for retrieving tidal harmonics.

In the first step, we down-sampled I/Q correlation sums to a 10-second (0.1 Hz) integration due to the outputs of the GORS receiver being based on 5-millisecond coherent integration time (200 Hz sampling rate). Afterward, we prepared the 15 min time series of I/Q with the time step of 1 min for extracting interferometric pattern periods using multivariate LS-HE to calculate L12 SL with an averaging window of 15 min and 5-minute time step. The multivariate analysis improves the detection by utilizing common-mode signals from the different GNSS-R time series by amplifying the power of the retrieved signals. Figure 4 visualized an example estimation of the LS-HE on the time series which is generated from a 15 min segment for satellite PRN 26 in L1 and
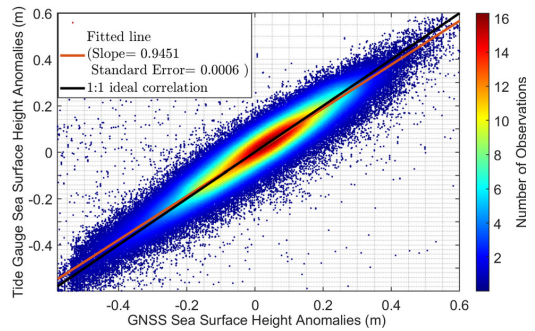
Fig. 5 Scatter plot of the GNSS-R and tide gauge height anomalies with the time step and averaging window of 5 and 15 min, respectively. The fitted line and 1:1 ideal correlation are shown by the solid red line and black line, respectively

L2 signals. Figure 4a shows the I and Q components from the LHCP antenna in different frequencies, and Fig. 4b depicts the harmonic analysis results for L1 and L2, including estimated heights.

Figure 5 compares the sea surface height variations from GNSS-R and tide gauge measurements. The SL variations from the two datasets show a high level of agreement. The red is the fitted line to the corresponding measurements from the datasets, and the black line illustrates the ideal 1:1 line. The RMSE between GNSS-R L12 sea surface heights with collocated tide gauge observations is 5.8 cm with a correlation of 0.948.

We utilize the univariate LS-HE method for detecting the tidal harmonics in the GNSS-R L12 and tide gauge sea-level time series. Figure 6a illustrates the tidal periods retrieved from both GNSS-R estimated and tide gauge heights. These plots show the detected periodic harmonics until the annual and semiannual tidal harmonics S_a and S_{sa}. S_a and S_{sa} are smaller than other tidal constituents and insignificant for most applications, but their estimated values are much larger than would be reasonable from astronomical forcing due to

Fig. 6 The least-squares power spectrum of the tidal harmonics detected in the GNSS-R and tide gauge (TG) sea-level measurements. The measurements cover a period of 6 years with a temporal resolution of 5 min. **a** The overall Periodogram produced by applying the univariate LS-HE to the GNSS-R and tide gauge data. **b** The power ratio between the two periodograms. **c, d** Provide zoomed views of the detected tidal harmonics with periods between 3 to 30 and 0.5 to 3 h, respectively
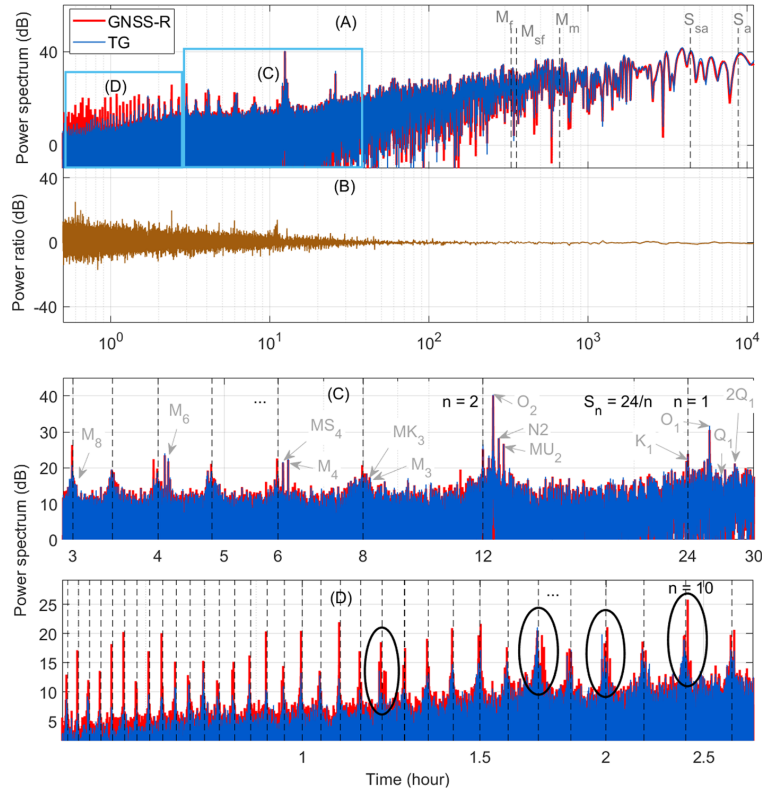
the seasonal changes in wind, temperature, and atmospheric pressure. Overall, the detected harmonics from the GNSS-R and tide gauge time series coincide very well. For instance, both sensors could successfully capture the periodicity of the lunar monthly constituent (M_m), lunar synodic fortnightly constituent (M_{sf}), and lunar fortnightly constituent (M_f). Figure 6b depicts the ratio of the GNSS-R and tide gauge power spectra. The variation of the power ratio is mostly distributed equally around zero.

Two parts of the spectra shown in Fig. 6a are magnified and presented in Fig. 6c, d. Figure 6c depicts the detected harmonics with periods between ≈ 3 and 30 h and Fig. 6d covers the periods ranging from 30 min to just below 3 h. The periodograms in Fig. 6c, d show the main tidal harmonic constituents segment the period spectrum with the central harmonics of $S_n = 24/n, n = 1, 2, \ldots$. Several harmonics are detected around the S_n harmonics. The results which the tidal harmonics are around S_n in the spectral analysis agree with the tidal analysis presented by Amiri-Simkooei et al. (2014). For better visualization, some of the harmonics by Darwin's symbols are marked in Fig. 6a, c. Both of the datasets can similarly capture the main tidal frequencies, e.g.,

the tidal periods longer than one day (bi-monthly, monthly, semiannual), the solar diurnal signal, and its higher harmonics (S_n), lunar diurnal and higher harmonics (O_1, K_1, ρ_1, M_2, N_2, M_3, M_4 and M_6), lunisolar diurnal (K_1) and variational (MU_2) and shallow waters (i.e., MK_3).

Figure 6d shows the detected tidal harmonics with periods below 3 h. The periodograms shown in Fig. 6 confirm the overall excellent performance of the GNSS-R measurements. However, we have detected some harmonics in GNSS-R time series (marked by a green ellipsoid in Fig. 6d) that are not well-accompanied by TG counterparts. In this area, some GNSS-R retrieved picks are stronger than TG and are closer to the standard tidal periods. For example, standard tenth-diurnal tidal constituents (according to the standard tidal constituents list of the tide, water level and current working group of international hydrographic organization (https://iho.int/en/twcwg) start from 2.431 to 2.511 h, and the estimated period by GNSS data is around 2.428 compared to 2.390 from TG. For the case of fourteenth-diurnal with the period of 1.766 to 1.770 h in the standard tide table, GNSS-R detects sharp peaks from 1.728 to 1.741 in contrast to a less prominent TG peak at 1.724 h. Therefore, GNSS-R

Table 1 The amplitudes and initial phases of the standard tidal constituents up to the annual period which were detected by the univariate least-squares harmonic estimation of 6-year time series for both tide gauge (TG) and GNSS-R

Darwin's symbol	Period (h)	Amp_T (cm)	Amp_G (cm)	Δ_{Amp}	ϕ_T°	ϕ_G°	abs(Δ_{phi}°)
Long periods							
S_a	8766.2315	4.57	4.40	0.18	290.9	287.5	3.4
S_{sa}	4382.9063	5.46	5.17	0.29	256.4	254.7	1.7
M_m	661.3092	2.27	2.13	0.14	170.2	172.2	2.0
M_{sf}	354.3671	0.87	0.83	0.05	145.6	142.4	3.2
M_f	327.8590	1.11	0.94	0.17	208.7	211.3	2.6
Diurnals							
$2Q_1$	28.0062	0.34	0.33	0.02	260.4	263.1	2.7
Q_1	26.8684	0.43	0.38	0.05	257.9	266.5	8.6
ρ_1	26.7231	0.27	0.25	0.02	277.6	289.1	11.6
O_1	25.8193	2.25	2.04	0.21	299.0	301.9	3.0
M_1	24.8332	0.33	0.34	0.00	335.3	326.4	8.9
P_1	24.0659	0.29	0.30	0.00	278.0	305.4	27.5
S_1	24.0000	0.94	1.03	− 0.09	27.6	40.0	12.4
K_1	23.9345	0.47	0.09	0.37	308.8	52.8	104.0
J_1	23.0985	0.12	0.11	0.00	156.2	170.8	14.6
OO_1	22.3061	0.10	0.13	− 0.03	288.6	238.3	50.2
Semi-Diurnals							
$2''N_2$	12.9054	0.15	0.12	0.03	38.3	59.4	21.1
MU_2	12.8718	1.08	1.13	− 0.06	316.2	319.1	2.9
N_2	12.6583	1.30	1.31	− 0.01	108.7	112.5	3.9
V_2	12.6260	0.47	0.50	− 0.02	135.7	131.5	4.2
M_2	12.4206	5.32	5.28	0.04	151.4	153.4	2.0
λ_2	12.2218	0.35	0.32	0.04	260.0	265.4	5.4
L_2	12.1916	0.60	0.63	− 0.04	277.3	282.1	4.8
T_2	12.0164	0.17	0.09	0.07	122.4	85.4	37.0
S_2	12.0000	1.13	1.00	0.13	106.1	101.2	4.9
R_2	11.9836	0.13	0.19	− 0.06	315.6	308.2	7.5
K_2	11.9672	0.21	0.20	0.01	70.2	338.8	91.4
Higher harmonics							
$2''MK_3$	8.3863	0.22	0.22	0.00	8.1	352.1	16.0
M_3	8.2804	0.15	0.14	0.01	26.0	18.6	7.4
MK_3	8.1771	0.16	0.16	0.00	254.3	348.9	94.6
MN_4	6.2692	0.21	0.19	0.02	296.5	304.7	8.2
M_4	6.2103	0.73	0.70	0.03	302.9	309.1	6.2
MS_4	6.1033	0.49	0.50	− 0.01	31.7	39.3	7.6
S_4	6.0000	0.14	0.13	0.01	27.8	4.5	23.3
M_6	4.1402	0.72	0.63	0.09	65.4	69.7	4.3
M_8	3.1052	0.05	0.04	0.01	337.7	355.0	17.2

Amp_T (cm) and Amp_G (cm) denote the amplitudes related to TG and GNSS-R, respectively. ϕ_T° and ϕ_G° are the initial phases of the TG and GNSS-R, respectively. $\Delta_{Amp} = Amp_G - Amp_T$ is the differences between the GNSS-R and TG amplitudes

Fig. 7 The estimated amplitudes of standard tidal constituents retrieved from GNSS-R and Tide Gauge observations. The blue bars are related to the GNSS-R, and the red bars show the tide gauge estimates. The circles above the bars visualize the relative error between GNSS-R and tide gauge amplitudes by their sizes and colors. Horizontal axes are labeled by the Darwin Symbol clarified in Table 1
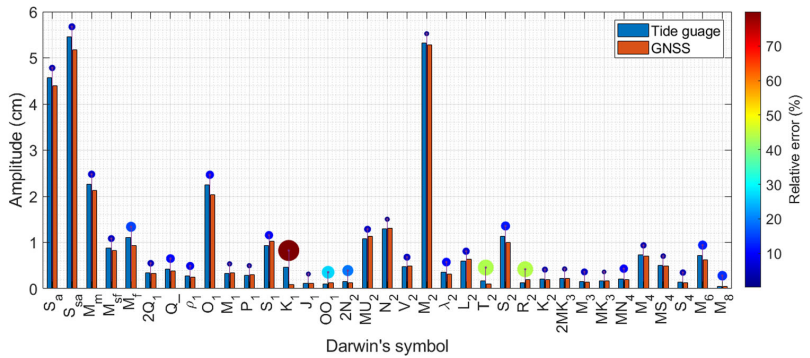
Fig. 8 Comparison of amplitudes and phases of the most important tidal harmonics at Onsala stations based on polar representation. The amplitudes are shown in centimeter and the phases are in degrees
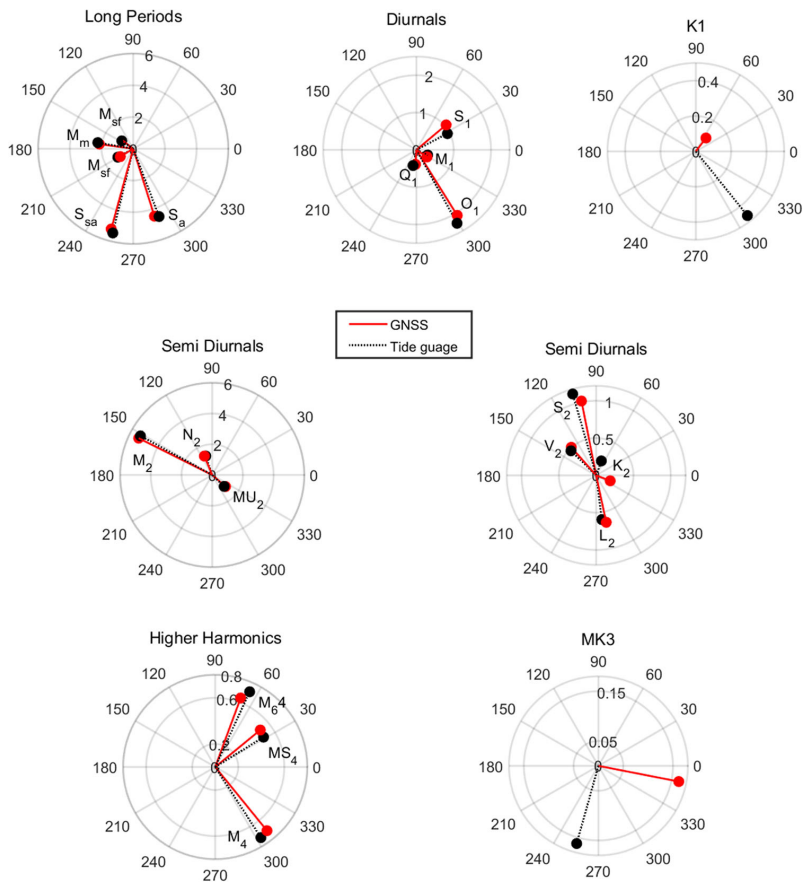
shows a better performance in detecting higher harmonics. Geremia-Nievinski et al. (2020) investigated the capability of GNSS-R using the least-square method in Onsala to capture tidal harmonics between 3 and 30 h. Their results confirm that GNSS-R is successful in capturing the dominant tidal constituents. However, long periods of tidal harmonics are less discussed in the GNSS-R studies due to the limited time span of the datasets. The same issue applies to the period shorter than 3 h because of the temporal resolution of the retrieved sea levels. For example, Semmling et al. (2012) could detect the diurnal ($K1$) and semi-diurnal harmonics ($M2$, $S2$) in Godhavn. Löfgren et al. (2014) report their tidal analysis and the captured periods (semi-diurnal up to semiannual) in five different stations, one of which is located in Onsala. This study investigates tidal harmonics with a wide range of periods from 30 min to 1 year using a relatively long dataset. It should be noted that the GNSS-R station used in the two studies mentioned above in Onsala are different from our experiment and are based on SNR observations from geodetic receivers.

Table 1 lists the amplitudes larger than the 1-sigma confidence interval and the initial phases of the standard tidal constituents estimated from the tide gauge and GNSS-R. The table highlights an overall good agreement between the tide gauge and GNSS-R results, suggesting that the GNSS-R sea-level products can effectively be used for the tidal analysis purposes. As can be seen from Table 1, the most significant difference of 3.7 mm between the amplitudes belongs to K_1 constituent as depicted in Fig. 7. The figure visualizes Table 1 regarding amplitude and relative errors between two datasets. The blue and red bars show the amplitudes of the tidal harmonics retrieved from GNSS-R and TG observations, respectively. The size and color of the circles above the bars illustrate the relative error between the estimated amplitudes in percentage. The relative errors are calculated as the difference of the two amplitudes divided by the tide gauge amplitude. Figure 8 highlights the agreements and discrepancies between the estimated phase values of GNSS-R and tide gauge using the polar coordinate system. The estimated phase values from GNSS-R measurements for harmonics K_1, OO_1, K_2, and MK_3 show large deviations from the tide gauge estimates, although they have relatively small amplitudes at the site. The GPS orbital period can be one the main contributors to the observed differences as reported by previous studies (e.g., Tabibi et al. (2020), Larson et al. (2017), Löfgren et al. (2014)). This effect is more noticeable in phase of the tidal harmonics.

Our estimated amplitudes for daily and sub-daily harmonics agree with a similar study at Onsala by Löfgren et al. (2014). However, for the monthly and semiannual harmonics the differences are significant. These differences can stem from the fact that the results presented here are based on measurements at higher temporal resolution from I/Q obser-

vations over much longer time span (6 years compared to six months).

5 Conclusion

This study investigated the potential of ground-based GNSS-R technique for detecting and analyzing tidal constituents. The analysis is conducted using a relatively long dataset of 6 years obtained from a coastal GNSS-R experiment installed at Onsala Space Observatory. A highlight of this study was to utilize dual-frequency I/Q interferometric observations to retrieve sea level and tidal harmonics. We applied uni- and multivariate least-squares harmonic estimation (LS-HE) method for sea-level calculation and estimating tidal constituents. The U-tide software is used to retrieve the amplitude and phase of a list of standard tidal harmonics. The RMSE value between GNSS-R sea surface heights for LHCP sea-looking antenna and collocated tide gauge measurements was 5.8 cm, with a correlation of 0.948. Our tidal harmonics analysis, owing to the long dataset and a high temporal resolution measurements of 5 min, could capture a broad range of periods, i.e., from 30 min to annual. Both the GNSS-R and tide gauge sea-level measurements showed similar performance in capturing tidal constitutes. However, the GNSS-R shows supremacy in detecting harmonics with the periods shorter than 3 h. Comparison of the estimated amplitude and phase of the standard tidal periods indicates a high level of agreement between the GNSS-R and tide gauge observations. However, a significant difference is observed for the amplitude and phase of the k_1 constituent. Moreover, the phase values of OO_1, K_2, and MK_3 constituents derived from GNSS-R are notably different compared to the tide gauge. As already reported in the literature, the orbital period of GPS is considered as one of the main affecting factors for the observed differences. It should be noted that these four constituents have very small amplitudes of less than 5 mm at Onsala. The study suggests that a dedicated GNSS-R setup based on the dual-frequency I/Q observations from sea-looking antenna, provides accurate tidal products.

References

Adebisi N, Balogun AL, Min TH, Tella A (2021) Advances in estimating sea level rise: a review of tide gauge, satellite altimetry and spatial data science approaches. Ocean Coast Manag 208(105):632

Amiri-Simkooei AR, Tiberius CC, Teunissen PJ (2007) Assessment of noise in GPS coordinate time series: methodology and results. J Geophys Res Solid Earth 112(B7)

Amiri-Simkooei A (2013) On the nature of GPS draconitic year periodic pattern in multivariate position time series. J Geophys Res Solid Earth 118(5):2500–2511

Amiri-Simkooei A, Zaminpardaz S, Sharifi M (2014) Extracting tidal frequencies using multivariate harmonic analysis of sea level height time series. J Geod 88(10):975–988

Anderson KD (2000) Determination of water level and tides using interferometric observations of GPS signals. J Atmos Ocean Technol 17(8):1118–1127

Asgarimehr M, Hoseini M, Semmling M, Ramatschi M, Camps A, Nahavandchi H, Haas R, Wickert J (2021) Remote sensing of precipitation using reflected GNSS signals: response analysis of polarimetric observations. IEEE Trans Geosci Remote Sens. https://doi.org/10.1109/TGRS.2021.3062492

Church JA, White NJ (2011) Sea-level rise from the late 19th to the early 21st century. Surv Geophys 32(4):585–602

Cipollini P, Calafat FM, Jevrejeva S, Melet A, Prandi P (2017) Monitoring sea level in the coastal zone with satellite altimetry and tide gauges. In: Integrative study of the mean sea level and its components, pp 35–59

Codiga DL (2011) Unified tidal analysis and prediction using the UTide Matlab functions. Technical report 2011-01. Graduate School of Oceanography, University of Rhode Island, Narragansett

Devlin AT (2016) On the variability of pacific ocean tides at seasonal to decadal time scales: observed vs modelled. Ph.D. thesis, Portland State University

Doodson A (1954) Appendix to circular-letter 4-h. The harmonic development of the tide-generating potential. Int Hydrogr Rev 31:37–61

Foreman MGG, Henry RF (1989) The harmonic analysis of tidal model time series. Adv Water Resour 12(3):109–120

Foreman MG, Cherniawsky JY, Ballantyne V (2009) Versatile harmonic tidal analysis: improvements and applications. J Atmos Ocean Technol 26(4):806–817

Foti G, Gommenginger C, Srokosz M (2017) First spaceborne GNSS-reflectometry observations of hurricanes from the UK TechDemoSat-1 mission. Geophys Res Lett 44(24):12–358

Geremia-Nievinski F, Hobiger T, Haas R, Liu W, Strandberg J, Tabibi S, Vey S, Wickert J, Williams S (2020) SNR-based GNSS reflectometry for coastal sea-level altimetry: results from the first IAG inter-comparison campaign. J Geodesy 94(8):1–15

Godin G (1972) University of Toronto Press

Gravalon T, Seoane L, Ramillien G, Darrozes J, Roblou L (2022) Determination of weather-induced short-term sea level variations by GNSS reflectometry. Remote Sens Environ 279(113):090

Helm A, Montenbruck O, Ashjaee J, Yudanov S, Beyerle G, Stosius R, Rothacher M (2007) GORS-A GNSS occultation, reflectometry and scatterometry space receiver. In: Proceedings of the 20th international technical meeting of the Satellite Division of The Institute of Navigation (ION GNSS 2007), pp 2011–2021

Hoseini M, Asgarimehr M, Zavorotny V, Nahavandchi H, Ruf C, Wickert J (2020) First evidence of mesoscale ocean eddies signature in GNSS reflectometry measurements. Remote Sens 12(3):542

Hoseini M, Semmling M, Nahavandchi H, Rennspiess E, Ramatschi M, Haas R, Strandberg J, Wickert J (2020b) On the response of polarimetric GNSS-reflectometry to sea surface roughness. IEEE Trans Geosci Remote Sens

Larson KM, Ray RD, Williams SD (2017) A 10-year comparison of water levels measured with a geodetic GPS receiver versus a conventional tide gauge. J Atmos Ocean Technol 34(2):295–307

Löfgren JS, Haas R, Scherneck HG (2014) Sea level time series and ocean tide analysis from multipath signals at five GPS sites in different parts of the world. J Geodyn 80:66–80

Marti F, Cazenave A, Birol F, Passaro M, Léger F, Niño F, Almar R, Benveniste J, Legeais JF (2019) Altimetry-based sea level trends along the coasts of Western Africa. Adv Space Res

Martin-Neira (1993) A passive reflectometry and interferometry system (PARIS): application to ocean altimetry. ESA J 17(4):331–355

Rajabi M, Amiri-Simkooei A, Asgari J, Nafisi V, Kiaei S (2015) Analysis of TEC time series obtained from global ionospheric maps. J Geomat Sci Technol 4(3):213–224

Rajabi M, Amiri-Simkooei A, Nahavandchi H, Nafisi V (2020) Modeling and prediction of regular ionospheric variations and deterministic anomalies. Remote Sens 12(6):936

Rajabi M, Nahavandchi H, Hoseini M (2020) Evaluation of CYGNSS observations for flood detection and mapping during Sistan and Baluchestan Torrential Rain in 2020. Water 12(7):2047

Rajabi M, Hoseini M, Nahavandchi H, Semmling M, Ramatschi M, Goli M, Haas R, Wickert J (2022) Polarimetric GNSS-R sea level monitoring using I/Q interference patterns at different antenna configurations and carrier frequencies. IEEE Trans Geosci Remote Sens 60:1–13. https://doi.org/10.1109/TGRS.2021.3123146

Rajabi M, Hoseini M, Nahavandchi H, Semmling M, Ramatschi M, Goli M, Haas R, Wickert J (2021a) Performance assessment of GNSS-R polarimetric observations for sea level monitoring. In: EGU general assembly conference abstracts, pp EGU21–12709

Rajabi M, Hoseini M, Nahavandchi H, Semmling M, Ramatschi M, Goli M, Haas R, Wickert J (2021b) A performance assessment of polarimetric GNSS-R sea level monitoring in the presence of sea surface roughness. In: 2021 IEEE international geoscience and remote sensing symposium IGARSS, IEEE, pp 8328–8331

Rourke FO, Boyle F, Reynolds A (2010) Tidal energy update 2009. Appl Energy 87(2):398–409

Semmling A, Schmidt T, Wickert J, Schön S, Fabra F, Cardellach E, Rius A (2012) On the retrieval of the specular reflection in GNSS carrier observations for ocean altimetry. Radio Sci 47(06):1–13

Semmling AM, Leister V, Saynisch J, Zus F, Heise S, Wickert J (2016) A phase-altimetric simulator: Studying the sensitivity of Earth-reflected GNSS signals to ocean topography. IEEE Trans Geosci Remote Sens 54(11):6791–6802

Semmling AM, Rösel A, Divine DV, Gerland S, Stienne G, Reboul S, Ludwig M, Wickert J, Schuh H (2019) Sea-ice concentration derived from GNSS reflection measurements in Fram Strait. IEEE Trans Geosci Remote Sens 57(12):10,350-10,361

Shum C, Yu N, Morris CS (2001) Recent advances in ocean tidal science. J Geod Soc 47(1):528–537

Tabibi S (2016) Snow depth and soil moisture retrieval using SNR-based GPS and GLONASS multipath reflectometry. Ph.D. thesis, University of Luxembourg, Luxembourg

Tabibi S, Geremia-Nievinski F, Francis O, van Dam T (2020) Tidal analysis of GNSS reflectometry applied for coastal sea level sensing in Antarctica and Greenland. Remote Sens Environ 248(111):959. https://doi.org/10.1016/j.rse.2020.111959

Vu PL, Ha MC, Frappart F, Darrozes J, Ramillien G, Dufrechou G, Gegout P, Morichon D, Bonneton P (2019) Identifying 2010 Xynthia storm signature in GNSS-R-based tide records. Remote Sens 11(7):10. https://doi.org/10.3390/rs11070782

Williams S, Nievinski F (2017) Tropospheric delays in ground-based GNSS multipath reflectometry—experimental evidence from coastal sites. J Geophys Res Solid Earth 122(3):2310–2327

Zavorotny VU, Gleason S, Cardellach E, Camps A (2014) Tutorial on remote sensing using GNSS bistatic radar of opportunity. IEEE Geosci Remote Sens Mag 2(4):8–45. https://doi.org/10.1109/MGRS.2014.2374220

Zeiger P, Frappart F, Darrozes J, Roussel N, Bonneton P, Bonneton N, Detandt G (2021) SNR-based water height retrieval in rivers: application to high amplitude asymmetric tides in the Garonne River. Remote Sens 13(9):25. https://doi.org/10.3390/rs13091856

NTNU
Norwegian University of
Science and Technology